

Molecular Self-Assembly of Reactive Organic and Metal-
Organic Solids

Joseph M. Marrett

A Thesis submitted to McGill University in partial fulfillment of
the requirements of the degree of

Master of Science

Department of Chemistry

McGill University

Montreal, Quebec, Canada

July 2021

©Joseph Marrett, 2021. All rights reserved.

Abstract

Developing strategies to induce and control reactivity in solid materials is a pursuit with far-reaching relevance from pharmaceutical formulation to organic synthesis. The design of crystalline materials whose solid-state structures determine the reactivity of their molecular building blocks has been the central focus of crystal engineering since Schmidt related the crystal structures of organic crystals to their solid-state reactivity in the 1960s. This thesis will present two self-assembled crystalline materials with designed reactivity: an organic salt which is able to crystallize with a set of reactive partner molecules, and a metal-organic framework with reactivity appropriate for solid rocket fuel applications. In the first example, we present an organic salt which reliably crystallizes with small polar molecules to form hexameric supramolecular halogen bonded cages with the polar molecules as guests. The organic salt, (dibromomethyl)triphenylphosphonium bromide, is a precursor to a reactive phosphorous ylide capable of acting on carbonyl-containing substrates as part of a Wittig olefination reaction. We show that a set of aldehydes and a ketone can be encapsulated as guests within the cavities of the Wittig-salt capsule, and that this compound material can afford gem-dibromoolefin Wittig products by simple mechanochemical milling with solid base. This supramolecular assembly is also capable of acting as an equivalent to the product olefin in the context of a palladium-catalyzed Sonogashira cross-coupling reaction, where the nascent vinylbromides couple to terminal alkynes.

The second example is of a set of novel copper imidazolate metal-organic frameworks (MOFs) whose imidazolate organic linkers are decorated with methyl, vinyl, and acetylene moieties to provide predictable chemical reactivity to the solid material. In particular, the vinyl and acetylene functionalities confer hypergolicity, the reactive property of ignition on contact with an oxidizer, to these otherwise non-hypergolic framework materials. Crucially, these copper-based materials show higher energy densities than the previously reported hypergolic MOF materials, on account of their densely packed non-porous crystalline structures, advancing the effort to find alternative and environmentally amenable hypergolic materials for use in aerospace rocket propulsion systems. Additionally, the acetylene-decorated material shows impact-induced polymorphism with retention of hypergolicity, presenting an opportunity to study hypergolicity as a function of crystal structure.

The two examples detailed herein represent our efforts to design molecular and framework solids with predictable and useful chemical reactivity and solid-state properties, and highlight the relationships between chemical identity, crystal structure, and solid-state reactivity.

Abrégé

Le développement de stratégies visant à induire et à contrôler la réactivité de matériaux solides représente une recherche d'une grande importance, de la formulation pharmaceutique à la synthèse organique. La conception de matériaux cristallins dont les structures à l'état solide déterminent la réactivité de leurs éléments moléculaires est au cœur de l'ingénierie des cristaux depuis que Schmidt a relié les structures cristallines des cristaux organiques à leur réactivité à l'état solide dans les années 1960. Cette thèse présente deux matériaux cristallins auto-assemblés avec une réactivité déterminée : un sel organique capable de cristalliser avec un ensemble de molécules partenaires réactives et un cadre métallo-organique (metal-organic framework, MOFs) dont la réactivité est adaptée aux applications de combustible solide pour fusée. Dans le premier exemple, nous présentons un sel organique qui cristallise de manière fiable avec de petites molécules polaires pour former des cages supramoléculaires hexamériques à liaison halogène avec les molécules polaires comme hôtes. Le sel organique, le bromure de (dibromométhyl)triphénylphosphonium, est un précurseur d'un ylides phosphoreux réactif capable d'agir sur des substrats contenant du carbonyle dans le cadre d'une réaction d'oléfination de Wittig. Nous montrons qu'un ensemble d'aldéhydes et une cétone peuvent être encapsulés en tant qu'invités dans les cavités de la capsule de sel de Wittig, et que ce matériau composé peut donner des produits de Wittig de type gem-dibromo-oléfine par simple broyage mécano-chimique avec une base solide. Cet assemblage supramoléculaire est également capable d'agir comme un équivalent d'oléfine produite dans le contexte d'une réaction de couplage croisé de Sonogashira catalysée par le palladium, où les bromures de vinyle naissants se couplent à des alcynes terminaux.

Le deuxième exemple concerne un ensemble de nouveaux cadres métallo-organiques (metal-organic frameworks, MOF) à base d'imidazolate de cuivre dont les liens organiques imidazolate possèdent des fragments méthyle, vinyle et acétylène pour produire une réactivité chimique prévisible du matériau solide. En particulier, les fonctionnalités vinyle et acétylène confèrent l'hypergolicité, la propriété réactive d'inflammation au contact d'un oxydant, à ces matériaux de structure autrement non hypergoliques. Il est important de noter que ces matériaux à base de cuivre présentent des densités énergétiques plus élevées que les matériaux MOF hypergoliques précédemment rapportés, en raison de leurs structures cristallines denses et non poreuses, ce qui

fait progresser les efforts visant à trouver des matériaux hypergoliques alternatifs et respectueux de l'environnement pour une utilisation dans des systèmes de propulsion de fusées aérospatiales. En outre, le matériau à base d'acétylène présente un polymorphisme induit par impact avec conservation de l'hypergolicité, ce qui permet d'étudier l'hypergolicité en fonction de la structure cristalline.

Les deux exemples détaillés ici représentent nos efforts pour concevoir des solides moléculaires et structuraux présentant une réactivité chimique et des propriétés à l'état solide prévisibles et utiles, et mettent en évidence les relations entre l'identité chimique, la structure cristalline et la réactivité à l'état solide.

Acknowledgements

My greatest thanks go to my supervisor and mentor, Prof. Tomislav Friščić, whose passion and excitement are contagious. It is never hard to find motivation or inspiration to get into the lab and have fun when working for him.

The students and postdocs who made great efforts to teach me how to do research also deserve many thanks. They include Dr. Cristina Mottillo, Dr. Dayaker Gandrath, Dr. Ghada Ayoub, Prof. Mihails Arhangelskis, Dr. Igor Huskić, Dr. Filip Topić, Dr. Patrick Julien, Dr. Thanassis Katsenis, Mr. Jean-Louis Do, and more. Dr. Hatem Titi has been of special significance to me as a teacher, research-mate and friend. I thank all the current group members, who are tremendously fun, smart, and dynamic, for their support and friendship. The lab is as fun now as it has ever been.

Finally, I thank my parents and grandparents for being supportive, interested, and invested.

Contributions of Authors

Abstract:

The abstract was written by Joseph M. Marrett and translated to French by Dr. Lori Gonnet.

Chapter 1: Introduction

The introduction was written by Joseph M. Marrett with guidance from Prof. Tomislav Friščić.

Chapter 2: A hexameric halogen-bonded phosphonium salt cage for encapsulation and solid-state transformation of small-molecule carbonyl compounds

Joseph M. Marrett, Dr. Hatem M. Titi, and Prof. Tomislav Friščić

Chapter 2 is based on a manuscript being prepared for submission to an academic journal, written primarily by Joseph M. Marrett and edited by the coauthors. It is coauthored by Dr. Hatem M. Titi, who assisted with single crystal X-ray diffraction measurements and the subsequent structural solution and refinement, and Prof. Tomislav Friščić who provided supervision and guidance.

Chapter 3: Ab Initio metal-organic framework crystal structure prediction reveals elusive and functional copper imidazolate frameworks

Joseph M. Marrett, Yizhi Xu, Dr. Hatem M. Titi, Dr. James P. Darby, Prof. Robin D. Rogers, Prof. Andrew J. Morris, Prof. Mihails Arhangelskis, and Prof. Tomislav Friščić.

Chapter 3 is the result of a collaboration between the groups of Prof. Tomislav Friščić (McGill University), Prof. Mihails Arhangelskis (University of Warsaw), and Prof. Andrew J. Morris (University of Birmingham). The chapter is based on a manuscript being prepared for submission to an academic journal and was written primarily by Joseph M. Marrett with input and editing from the coauthors. Ms. Yizhi Xu and Prof. Mihails Arhangelskis are responsible for all computational analyses in Chapter 3 and were provided guidance for this by Dr. James P. Darby and Prof. Andrew J. Morris. Dr. Hatem M. Titi assisted with hypergolic testing and the structural solution and

refinement of single crystal X-ray structures. Prof. Robin D. Rogers, Prof. Andrew J. Morris, Prof. Mihails Arhangeliskis provided guidance and Prof. Tomislav Friščić provided guidance and supervision.

Chapter 4: Conclusion

The conclusion was written by Joseph M. Marrett with guidance from Prof. Tomislav Friščić.

Table of Contents

Abstract	2
Acknowledgements	6
Author Contributions	7
List of Abbreviations	10
List of Figures	11
List of Tables	14
Chapter 1: Introduction	
1.1 General introduction	15
1.2 Reactions of crystalline organic solids.....	15
1.3 Supramolecular encapsulation	21
1.4 Metal-organic materials	22
1.5 Applications of MOFs.....	28
1.6 Energy and stability of MOFs.....	32
1.7 Mechanochemistry	34
Connecting text for Chapter 2	42
Chapter 2: A hexameric halogen-bonded phosphonium salt cage for encapsulation and solid-state transformation of small-molecule carbonyl compounds	
2.1 Abstract	43
2.2 Introduction.....	43
1.3 Results and discussion	44
1.4 Conclusion	55
Connecting text for Chapter 3	57
Chapter 3: <i>Ab initio</i> metal-organic framework crystal structure prediction reveals elusive copper(II) imidazolate frameworks	
3.1 Abstract	58
3.2 Introduction.....	58
1.3 Results and discussion	59
1.4 Conclusion	65
Appendix A	70
Appendix B	107

List of Abbreviations

- ¹³C and ¹H NMR:** Carbon and proton nuclear magnetic resonance
- AIm :** 2-ethynylimidazolate
- AIRSS:** *Ab initio* random structure searching algorithm
- COF:** Covalent-organic framework
- CP/MAS SSNMR:** Cross polarization/magic angle spinning solid-state nuclear magnetic resonance
- CSP:** Crystal structure prediction
- DFT:** Density functional theory
- DMF:** N,N-dimethylformamide
- DMSO:** Dimethyl sulfoxide
- ESP:** Electrostatic surface potential
- FTIR:** Fourier-transform infrared spectroscopy
- HSAB:** Hard-soft acid-base theory
- ID:** Ignition delay
- IRMOF:** Isoreticular metal-organic framework
- LAG:** Liquid-assisted grinding
- MBD*:** Many-body dispersion correction
- MeIm:** 2-methylimidazolate
- MOF:** Metal-organic framework
- NMP:** N-methyl-2-pyrrolidone
- PXRD:** Powder X-ray diffraction
- RAM:** Resonant acoustic mixing
- SCSC:** Single-crystal-to-single-crystal
- scXRD:** Single-crystal X-ray diffraction
- TGA:** Thermogravimetric analysis
- VIm:** 2-vinylimidazolate
- WAM:** Wyckoff alignment of molecules
- WFNA:** White fuming nitric acid
- XB:** Halogen bond
- ZIF:** Zeolitic imidazolate framework

List of Figures

Chapter 1: Introduction

Figure 1.1: Polymorphs of *trans*-cinnamic acid undergo [2+2] photodimerization according to their crystal packing, as articulated by de Jong,⁷ and Schmidt's topochemical postulates.⁸

Figure 1.2: The host (R,R)-(-)-*trans*-2,2,-dimethyl-1,3-dioxacyclopentane forms an inclusion complex with coumarin, arranging the two coumarin molecules such that an enantioselective [2+2] photodimerization is possible in the solid-state. Republished with permission of John Wiley & Sons, from K. Tanaka, F. Toda, E. Mochizuki, N. Yasui, Y. Kai, I. Miyahara, K. Hirotsu, *Angew. Chem. Int. Ed.* **1999**, 38, 3523-3525.; permission conveyed through Copyright Clearance Center, Inc.

Figure 1.3: Possible orientations of coumarin as cocrystallized with cyclodextrins, as imagined by Weiss. Figure reproduced from reference X. Reprinted (adapted) with permission from J. N. Moorthy, K. Venkatesan, R. G. Weiss, *J. Org. Chem.* **1993**, 57, 3292-3297. Copyright 1993, American Chemical Society.

Figure 1.4: Overview of [2+2] photodimerization and its use to form a diffraction grating. a) A styrylpyrylium salt undergoes thermally reversible photodimerization; single crystals of the monomer and dimer will interconvert while preserving monocrystallinity. Reprinted (adapted) with permission from W. Köhler, K. Novak, V. Enkelmann, *J. Chem. Phys.* **1994**, 101, 10474-10480. Copyright 1994, AIP publishing. b) Single crystals can be converted to diffraction gratings by careful irradiation to create spatially resolved solid solutions of monomer and dimer in a "layer" format.

Figure 1.5: Cram's capsule and the reactions performed within. a) Cram's hemicarceplex encapsulating guest **G**, decorated with CH₂CH₂Ph groups to improve solubility. b) All reactions shown were performed inside the inner cavity of the molecular capsule, except for **6** → **7** which proceeds in solution outside of the cage. Thin solid and dotted lines denote reactions previously reported in solution. Republished with permission of John Wiley & Sons, from D. J. Cram, M. E. Tanner, R. Thomas, *Angew. Chem. Int. Ed.* **1991**, 30, 1024-1027.; permission conveyed through Copyright Clearance Center, Inc.

Figure 1.6: Hoskins and Robson's cationic MOF. a) The ligand 4,4',4'',4'''-tetracyanotetraphenylmethane binds monovalent copper. Anion (tetrafluoroborate) not shown. b) Crystal structure of MOF, copper atoms being green, carbon grey and nitrogen blue. Guests and anions are not shown as they were unmodeled. Reprinted (adapted) with permission B. F. Hoskins, R. Robson, *J. Am. Chem. Soc.* **1990**, 112, 1546-1554. Copyright 1993, American Chemical Society.

Figure 1.7: Yaghi's original isorecticular MOFs (IRMOFs). a) The ligands used in Yaghi's synthesis of isorecticular MOF materials. b) Crystal structures of the corresponding non-interpenetrated MOFs, with the yellow spheres representing the void spaces which confer porosity to the material. Figures from M. Eddaoudi, J. Kim, N. Rosi, D. Vodak, J. Wachter, M. O'Keeffe, O. M. Yaghi, *Science* **2002**, 295, 469-472. Reprinted with permission from AAAS.

Figure 1.8: Overview of ZIF bonding geometry and the resulting structures which can be accessed. a) The metal-imidazolate-metal bonding angle is roughly 145°, which is similar to the silicon-oxygen-silicon bonding angle in silicates. b) Zeolitic imidazolate frameworks (ZIFs) reported by Yaghi based on divalent zinc and cobalt nodes. Figures reproduced from K. S. Park, Z. Ni, A. P. Côté, J. Y. Chaoi, R. Huang, F. J. Uribe-Romo, H. K. Chae, M. O'Keeffe, O. M. Yaghi, *Proc. Natl. Acad. Sci. U.S.A.* **2006**, 103, 10186-10191. Copyright 2006 National Academy of Sciences.

Figure 1.9: AFFIVE-1-Ni is useful for the separation of H₂S and CO₂ from CH₄. a) AFFIVE-1-Ni captures hydrogen sulfide and carbon dioxide with equal efficiency in a stream of methane, due to an ideal balance between pore size and chemical functionality. b) AFFIVE-1-Ni binding carbon dioxide (top) and hydrogen sulfide (bottom); positions of guests optimized by density functional theory. Reprinted by permission from Youssef Belmabkhout *et. al.*: Springer Nature Energy, copyright Y. Belmabkhout, P. M. Bhatt, K. Adil, R. S. Pillai, A. Cadiou, A. Shkurenko, G. Maurin, G. Liu, W. J. Koros, M. Eddaoudi, *Nat. Energy* **2018**, *3*, 1059-1066.

Figure 1.10: The postsynthetic modification of the aldehyde-functionalized ZIF-90 proceeds by suspension of the ZIF in methanolic NaBH₄ or ethanolamine to produce alcohols and imines, respectively, with the preservation of crystallinity and overall framework structure. Reprinted (adapted) with permission from W. Morris, C. J. Doonan, H. Furukawa, R. Banerjee, O. M. Yaghi, *J. Am. Chem. Soc.* **2008**, *130*, 12626-12627. Copyright 2008 American Chemical Society.

Figure 1.11: Isostructural sodalite-topology ZIFs have varying formation enthalpies based on the functionality installed on the 2-position of the imidazolate linker.

Figure 1.12: Correlation between the Hammett σ -para⁺ parameter of imidazolate 2-substituents and the stability of the ZIFs they compose.

Figure 1.13: a) A shaker mill, a popular type of mill for laboratory-scale mechanochemistry. b) A poly(methylmethacrylate) milling jar loaded with solid reactant and two stainless steel milling balls. Shaking happens laterally, as shown by the arrows, at frequencies up to 30 Hz.

Figure 1.14: *In situ* PXRD allows for the detection of *kat* phase Zn(MeIm)₂ during milling. a) PXRD waterfall plot of the conversion of Zn(MeIm)₂ from SOD to *kat* to *dia* phases during milling. b) Plot of relative intensities for each phase over time during milling Reprinted by permission from Thanassis Katsenis *et. al.*: Springer Nature Communications, copyright A. D. Katsenis, A. Puškarić, V. Štrukil, C. Mottillo, P. A. Julien, K. Užarević, M. Pham, T. Do, S. A. J. Kimber, P. Lazić, O. Magdysyuk, R. E. Dinnebier, I. Halasz, T. Friščić, *Nat. Commun.* **2015**, *6*, 6662.

Chapter 2: A hexameric halogen-bonded phosphonium salt cage for encapsulation and solid-state transformation of small-molecule carbonyl compounds

Figure 2.1: Overview of XB cage based on **1, and its molecular guests.** a) The salt (dibromomethyl)triphenylphosphonium bromide, **1**. b) Chemical diagram of the hexameric cage based on **1**. c) Electrostatic surface potential (ESP) map of the cation (dibromomethyl)triphenylphosphonium cation at an 0.0025 a.u. isosurface level. d) Single crystal X-ray structure of **1**•MeCN with the acetonitrile guest omitted. Top half of the cage is displayed as capped sticks, bottom half shown in space fill mode. e) Guest molecules included in cage. f) Guest molecules included in cage which can react with the cage *via* milling with base.

Figure 2.2: The salt **1** recrystallized from hot liquid guest produces cage-type inclusion compounds whose structures could be solved by single crystal x-ray diffraction. Bulk powders grown in the same fashion show PXRD patterns which match those simulated from the crystal structures, confirming their phase purity.

Figure 2.3: For most **1**•guest materials, thermogravimetric analysis (TGA) of the powdered samples in an atmosphere of nitrogen reveals a mass loss at temperatures between 75 °C and 175 °C, which is interpreted as to the loss of **guest** molecules from the cage. Guest loadings can be calculated from this loss of mass, as

shown in table A.7.1. of Appendix A. TGA thermograms for materials which do not release the guest molecules in one clean step are also included in Appendix A.

Figure 2.4: PXRD patterns of **1•reactive guest** materials compared to the patterns simulated from scXRD structures, when available.

Figure 2.5: Transformations of 1. a) **1•MeCN** can be desolvated to form **1** by exposure to vacuum at 130 °C, and **1** can be solvated by milling with, soaking in, or recrystallization from a guest. b) The **1•reactive guest** materials can be milled with K_2CO_3 to induce a Wittig reaction.

Figure 2.6: Encapsulation of some aldehydes mitigates their volatility. **1•reactive guest** materials containing propionaldehyde, butyraldehyde, and cyclobutanone stabilize these guests to temperatures beyond even their boiling points.

Figure 2.7: **1•butyraldehyde** reacts mechanochemically as part of a one-pot reaction involving olefination followed by Sonogashira coupling to produce a mixture of eneyne and diene-yne products.

Figure 2.8: Overview of structures of 2 and 3. a) Electrostatic surface potential of the (dichloromethyl)triphenylphosphonium cation, **2**, plotted at an 0.0025 a.u. isosurface level. b) Electrostatic surface potential of the (diiodo)triphenylphosphonium cation, **3**, plotted at an 0.0025 a.u. isosurface level. c) Crystal structure of **2**, with one formula unit displayed as a space-fill model, and one formula unit displayed as capped sticks. d) Crystal structure of **4**, which adopts the XB cage structure with nitromethane as the guest.

Figure 2.9: The salt **3** converts to its monoiodinated analogue, **4**, when dissolved in solvent and heated, or left to crystallize in open air for extended periods of time.

Chapter 3: *Ab Initio* metal-organic framework crystal structure prediction reveals elusive copper imidazolate frameworks

Figure 3.1: Generated structures for the putative $Cu(VIm)_2$ framework, plotted based on their relative energies and densities. The structure with the lowest energy, marked in red, is a nonporous *diamondoid*-topology framework.

Figure 3.2. Experimental analysis and structures of $Cu(MeIm)_2$, $Cu(VIm)_2$, and $Cu(AIm)_2$. a) PXRD patterns for bulk microcrystalline ZIFs in comparison with the simulated patterns for their crystal structures as determined by scXRD. b) Chemical scheme for the ZIFs reported herein. c) Crystal structure of $Cu(MeIm)_2$. d) Crystal structure of $Cu(VIm)_2$. e) Crystal structure of $Cu(AIm)_2$.

Figure 3.3. Crystal structures of α - $Cu(AIm)_2$ and β - $Cu(AIm)_2$. The α -phase converts to the β -phase upon impact or ball-milling.

Figure 3.4 Hypergolic testing results for the $Cu(VIm)_2$, α - $Cu(AIm)_2$, and β - $Cu(AIm)_2$ MOFs.

List of Tables

Chapter 2: A hexameric halogen-bonded phosphonium salt cage for encapsulation and solid-state transformation of small-molecule carbonyl compounds

Table 2.1: ^1H NMR conversions for the mechanochemical Wittig reactions between **1** and its **reactive guest**. In all cases, 1.1 equivalents of K_2CO_3 were used as the base. See Appendix section A.9.2. for details of conversion calculations.

Table 2.2: Optimization of reaction conditions for the one-pot conversion of encapsulated aldehydes to *eneyne* and *enediyne* Sonogashira products. Conversions determined by ^1H NMR (see Appendix A, section A.9.3.) All K_2CO_3 was used in its sesquihydrate form, except *as* noted in reaction number 1.

Chapter 3: *Ab Initio* metal-organic framework crystal structure prediction reveals elusive copper imidazolate frameworks

Table 3.1. Calculated combustion energies (ΔE_c), gravimetric energy densities (E_g) and volumetric energy densities (E_v) as calculated by CASTEP DFT code for $\text{Cu}(\text{MeIm})_2$, $\text{Cu}(\text{VIm})_2$, and $\text{Cu}(\text{AIm})_2$.

Introduction

1.1 General Introduction

The reactions of solids have, traditionally, been of secondary concern in the chemical sciences. The notion that substances should be first dissolved in a solvent before they react has long prevailed among chemists, and the origins of that viewpoint has been suggested to date back as early as the 4th century BCE when Aristotle wrote, "... it is chiefly the liquid substances which react".¹ A vast majority of reported chemical transformations have involved solvent, and much of chemists' time and energy are placed, both in the laboratory and in industry, on the handling, storage, and recovery of the quantities of solvent which are used to enable chemical reactions.² However, there is an ongoing revival of interest in solid-state chemical transformations, especially given the increasing awareness among chemists of the environmental costs associated with bulk solvent use.

Central to the understanding of the reactions of solids are not only their molecular or chemical structures, but also their solid-state crystal structures. The weak, non-covalent forces which bind molecules in the solid state include Van der Waals forces, hydrogen bonding, non-directional Coulombic interactions, halogen bonds (XB), and more. Decades of effort to design solid crystalline materials based on these and other supramolecular interactions has produced the field of crystal engineering which, according to Desiraju, concerns "the understanding of intermolecular interactions in the context of crystal packing and in the utilization of such understanding in the design of new solids with desired physical and chemical properties".³ Using this control of crystal packing to address, specifically, issues related to the reactivity of solids has been an ongoing challenge in the crystal engineering community. This Thesis will present two new sets of materials which have been engineered, by both their chemical identity and crystal structures, to be functional and potentially useful materials.

1.2 Reactions of crystalline organic solids

It was around the turn of the 20th century that the photodimerizations of coumarins,⁴ cinnamic acids,⁵ and anthracene⁶ were reported, marking some of the earliest examples of photo-induced

solid-state organic transformations in the chemical literature. With the subsequent development of X-ray diffraction methods for structural characterization of crystalline solids, researchers began to relate the crystal structures of organic molecules to their photoreactivity. In solution, reacting species move mostly freely and rely on molecular collisions to initiate reactions, while species which are in a crystalline environment are pre-arranged in a way which can completely govern their reactivity with other components of the crystal. Some of the earliest attempts to explore this concept as it relates to cinnamic acids were reported by de Jong in 1923,⁷ and a deeper analysis has been produced by Gerhardt M. J. Schmidt, one of the pioneers of solid-state photochemistry. Schmidt's extensive work correlating crystal structure and reactivity revealed that olefins must be both parallel and within 4.2 Å in order to react upon irradiation, a set of rules which have become commonly known as the *topochemical postulates*.⁸ Such fundamental studies relating the crystal structures of organic materials to their reactivities in the solid-state have flourished and have been extended to transformations including the Diels-Alder reaction,⁹ [4+4] photocyclizations,¹⁰ and more.¹¹

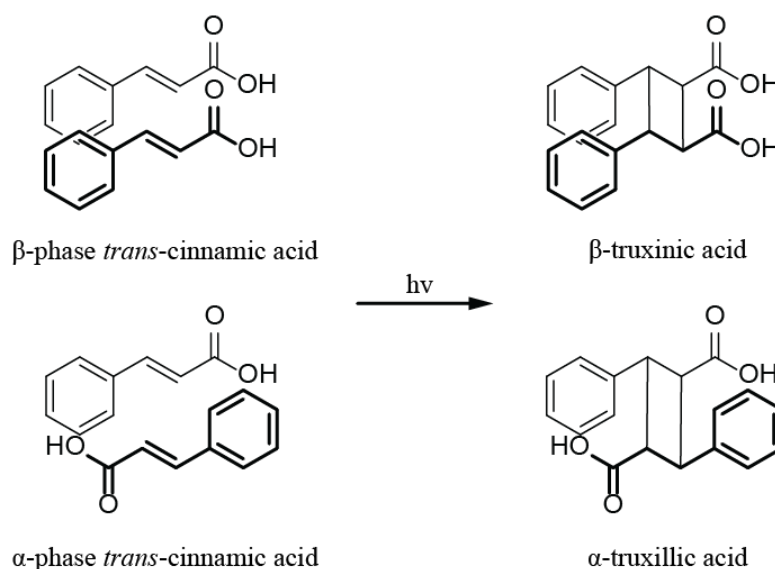


Figure 1.2: Polymorphs of *trans*-cinnamic acid undergo [2+2] photodimerization according to their crystal packing, as articulated by de Jong,⁷ and Schmidt's topochemical postulates.⁸

Resulting from the systematic studies of the structures and reactivities of cinnamic acids, and from extensive studies of the effects of chemical substituents on the packing of organic molecules in crystals, several simple strategies to steer the self-assembly of photoreactive organic crystals emerged.¹² In particular, methods based on the crystallization of the olefins with other organic

molecules as part of multicomponent crystals, known commonly as cocrystals, offered a powerful way to control the packing and reactivity of the olefins. In cocrystals, two or more components crystallize in fixed stoichiometric ratios to form an extended crystal structure which is distinct from those of the components on their own, offering the opportunity to access solid-state environments where the olefins are arranged spatially to obey the topochemical postulates.

An early effort to arrange olefins for photoreaction by the formation of multicomponent crystals is based on a host-guest strategy originally devised by the Toda group in 1968.¹³ In a representative study, the olefins benzylideneacetophenone or dibenzylideneacetone were cocrystallized with rigid hosts which had a “wheel-and-axle” molecular shape.¹⁴ The authors supposed that this particularly-shaped molecule would have difficulty forming a dense-packed crystal structure in the solid state and would, therefore, be particularly susceptible to crystallization with complementary molecules. In the case of these olefin guests, crystallization with the “wheel-and-axle” host molecules yielded structures where the olefins moieties of each guest were arranged appropriately, between the hosts, to undergo photoreaction during irradiation, in a stereoselective manner.¹⁵ Importantly, the guest olefins in their pure crystalline forms were poorly photoreactive which was explained by the unsuitable arrangement of olefin functionalities, and the products which did form were of diverse stereochemistries. Toda’s group extended this concept by using chiral host molecules to effect the enantioselective photodimerization of coumarin and thiocoumarin in a single-crystal-to-single-crystal (SCSC) fashion.¹⁶ (Fig. 1.2)

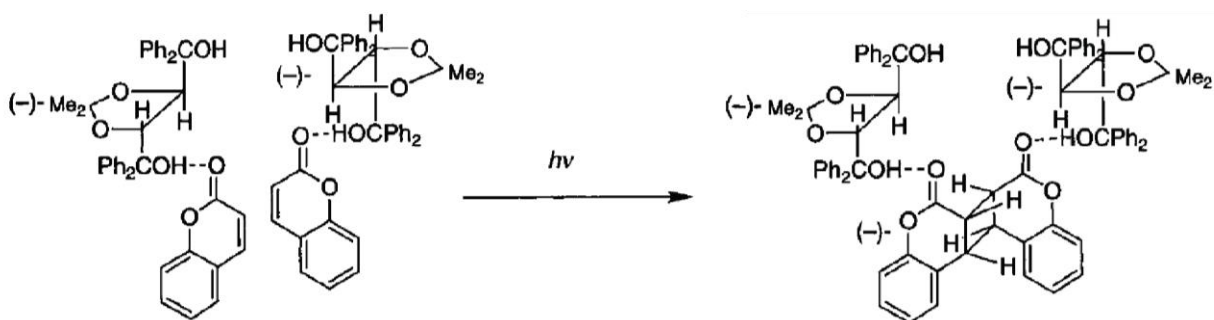


Figure 1.2: The host (R,R)-(-)-trans-2,2-dimethyl-1,3-dioxacyclopentane forms an inclusion complex with coumarin, arranging the two coumarin molecules such that an enantioselective [2+2] photodimerization is possible in the solid-state. Republished with permission of John Wiley & Sons, from K. Tanaka, F. Toda, E. Mochizuki, N. Yasui, Y. Kai, I. Miyahara, K. Hirotsu, *Angew. Chem. Int. Ed.* **1999**, *38*, 3523-3525.; permission conveyed through Copyright Clearance Center, Inc.

An alternative approach to arranging olefins for photoreactions in the crystalline solid state, using a resorcinol as a hydrogen-bonding template to bring pyridine-functionalized molecules into close

contact, was presented by the MacGillivray group.¹⁷ The use of a template enabled molecules with multiple potentially reactive olefin sites to be aligned suitably for photodimerization reactions to produce synthetically challenging molecules including paracyclophanes¹⁷ and ladderanes¹⁸ which, in solution, would be difficult or even impossible to achieve. This strategy is particularly notable due to its ready applicability to a wide range of olefinic systems, regardless of their size or shape; templating of molecular reactivity in this way only concerns the ‘head’ and ‘tail’ of the reactive molecules and only requires that there be appropriate hydrogen-bond acceptors in these positions. In this way, extending the reactive substrates to long and conjugated systems was made possible, and the physical length of the substrates was not a limiting factor in the design of effective templates.

The ability to use crown ethers as supramolecular templates able to arrange olefins bearing positively-charged substituents suitably for a [2+2] photodimerization was shown by the Stoddart group.¹⁹ In particular, a large crown ether molecule, designated BPP34C10, was found to surround two ammonium-functionalized stilbene molecules and create a “bundled” supramolecular complex ready for high-conversion photodimerization. Similarly, cyclodextrins have been used as cavitands to bring coumarin and substituted coumarin molecules into close contact by cocrystallization in the solid state.²⁰ (Fig. 1.3) While no X-ray structural analysis has been provided of these cyclodextrin complexes, stereoselective photodimerizations were made possible for some coumarins which would otherwise not react in such a manner, which was rationalized by the inclusion of coumarins as guests within cyclodextrin cavitands or dimeric cyclodextrin capsules. Similar behavior was in some cases also seen in solution, providing evidence that the molecular recognition and assembly between coumarins and cyclodextrins also exists in a liquid environment.

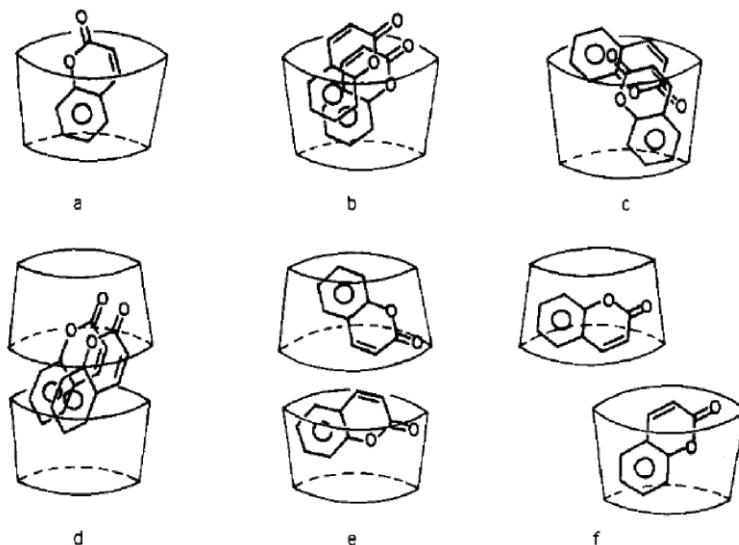


Figure 1.3: Possible orientations of coumarin as cocrystallized with cyclodextrins, as imagined by Weiss. Figure reproduced from reference X. Reprinted (adapted) with permission from J. N. Moorthy, K. Venkatesan, R. G. Weiss, *J. Org. Chem.* **1993**, *57*, 3292-3297. Copyright 1993, American Chemical Society.

The solid-state reactions of single crystals have been exploited for the creation of functional materials. For example, the [2+2] photodimerization has been used to produce diffraction gratings within a single crystal by Enkelmann and coworkers.²¹ Single crystals of a styrylpyrylium salt undergo an intermolecular photodimerization and the accompanying thermal back-reaction to the monomer. Both processes occur in a single-crystal-to-single-crystal (SCSC) fashion, allowing for cycling between monomer and dimer within a single crystal without destroying it. By exposing a single crystal of the monomer to 633 nm laser light shone through an optical interference grating, a pattern of the monomer and dimer layers within the single crystal could be made, producing a spatially-resolved solid solution of the monomer and the dimer within the same crystal. (Fig. 1.4) Different indices of refraction for each layer meant the crystal could, itself, act as a laser diffraction grating and that the thermal back-reaction could be kinetically probed by monitoring the decay of diffracted light by the crystal as it was heated. This particularly applied example of a solid-state photoreaction relied both on the molecular design of a species whose photoreaction was readily reversible, but also on the crystal engineering of the same species such that the topochemical postulates were fulfilled.

While photodimerization reactions have been highly popular subjects of study in solid-state chemistry, other types of transformations have also been explored. For example, the

heteromolecular SCSC Diels-Alder reactions within multicomponent crystals was studied by the Kochi group.⁹ Whereas all of the previously mentioned solid-state reactions are homomolecular, involving the reaction of a molecule with another molecule of the same kind, the authors found that the cocrystallization of an electron donor/acceptor pair as charge-transfer complexes enabled a heteromolecular solid-state Diels-Alder reaction. In particular, the charge-transfer complex of anthracene and bis(ethylimino)-1,4-dithiin was found to crystallize with the molecules arranged in donor-acceptor pairs pre-organized for thermally-induced [4+2] cycloaddition.

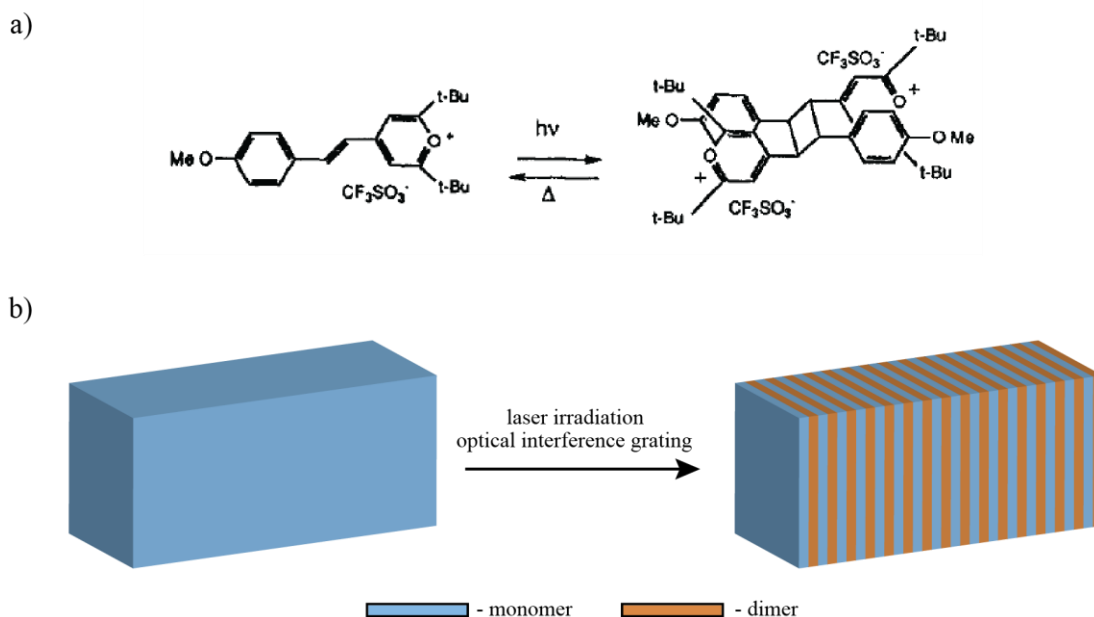


Figure 1.4: Overview of [2+2] photodimerization and its use to form a diffraction grating. a) A styrylpyrylium salt undergoes thermally reversible photodimerization; single crystals of the monomer and dimer will interconvert while preserving monocrystallinity. Reprinted (adapted) with permission from W. Köhler, K. Novak, V. Enkelmann, *J. Chem. Phys.* **1994**, *101*, 10474-10480. Copyright 1994, AIP publishing. b) Single crystals can be converted to diffraction gratings by careful irradiation to create spatially resolved solid solutions of monomer and dimer in a “layer” format.

Interestingly, the single crystals of dimer produced by irradiation adopted a crystal structure which was clearly related to the structure of the cocrystal before irradiation, contrasting to the dimer solid form recrystallized from solution which exhibited another, entirely unrelated, crystal structure. This result highlights the potential SCSC reactions to access crystalline forms of materials which are not obtained by solution crystallization.

1.3 Supramolecular encapsulation

The molecular recognition processes which define the arrangement of reactive substrates in a crystal structure are also of consequence in solution. A popular strategy for harnessing the directive power of molecular recognition in solution has been the molecular inclusion of reactive substrates in capsules, cavitands, or other supramolecular assemblies in order to control, probe, or modulate their reactivity. This method has, so far, provided access to chemical isomerizations,²² decarbonylations,²³ pericyclic reactions,²⁴ and other reactions which are either accelerated or entirely enabled by molecular inclusion in the solid state or in solution.

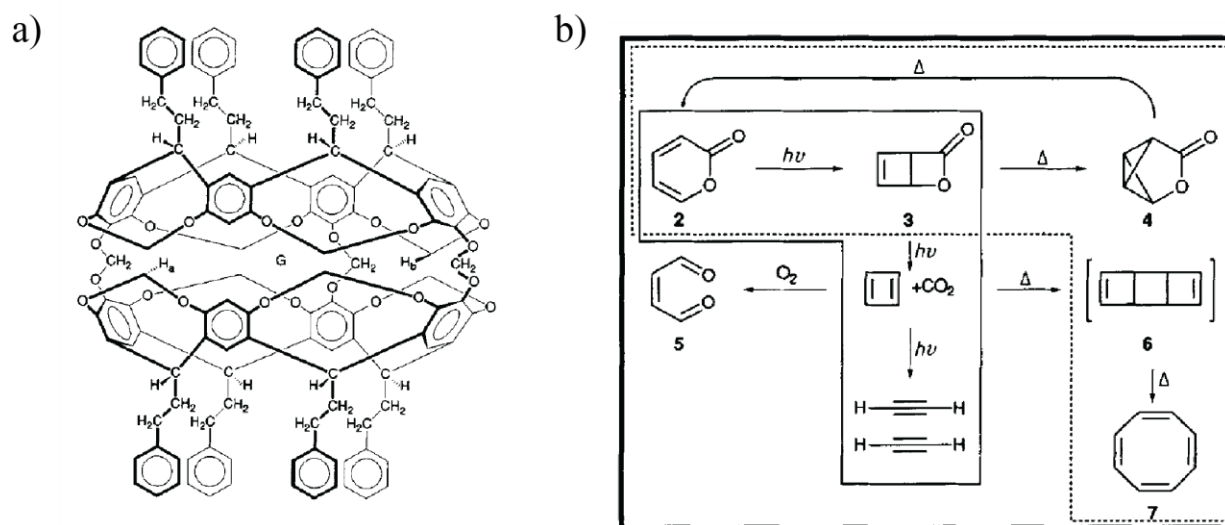


Figure 1.5: Cram's capsule and the reactions performed within. a) Cram's hemicarceplex encapsulating guest **G**, decorated with $\text{CH}_2\text{CH}_2\text{Ph}$ groups to improve solubility. b) All reactions shown were performed inside the inner cavity of the molecular capsule, except for $6 \rightarrow 7$ which proceeds in solution outside of the cage. Thin solid and dotted lines denote reactions previously reported in solution. Republished with permission of John Wiley & Sons, from D. J. Cram, M. E. Tanner, R. Thomas, *Angew. Chem. Int. Ed.* **1991**, *30*, 1024-1027.; permission conveyed through Copyright Clearance Center, Inc.

In 1991, Nobel Laureate Donald J. Cram reported a striking example of the power of molecular inclusion to provide access to otherwise elusive chemical species. By incarcerating α -pyrone in a molecular capsule, its photoproduct, cyclobutadiene, could be obtained inside the capsule in quantitative yields by irradiation of the complex with a xenon arc lamp in solution, evident by immediate analysis by ^1H nuclear magnetic resonance spectroscopy.²⁵ Moreover, the nascent cyclobutadiene could be further reacted to produce acetylene (*via* further irradiation) or malealdehyde (*via* diffusion of dioxygen into the complex) within the capsule. This ability to

generate and observe cyclobutadiene, which is notoriously difficult to isolate and highly reactive, was ascribed to the chemically-isolated and spatially-discrete nature of the interior cavity of the molecular capsule, which was termed the “inner phase” by the authors and was likened to a new state of matter.²⁶

A related approach to catalyze Diels-Alder reactions in solution was reported by Rebek.²⁷ In this approach, the reaction was performed in the presence of dimeric hydrogen-bonded capsules which freely associated and dissociated around both solvent and reaction substrate molecules. For example, reactions between dissolved *p*-quinone and cyclohexadiene substrates were accelerated considerably, by up to two orders of magnitude, upon the addition of this dimeric capsule to the reaction mixture. Rather than by stabilizing or enabling a transition state, the increase in rate was rationalized as an effect of the ability of the capsule to increase the effective concentration of the reactants by bringing them in proximity. In fact, the authors calculated the concentration of two reactant molecules within the capsule given its volume to be 5 M. In practice, this means that the capsules would be able to increase the reaction rates of any reaction mixture where the reactive species existed in concentrations less than this threshold. This work can be seen as a natural extension of Cram’s idea that the interior of a molecular or supramolecular capsule represents an alternative state of matter, where physical confinement dominates and can be harnessed to stabilize molecular species or to direct reactivity.

1.4 Metal-organic materials

While hydrogen bonding and other noncovalent interactions are powerful tools for organizing molecules in the solid state, the coordination bond between a metal atom and an organic ligand has also proven useful for this purpose, given the predictability and directionality of this type of bonding. Since Werner’s early descriptions of “double salts” and his revolutionary conception of the coordination sphere,²⁸ chemists have expanded the scope of the coordination bond to create remarkable functional materials with properties as diverse as porosity,²⁹ catalytic activity,³⁰ and chemical sensing.³¹

The Fujita group, for instance, took advantage of the well-defined geometry of palladium(II) coordination to design a molecular cage where six metal ions form the corners of an octahedral

capsule, with large and planar organic ligands forming coordination bonds to the ions and also forming the faces of the supramolecular octahedron.³² By modification of the ligands, a cup-shape cavitand of similar shape could be synthesized. These structures were found to dramatically accelerate the [2+2] photodimerization of acenaphylenes and naphthoquinones when these molecules were incorporated as guests in the cage or cavitand dissolved in benzene. In many other examples,^{33, 34} the predictable, robust and directional nature of the coordinative bond has been exploited to form useful structural units as part capsules, cavitands, and other complex supramolecular structures. The defining characteristic of such examples is that metal-ligand coordination is used as tool to construct discrete assemblies which can exist either in the solid state, in solution, or both. Fujita termed these materials “ultrafine particles” due to this discrete and nonpolymeric nature.³⁵

In the context of material science, the coordination bond has probably found the most use as a component of polymeric materials known as coordination polymers, which are of one (1D), two (2D) or three dimensions (3D).³⁶ The defining characteristic of these materials is that coordination bonds are part of the polymeric backbone of the material. Due to the labile and reversible nature of coordination bonds when compared to covalent ones, crystals of coordination polymers are typically of high quality due to the self-correcting nature of their polymerization and crystallization.³⁷ This has facilitated characterization of a large variety of coordination polymers by single crystal X-ray diffraction (scXRD), in stark contrast to purely covalent framework materials whose linkages are often less reversible, making the synthesis of corresponding diffraction-quality single crystals inherently more challenging. As a result, only a few examples of scXRD diffraction analyses of covalent organic framework (COFs) materials have been reported so far.^{38,39}

Coordination polymers of practical interest have been known for hundreds of years, even if their structures were not clear to scientists of the time. Prussian blue, the archetypical blue pigment which is also a member of the World Health Organization’s list of essential medicines,⁴⁰ is the mixed-valence compound iron(III) hexacyanoferrate(II).⁴¹ The iron atoms arrange along a 3D cubic lattice in space, each connected to its neighbor by a bridging cyanide anion to form a network with large cavities capable of harboring small molecules as guests. Another early type metal-organic material, Hoffman’s clathrates, were originally synthesized in 1897⁴² and were later found,

by X-ray diffraction, to be comprised of 2D diammonia-nickel(II) tetracyanonickelate(II) sheets which can accommodate neutral organic guest molecules between them in the solid-state.⁴³

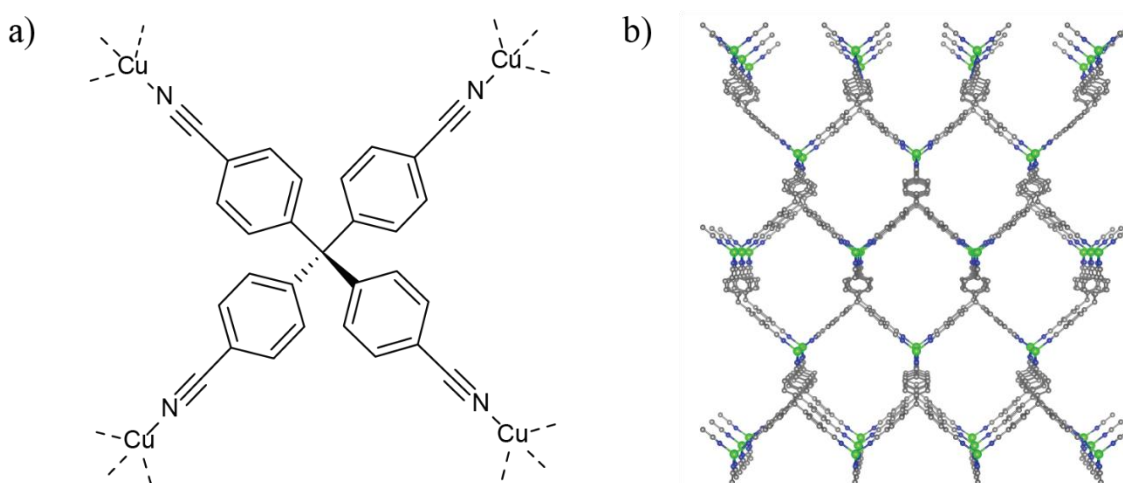


Figure 1.6: Hoskins and Robson's cationic MOF. a) The ligand 4,4',4'',4'''-tetracyanotetraphenylmethane binds monovalent copper. Anion (tetrafluoroborate) not shown. b) Crystal structure of MOF, copper atoms being green, carbon grey and nitrogen blue. Guests and anions are not shown as they were unmodeled. Reprinted (adapted) with permission B. F. Hoskins, R. Robson, *J. Am. Chem. Soc.* **1990**, *112*, 1546-1554. Copyright 1993, American Chemical Society.

In 1990, Hoskins and Robson expanded the field of coordination polymers as a product of their investigation of the solid-state structures of zinc(II) and cadmium(II) cyanides, which form interpenetrated networks which each resemble the structure of diamond.⁴⁴ This team hypothesized that replacing the cyanide anions with large and rigid organic molecules functionalized with cyanide groups to coordinate metals could produce materials which were similar in connectivity to the simple metal cyanides, but with larger voids resulting from the use of larger “rod-like” ligands. By reacting monovalent copper tetrafluoroborate with the ligand 4,4',4'',4'''-tetracyanotetraphenylmethane in solution, crystals of the target cationic framework were obtained with disordered nitrobenzene and tetrafluoroborate anions as guests within the open cavities of the material. This approach of pairing metal or metal-cluster “nodes” with organic “linkers” opens a nearly limitless set of possibilities given the diversity of metal nodes, metal clusters, and organic linkers which can be selected to produce open, porous, or otherwise useful materials. Naturally, the field of MOFs has exploded due to this diversity of form and function, and the topic remains one of the most popular in materials science.

In 1999, the group of Omar Yaghi, one of the pioneering scientists in the field of MOFs, reported the first example of a MOF whose voids could be emptied without the structural degradation of the host framework, opening the possibility of permanent porosity in these materials.⁴⁵ Taking advantage of known metal carboxylate cluster chemistry,⁴⁶ ditopic 1,4-benzenedicarboxylate linkers were used to bind oxygen-centered Zn_4O cluster nodes into a cubic framework of repeat distance 12.94 Å. This was achieved by exposure of a zinc salt, an acid linker precursor, and hydrogen peroxide to triethylamine in a solution of DMF and chlorobenzene to produce single crystals of the target framework. The resulting material, known as MOF-5, could be soaked in chloroform to replace the DMF in the pores, and the newly-incorporated chloroform could then be completely removed from the framework by exposure of the material to vacuum at room temperature. The washing was sufficiently gentle to preserve the single crystals for re-analysis by scXRD, which revealed a host framework identical to that of the as-synthesized material, but with the absence of significant electron density in the voids. Moreover, nitrogen gas-sorption measurements showed that the material was sufficiently absorptive to rival known zeolite materials in measured porosity with a measured Langmuir surface area of 2900 m² g⁻¹.

The Yaghi group generalized the design of this type of MOF material by expanding the set of organic linkers to a group of large and rigid aromatic dicarboxylates with varying shapes, sizes, and chemical functionalities. (Fig. 1.7) The target MOF materials were synthesized using methodologies mostly identical to that used for MOF-5.⁴⁷ In the majority of cases, the 180° angles between carboxylate functionalities for each linker was sufficient to yield materials whose structures mimicked that of MOF-5, *i.e.* were cubic and contained voids, but whose pore size and node cluster spacing varied corresponding to the length of the linker. In other cases, especially for the larger dicarboxylate linkers, interpenetrated nets were formed where the voids of each network were occupied by another copy of an identical network, destroying the potential for permanent porosity. This issue of interpenetration was shown to be resolvable by the dilution of the reaction mixtures for these materials, which produced single crystals of the non-interpenetrated networks. In later works,⁴⁸ this style of chemistry has been termed *reticular chemistry*, meaning the design of chemical materials whose subunits are reticulated, meaning divided or otherwise arranged into a network. The general concept of linking metal ions or clusters with multitopic carboxylate linkers has since been relied on heavily for the design of MOFs, with many popular examples including HKUST-1,⁴⁹ NU-1000,⁵⁰ and MIL-53.⁵¹

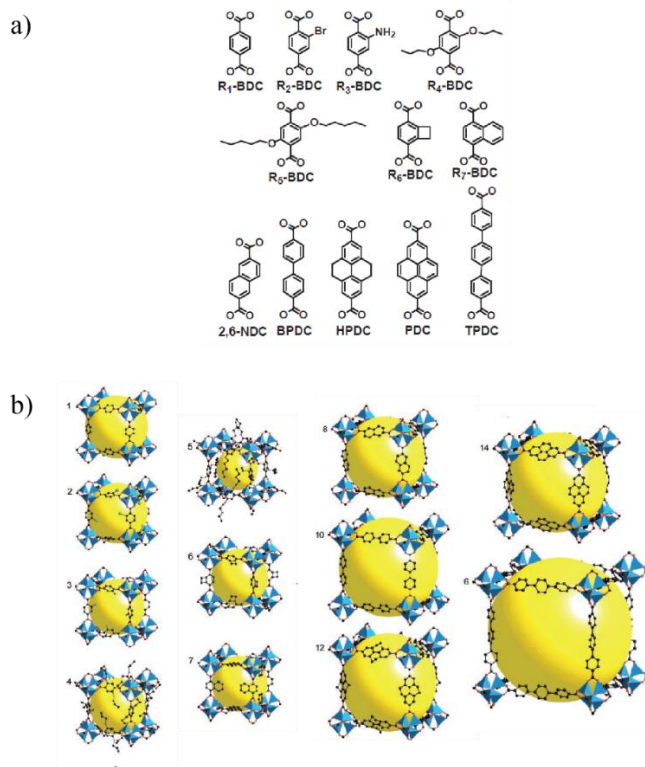


Figure 1.7: Yaghi’s original isorecticular MOFs (IRMOFs). a) The ligands used in Yaghi’s synthesis of isorecticular MOF materials. b) Crystal structures of the corresponding non-interpenetrated MOFs, with the yellow spheres representing the void spaces which confer porosity to the material. Figures from M. Eddaoudi, J. Kim, N. Rosi, D. Vodak, J. Wachter, M. O’Keeffe, O. M. Yaghi, *Science* **2002**, 295, 469-472. Reprinted with permission from AAAS.

Nitrogen-containing organic linkers have also been used extensively for the synthesis of MOFs, with imidazolates and related heterocycles being among the most popular ligand types for this purpose. In 2003, the crystal structure of zinc(II) benzimidazolate was reported. The material was crystallized by diffusion of an ethanolic solution of benzimidazole and 2,2’-bipyridine into one of zinc(II) acetate in concentrated aqueous ammonia.⁵² This produced single crystals that were found to have a structure which was open, had voids, and shared its node and linker connectivity with naturally-occurring zeolite materials. Specifically, the connectivity of the node and linker net, known as *topology*, was an arrangement formally known as the sodalite topology and denoted using the “SOD” label. The Chen group, in follow-up work,⁵³ reported another set of metal imidazolate materials which were open, porous, and whose topologies were diverse and often zeolitic. Yaghi’s team shortly thereafter presented an even larger set of these porous materials⁵⁴ based on zinc(II) and cobalt(II) nodes, which were termed *zeolitic imidazolate frameworks* (ZIFs).

The apparent tendency for zinc(II) and cobalt(II) imidazolates to crystallize with topologies identical to naturally occurring zeolites was rationalized by the Yaghi group to be a consequence of the similar bonding geometry seen for the silicate nodes in zeolites and the metal-ligand interactions in ZIFs. Specifically, the metal-imidazolate-metal angle in ZIFs and the preferred Si-O-Si bonding angle for zeolites are coincident at approximately 145° , with each silicon or metal atom binding its ligands or oxygen atoms in a tetrahedral fashion. It is likely these geometric similarities which are the driving factors which induce zeolitic topologies in metal imidazolates. To date, this trend has held, and many^{55,56} ZIFs have been produced with a diversity of metal nodes and organic linkers.

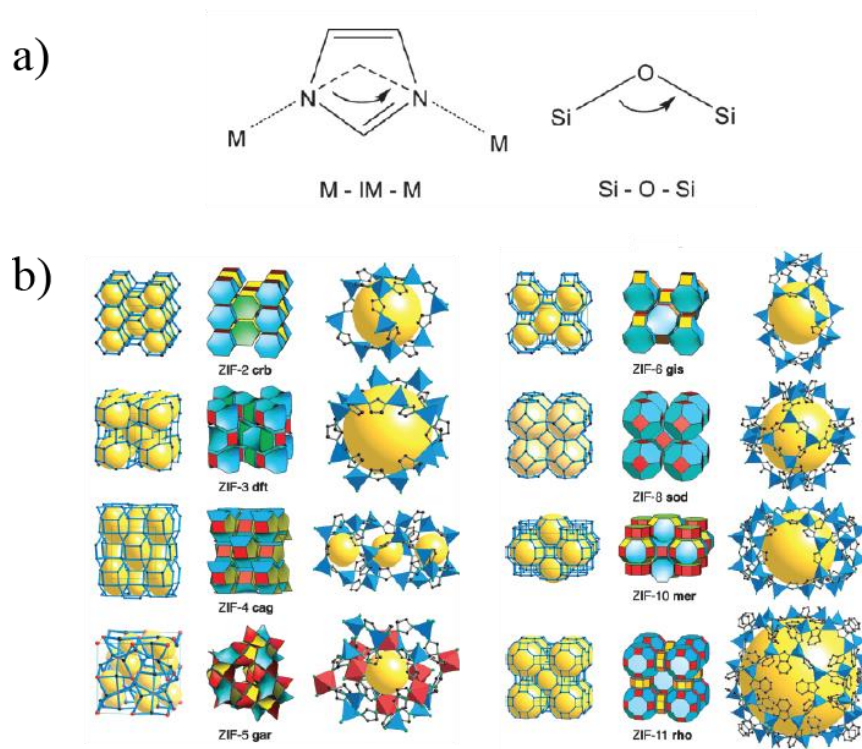


Figure 1.8: Overview of ZIF bonding geometry and the resulting structures which can be accessed. a) The metal-imidazolate-metal bonding angle is roughly 145° , which is similar to the silicon-oxygen-silicon bonding angle in silicates. b) Zeolitic imidazolate frameworks (ZIFs) reported by Yaghi based on divalent zinc and cobalt nodes. Figures reproduced from K. S. Park, Z. Ni, A. P. Côté, J. Y. Chaoi, R. Huang, F. J. Uribe-Romo, H. K. Chae, M. O’Keeffe, O. M. Yaghi, *Proc. Natl. Acad. Sci. U.S.A.* **2006**, *103*, 10186-10191. Copyright 2006 National Academy of Sciences.

1.5 Applications of MOFs

The porosity of MOFs is likely their most exploited physical property.⁵⁷ Applications for MOFs are often based on their ability to absorb guest molecules for their capture, storage, and transport or to effect physical guest separation. Even in the earliest reports of permanently porous MOF materials, the initial report of MOF-5 for instance,⁴⁵ nitrogen gas sorption measurements were usually included as part of characterization due to the obvious suitability of MOFs towards the absorption and accommodation of guest species. To date, MOFs have been designed for the absorption of N₂,⁵⁸ CO₂,⁵⁹ CH₄,⁶⁰ SO₂,⁶¹ H₂O,⁶² and many others.⁶³

Designing MOFs which absorb certain chemical species selectively over others can provide materials which are useful for purification or the physical separation of chemical mixtures. Selective absorption by MOFs is enabled by the exceptional tunability inherent to these materials because of their node and linker construction. Specifically, careful modification of the linker length or chemical functionality can change the pore and void size of a MOF, or change its chemical affinity towards a specific guest, respectively. Altering the metal node can also affect absorption selectivity of the MOF material, especially if there are open and unsaturated metal sites in the material with which the guest may interact.⁵⁷

The Eddaoudi group reported a set of fluorinated MOF materials with high selectivity towards CO₂ and H₂S in a medium of concentrated CH₄.⁶⁴ The removal of the acid gases CO₂ and H₂S from CH₄ is a common step in the purification of crude natural gas, and MOFs with the ability to strip these gases from a stream of methane could provide a more simple and cost-effective solution than existing methods for this purpose. A material reported previously⁶⁵ by their group, AIFIVE-1-Ni, was found to capture CO₂ and H₂S with equal selectivity, enabling simultaneous scrubbing of these two gasses from a methane stream. AIFIVE-1-Ni is a pillared MOF related to the SIFSIX class of framework materials and is comprised of two dimensional sheets of nickel ions bridged by pyrazine which are connected by AlF₆⁻² pillars to form a three-dimensional network. This equal selectivity for capturing CO₂ and H₂S was rationalized by considering the pore size of the material, which was intermediate, sufficiently large to allow the entry of H₂S but small enough to confine CO₂ effectively.

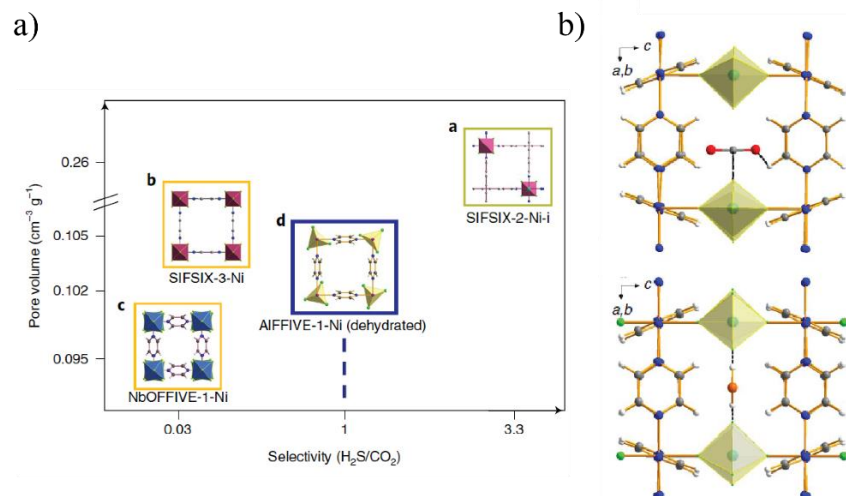


Figure 1.9: AFFIVE-1-Ni is useful for the separation of H₂S and CO₂ from CH₄. a) AFFIVE-1-Ni captures hydrogen sulfide and carbon dioxide with equal efficiency in a stream of methane, due to an ideal balance between pore size and chemical functionality. b) AFFIVE-1-Ni binding carbon dioxide (top) and hydrogen sulfide (bottom); positions of guests optimized by density functional theory. Reprinted by permission from Youssef Belmabkhout *et. al.*: Springer Nature Energy, copyright Y. Belmabkhout, P. M. Bhatt, K. Adil, R. S. Pillai, A. Cadiau, A. Shkurenko, G. Maurin, G. Liu, W. J. Koros, M. Eddaoudi, *Nat. Energy* **2018**, 3, 1059-1066.

MOFs have also been used as substrates for chemical reactivity in the crystalline solid state, demonstrating solid-state reaction unlike those of reactive organic molecules discussed earlier in this Thesis. Whereas organic crystals typically react in a fashion where one molecule reacts with another adjacent member of the crystal, the porosity inherent to many MOFs allows for the introduction of reactive guest molecules which can functionalize the crystalline material in a homogenous way throughout the entire volume of the MOF crystal. One of the most simple examples of this concept is the hydration of open metal sites in a MOF which has unsaturated metal centers as nodes. For example, HKUST-1, a MOF based on the paddlewheel motif which copper(II) ions adopt when coordinated by carboxylate ligands,⁴⁹ exists in a dehydrated form which can be completely and homogeneously hydrated when exposed to humidity or moisture, while the material retains its overall structure and porosity.

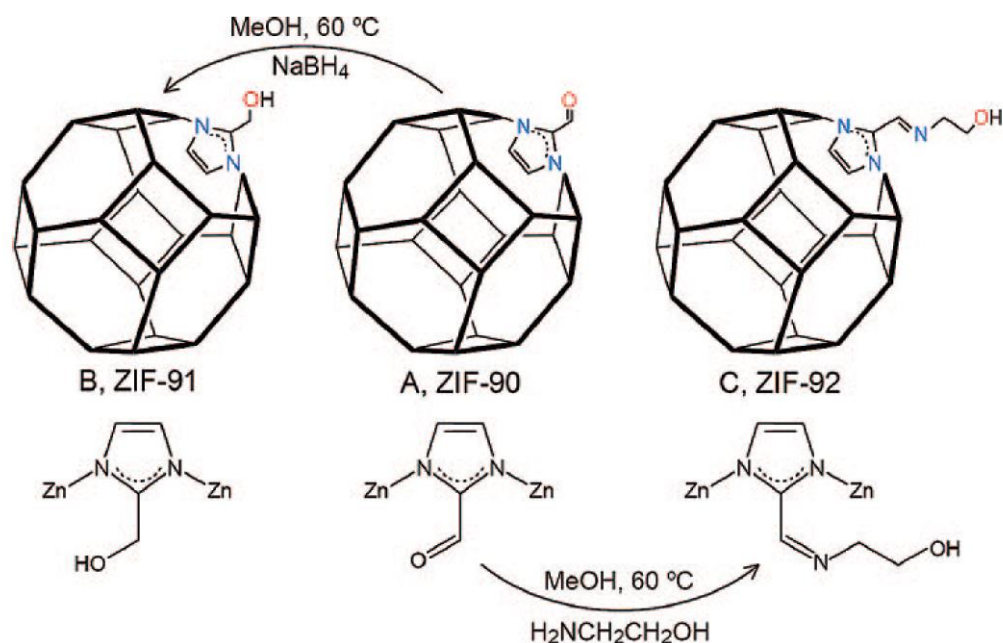


Figure 1.10: The postsynthetic modification of the aldehyde-functionalized ZIF-90 proceeds by suspension of the ZIF in methanolic NaBH₄ or ethanolamine to produce alcohols and imines, respectively, with the preservation of crystallinity and overall framework structure. Reprinted (adapted) with permission from W. Morris, C. J. Doonan, H. Furukawa, R. Banerjee, O. M. Yaghi, *J. Am. Chem. Soc.* **2008**, *130*, 12626-12627. Copyright 2008 American Chemical Society.

More sophisticated examples of such behavior involve the covalent modification of the linker of a MOF with the preservation of the structure of the material. In 2009, a ZIF composed of tetrahedral zinc nodes and imidazolate linkers functionalized with an aldehyde moiety on the 2-position was reported.⁶⁶ This material, designated ZIF-90, was found to be porous and upon exposure to NaBH₄ in methanol underwent the reduction of the aldehydes to alcohol groups in approximately 80% conversion, as confirmed by ¹³C cross polarization/magic angle spinning solid state nuclear magnetic resonance (CP/MAS SSNMR) and by solution ¹H NMR of the material after digestion in dilute DCl in D₂O. Crucially, this solid-state transformation took place with the preservation of crystallinity in the sample as confirmed by PXRD. The pristine ZIF-90 could also be exposed to ethanolamine in methanol at 60 °C for 3 hours to induce the imine condensation of the aldehyde functionalities with the amine in solution. Unlike for the reduction of the aldehyde group, this transformation was quantitative as confirmed by both NMR and Fourier-transform infrared (FTIR) spectroscopy.

This work was one of the early reports which presented crystalline MOFs as crystalline and macroscopic equivalents to molecules in solution, susceptible to covalent modification by simple exposure to a reagent or reactive species. Key to this concept of “crystals as molecules” is the permanent porosity of these materials, which allows for the reactive species to diffuse into the framework and cause complete and homogenous chemical transformation. Post-synthetic modification (PSMs) of this type has also been used to generate MOFs with catalytic applications. The MOF (Fe)MIL-101-NH₂, a MOF based on iron(III) metal clusters bridge by 2-aminoterephthalic acid nodes, was modified by reacting it with a pyridine-2-carboxaldehyde-nickel(II) complex, in solution, to form the corresponding nickel-coordinated imine functionality in place of the dangling amine groups of the MOF.⁶⁷ The nickel(II)-functionalized MOF could act as a catalyst for the dimerization of ethylene to form 1-butene and did so with higher conversion than many known nickel-based catalysts previously developed for this purpose, including the simple molecular equivalent to the modified MOF, Ni(bipy)Cl₂.

Recently, our group has reported the design of ZIFs for potential applications in the aerospace industry which relies on the solid-state reactivity of these materials, namely their ability to ignite when exposed to an oxidizer.⁶⁸ Hypergolic materials are central to aerospace propulsion, where they allow for the automatic ignition of fuel upon contact with an oxidizer in a rocket motor. Traditionally, hypergolic fuels have been based on the hydrazine functionality, and are correspondingly carcinogenic, environmentally deleterious, and difficult to handle. It is this fact which inspires ongoing efforts to design and produce hypergolic materials which are less toxic and environmentally damaging than hydrazines.

Replacing the 2-methylimidazolate linkers of the well-known ZIF-8 with imidazolates containing vinyl- and ethynyl- substituents on the 2-position results in MOFs with the same SOD topology, but with the added property of hypergolic ignition upon exposure to white fuming nitric acid (WFNA). The substitution of the tetrahedral zinc metal node of these materials with cobalt(II) or cadmium nodes also preserves the SOD-topology of the framework, but modulates their hypergolicity with cobalt(II)-based materials performing the best. This set of six ZIFs exhibited varying hypergolic performances, defined by the delay between the contact of the oxidizer with the MOF and the first signs of ignition. This quantity is known as the ignition delay (ID) and lower values indicate higher performance. Computational methods based on density functional theory

(DFT) showed that these hypergolic ZIFs had combustion energies between 16.1 and 19.7 kJ/g, which rivals traditional hypergolic fuels like hydrazine (19.5 kJ/g) and traditional energetic materials like trinitrotoluene (TNT) (14.9 kJ/g).⁶⁸

1.6 Energy and stability of MOFs

The quest to design more stable MOFs is a core component of the more general goal to produce framework materials with large scale applications, since the stability and persistence of the chemical and crystalline structure of a MOF is typically a requirement for their real-life application. Traditional methods to design MOFs which are stable have included careful matching of ligand and metal according to hard-soft acid-base theory (HSAB).⁶⁹ For example, the combination of high-valency *hard* metal cations with *hard* carboxylate bases has been a popular method for the creation of stable MOFs. This method of high-valency also allows for the inclusion of more anionic ligands, increasing the coordination metal sites, thereby increasing stability further. Pairing *soft* nitrogen-containing organic ligands with *soft* cations like divalent zinc or cobalt has also been popular and lead to highly stable materials like the prototypical ZIF-8.⁵⁴ Techniques like the introduction of hydrophobic moieties to the linkers of MOFs has also been used as a method to increase MOF stability by occluding chemically incompatible substances, like water, from the pores and interior of the MOF.⁷⁰

However, a particularly troublesome and not yet addressed problem in the field of MOFs is polymorphism, the ability of a material to adopt multiple crystal structures given a single chemical composition. This phenomenon is typified in the ZIF systems involving tetrahedral zinc nodes and imidazolate linkers functionalized on the 2-position with methyl or ethyl substituents. Early work⁵³ on these materials based on 2-methylimidazole and 2-ethylimidazole showed that they adopt the porous zeolitic topologies SOD and RHO, respectively, and later work showed that these materials could also be made to adopt dense, nonporous diamondoid⁷¹ (*dia*) and quartz⁷² (*qtz*) topologies. A third phase of intermediate density has also been reported for each of the two systems, the novel katsenite⁷³ (*kat*) topology for zinc(II) methylimidazole and the analcime (ANA) topology in the case of zinc(II) ethylimidazolate.⁵³

In order to understand the energetics which underly the existence of these polymorphs, isothermal dissolution calorimetry in dilute acid was performed on these materials. This analysis revealed the formation enthalpies of each material and showed that, commensurate with the conventional wisdom that open and porous materials are inherently unstable, an increase in polymorph framework density corresponds to an increase in thermodynamic stability.⁷⁴ While this work confirmed that denser MOF materials are likely to be more stable than their porous counterparts, it offers no solution to the question of how one can design functional porous materials with enhanced stability, resistant to polymorphic conversion to higher density forms.

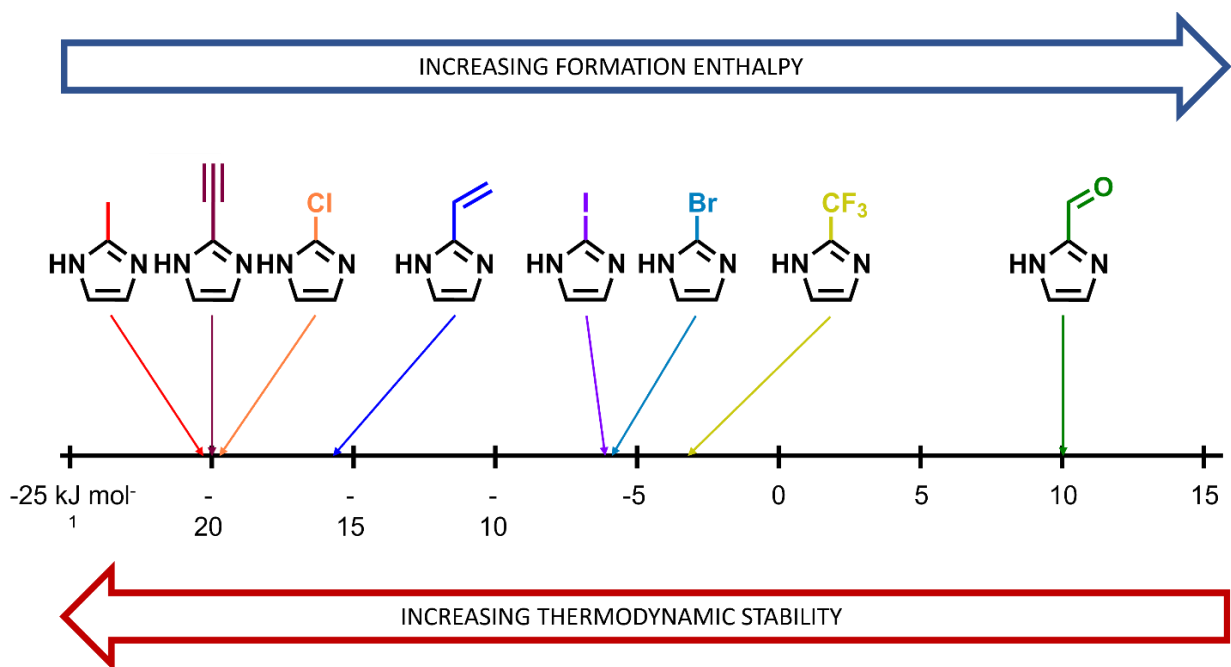


Figure 1.11: Isostructural sodalite-topology ZIFs have varying formation enthalpies based on the functionality installed on the 2-position of the imidazolate linker.

Later work in our group investigated the relationship between linker chemical functionality and ZIF stability for a limited set of isostructural and porous sodalite-topology ZIFs.⁷⁵ By incorporating a set of diversely 2-substituted imidazolate linkers into ZIFs which all adopt the sodalite topology, the effect of linker substituent on the formation enthalpies of each ZIF could be determined. Ultimately, the electron donating or withdrawing character of a substituent, quantified by its Hammett parameters, was found to correlate with ZIF thermodynamic stability. Specifically, an increasing Hammett parameter, which corresponds to the increased electron-withdrawing character of that substituent, results in an increase of the enthalpy of formation for the

corresponding ZIF. This makes intuitive sense; as the substituent increasingly withdraws electron density from the imidazolate ring, the ability of the imidazolate ring to donate electron density into the metal-ligand bond is decreased, destabilizing the framework. This work is notable because it reveals, for the first time, a quantitative relationship between the thermodynamic stability of a framework solid and the electronic properties of the ligands which compose it. This was enabled by the study of isostructural materials, controlling for the effect of crystal structure on framework energy and allowing the direct observation of ligand properties on ZIF stability. This work may also provide a potential rule-of-thumb for the design of stable ZIFs: imidazolate ligands can be appended with electron donating groups to increase the electron-rich nature of the rings and strengthen their bonding with metal nodes.

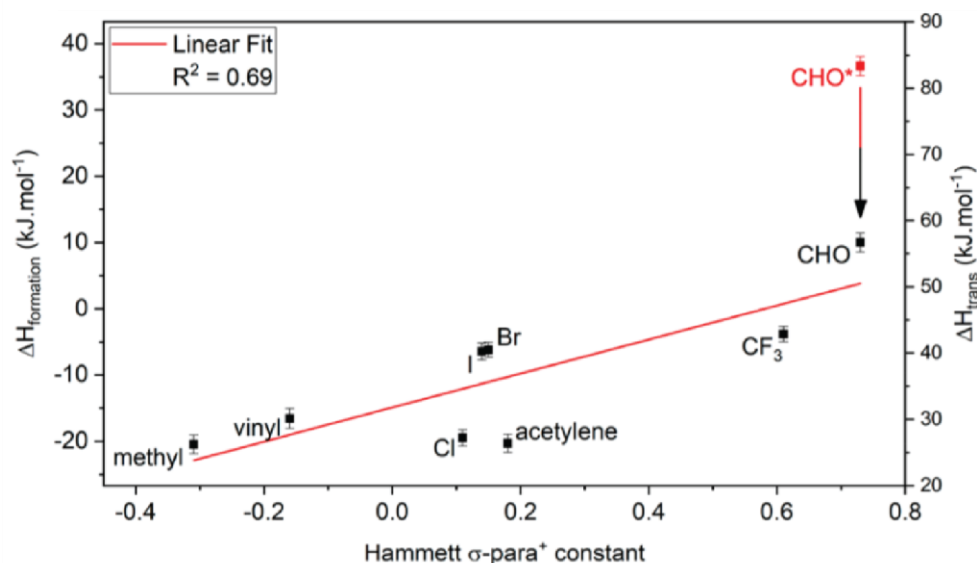


Figure 1.12: Plot demonstrating the correlation between the enthalpy of formation of the 8 isostructural ZIFs and the Hammett σ_{para^+} constant of the corresponding linker 2-substituent for each ZIF.

1.7 Mechanochemistry

Mechanochemistry refers to chemical and materials transformations which are initiated or sustained by the application of mechanical force and can be realized by manual grinding with a mortar and pestle, ball-milling, planetary milling, or twin-screw extrusion, among many other approaches.^{76,77} Mechanochemistry is not a new methodology, with roots traceable to Theophrastus' description of the production of mercury metal by grinding cinnabar with vinegar

in a copper mortar⁷⁶ and, much later, reports in the 1890s from M. C. Lea which investigated the effect of grinding on metal halides⁷⁸ There has, in the last 20 years, been a revival of the technique in the fields of organic and materials chemistry driven, in large part, by the increasing interest of chemists in the development of cleaner, more sustainable chemical processes. Since mechanochemistry usually requires very small amounts of or no solvent at all, it is a promising method for the development of synthesis which produces minimal solvent waste. Increasingly, work in the field of mechanochemistry has proven the technique to be useful as a synthetic tool in its own right, providing access to some molecules or materials which are otherwise difficult or impossible to obtain.⁷⁹

The mechanochemical transformations detailed in the experimental sections of this Thesis are all carried out by ball-milling in an oscillating shaker mill, which is one of the most popular methods for laboratory-scale mechanochemistry. In this arrangement, reactants are loaded into a jar with milling balls which is then sealed and shaken at a frequency between 25 and 30 Hz. This action causes the intimate mixing and crushing of solid reactants, and often allows for the direct reaction between two solid materials. In some cases, a small amount of liquid additive is included which can either accelerate or fully enable a reaction. The ratio between the solid reactants and this liquid additive has been quantified by the parameter η , defined as the volume of liquid (μl) divided by the total mass of solid in the milling vessel (mg).⁸⁰ Typically, such liquid-assisted grinding (LAG) experiments are conducted at η -values less than $1 \mu\text{l mg}^{-1}$

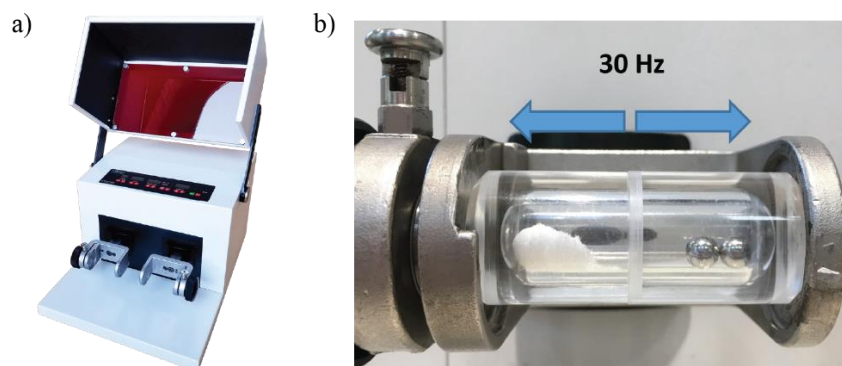


Figure 1.13: a) A shaker mill, a popular type of mill for laboratory-scale mechanochemistry. b) A poly(methylmethacrylate) milling jar loaded with solid reactant and two stainless steel milling balls. Shaking happens laterally, as shown by the arrows, at frequencies up to 30 Hz.

The synthesis of MOFs by mechanochemical methods has been studied extensively, with synthesis of popular MOFs like ZIF-8,⁷² HKUST-1,⁸¹ MOF-74,⁸² and UiO-66⁸³ having been reported previously in the literature. In this context, mechanochemistry has enabled the discovery of MOFs which were otherwise elusive. For example, Katsenis and coworkers explored the mechanochemical synthesis of ZIF-8 using *in situ* powder X-ray diffraction and revealed the existence of a then-unknown form of Zn(MeIm)₂, displaying a new topology which was assigned the name *katsenite*.⁷³ Despite ZIF-8 being one of the most popular and well-studied MOF systems in the literature, only the sodalite (SOD) and the more dense diamondoid (*dia*) topology forms had been reported in the literature, highlighting the power of mechanochemistry, especially when coupled to *in situ* analysis methods, to discover materials and phases which do not readily avail themselves during solution experiments.

Mechanochemistry was also proven to be an efficient tool for the preparation of organic molecules, sometimes enabling synthetic pathways which are not readily accessed in solution. A particularly instructive example of this is the dimerization of C₆₀ fullerene by mechanochemical means in the presence of KCN.⁸⁴ While in solution the reaction of fullerene and KCN provides a cyanated fullerene after workup, mechanochemical milling of KCN and fullerene produced dimers of C₆₀ instead. In another salient example, a molecule which was claimed in the literature to be impossible to synthesize due to steric hindrances, *tert*-butyl-substituted adamantoid phosph(III)azane, was made easily by solvent-free mechanochemical synthesis.⁸⁵ Milling a precursor macrocycle with a salt additive, *i.e.* lithium chloride, resulted in the isomerization of the molecule to the adamantoid analogue in quantitative conversion after only 90 minutes, a transformation which has been entirely impossible to replicate by solution methods.

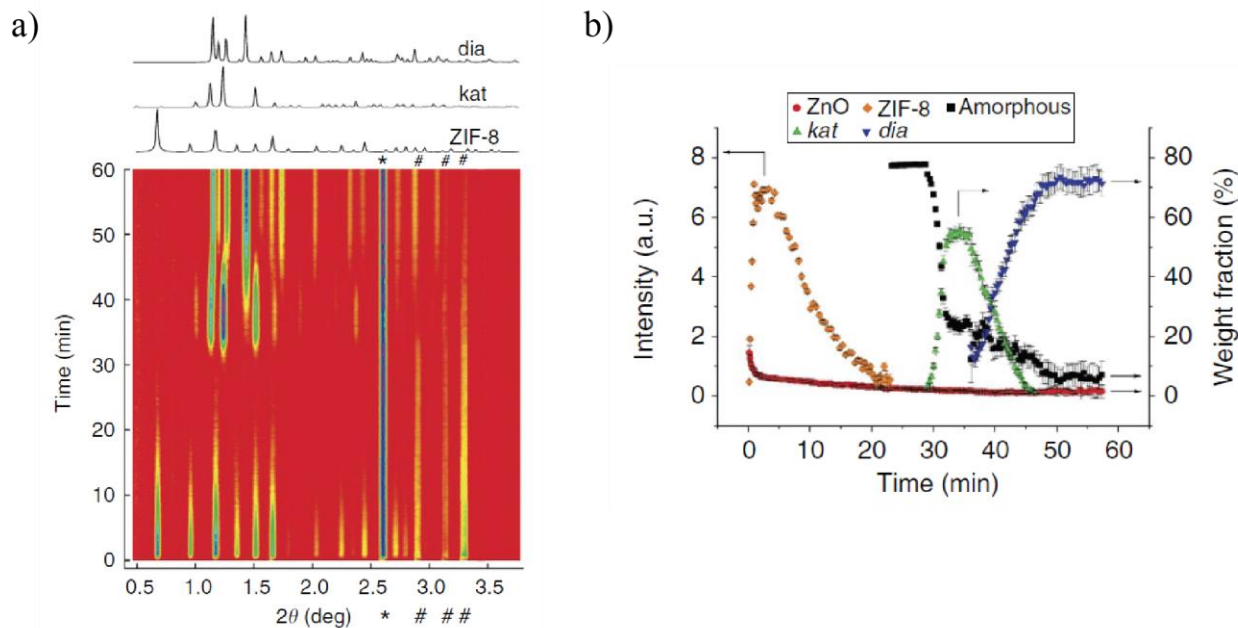


Figure 1.14: *In situ* PXRD allows for the detection of *kat* phase $\text{Zn}(\text{MeIm})_2$ during milling. a) PXRD waterfall plot of the conversion of $\text{Zn}(\text{MeIm})_2$ from SOD to *kat* to *dia* phases during milling. b) Plot of relative intensities for each phase over time during milling Reprinted by permission from Thanassis Katsenis *et. al.*: Springer Nature Communications, copyright A. D. Katsenis, A. Puškarić, V. Štrukil, C. Mottillo, P. A. Julien, K. Užarević, M. Pham, T. Do, S. A. J. Kimber, P. Lazić, O. Magdysyuk, R. E. Dinnebier, I. Halasz, T. Friščić, *Nat. Commun.* **2015**, *6*, 6662.

Classical synthetic pathways can also be accessed by mechanochemistry to improve efficiency and reduce or entirely eliminate the need for solvent. Diels-Alder reactions,⁸⁶ Schiff base condensations,⁸⁷ Huisgen couplings,⁸⁸ Sonogashira reactions,⁸⁹ Suzuki reactions,⁹⁰ Negishi reactions,⁹¹ Heck reactions,⁹² palladium catalyzed CH/CH oxidative couplings,⁹³ cyclopropanations,⁹⁵ Wittig olefinations,⁹⁵ organic oxidations⁹⁶ and reductions,⁹⁷ and many more have been performed in the solid-state *via* mechanochemistry, and the development of strategies to adapt known solution reactions to mechanochemistry is widening area.

The mechanochemical Wittig olefinations and Sonogashira reactions are particularly relevant to Chapter 2 of this Thesis, where they are used to transform components of a multicomponent crystal. In 2001, Balema and coworkers reported the mechanochemical Wittig olefination of aromatic aldehydes in high yield.⁹⁵ The reactive ylides necessary for reaction with the aldehydes were generated *in situ* by the exposure of phosphonium salts to potassium carbonate during milling. It was noted that the deprotonation of the specific phosphonium salts used in this work was enabled by mechanochemistry and would have been impossible in solution without the use of

stronger bases. In 2009, the Mack group reported the first example of the palladium-catalyzed cross-coupling of aryl halides with terminal acetylene groups, known commonly as the Sonogashira reaction.⁹⁰ While couplings using a copper(I)-based cocatalyst gave high yields, the omission of such as cocatalyst reduced the yields dramatically. By replacing the stainless steel milling balls and jars with those made of metallic copper, the yields could be restored to levels which matched those of the reactions performed using the copper cocatalyst. In this way, the Mack group provided one of the earliest examples of a mechanochemical transformation which was catalyzed by the material of the milling vessel and media. Chapter 2 of this Thesis will expand on these two reactions under mechanochemical conditions as part of a strategy where reaction components are pre-formulated as a multicomponent crystal before reaction.

References

1. C. Reichardt, T. Welton, *Solvents and Solvent Effects in Organic Chemistry*, Oxford University Press, Oxford, **1998**.
2. D. J. C. Constable, C. Jimenez-Gonzalez, R. K. Henderson, *Org. Process Res. Dev.* **2007**, *11*, 133-137.
3. G. R. Desiraju, *Angew. Chem. Int. Ed* **1995**, *34*, 2311-2327.
4. G. Ciamician, P. Silber, *Chem. Ber.* **1903**, *36*, 4266-4272.
5. C. N. Rieber, *Chem. Ber.* **1902**, *35*, 2908-2909.
6. R. Luther, F. Weigert, *Z. Phys. Chem. (Leipzig)* **1905**, *51*, 297-328.
7. A. W. K. de Jong, *Ber. Dtsch. Chem. Ges.* **1923**, *56*, 818.
8. G. M. J. Schmidt, *Pure Appl. Chem.* **1971**, *27*, 647-678.
9. J. H. Kim, S. V. Lindeman, J. K. Kochi, *J. Am. Chem. Soc.* **2001**, *123*, 4951-4959.
10. S. Kohmoto, Y. Ono, H. Masu, K. Yamaguchi, K. Kishikawa, M. Yamamoto, *Org. Lett.* **2001**, *3*, 4153-4155.
11. A. Matsumoto, K. Sada, K. Tashiro, M. Miyata, T. Tsubouchi, T. Tanaka, T. Odani, S. Nagahama, T. Tanaka, K. Inoue, S. Saragai, S. Nakamoto, *Angew. Chem. Int. Ed.* **2002**, *41*, 2502-2505.
12. L. R. MacGillivray, G. S. Papaefstathiou, in *Encyclopedia of Supramolecular Chemistry: Solid-State Chemistry/Topochemistry* (eds. J. L. Atwood and J. W. Steed), Marcel Dekker Inc., New York, **2004**, pp.1316-1321.
13. F. Toda, K. Akagi, *Tetrahedron. Lett.* **1968**, *33*, 3695-3698.
14. F. Toda, D. L. Ward, H. Hart, *Tetrahedron Lett.* **1981**, *22*, 3865-3868.
15. F. Toda, K. Tanka, A. Sakikawa, *Chem. Commun.* **1987**, *4*, 279-280.
16. K. Tanaka, F. Toda, E. Mochizuki, N. Yasui, Y. Kai, I. Miyahara, K. Hirotsu, *Angew. Chem. Int. Ed.* **1999**, *38*, 3523-3525.
17. L. R. MacGillivray, J. L. Reid, J. A. Ripmeester, *J. Am. Chem. Soc.* **2000**, *122*, 7817-7818.
18. X. Gao, T. Friščić, L. R. MacGillivray, *Angew. Chem. Int. Ed.* **2003**, *43*, 232-236.

19. D. G. Amirsakis, M. A. Garcia-Garibay, S. J. Rowan, J. F. Stoddart, A. J. P. White, D. J. Williams, *Angew. Chem. Int. Ed.* **2001**, *40*, 4256-4261.
20. J. N. Moorthy, K. Venkatesan, R. G. Weiss, *J. Org. Chem.* **1993**, *57*, 3292-3297.
21. W. Köhler, K. Novak, V. Enkelmann, *J. Chem. Phys.* **1994**, *101*, 10474-10480.
22. T. Iwasawa, E. Mann, J. Rebek, *J. Am. Chem. Soc.* **2006**, *128*, 9308-9309.
23. C. L. D. Gibb, A. K. Sundaresan, V. Ramamurthy, B. C. Gibb, *J. Am. Chem. Soc.* **2008**, *130*, 4069-4080.
24. J. Kang, J. Rebek, *Nature* **1997**, *385*, 50-52
25. D. J. Cram, M. E. Tanner, R. Thomas, *Angew. Chem. Int. Ed.* **1991**, *30*, 1024-1027.
26. J. C. Sherman, D. J. Cram, *J. Am. Chem. Soc.* **1989**, *111*, 4527-4528.
27. J. Kang, G. Hilmersson, J. Santamaría, J. Rebek, *J. Am. Chem. Soc.* **1998**, *120*, 3650-3656.
28. A. Werner, *Z. Anorg. Allg. Chem.* **1893**, *3*, 267-330.
29. I. M. Hönicke, I. Senkovska, V. Bon, I. A. Baburin, N. Bönisch, S. Raschke, J. D. Evans, S. Kaskel, *Angew. Chem. Int. Ed.* **2018**, *57*, 13780-13783.
30. A. H. Chughtai, N. Ahmad, H. A. Younus, A. Laypkov, F. Verpoort, *Chem. Soc. Rev.* **2015**, *44*, 6804-6849.
31. S. Zhao, J. Yang, Y. Liu, J. Ma, *Inorg. Chem.* **2016**, *55*, 2261-2273.
32. M. Yoshizawa, Y. Takeyama, T. Kusukawa, M. Fujita, *Angew. Chem. Int. Ed.* **2002**, *41*, 1347-1349.
33. S. Mirtschin, A. Slabon-Turski, R. Scopelliti, A. G. Velders, K. Severin, *J. Am. Chem. Soc.* **2010**, *132*, 14004-14005.
34. W. Cullen, M. C. Misuraca, C. A. Hunter, N. H. Williams, M. D. Ward, *Nat. Chem.* **2016**, *8*, 231-236.
35. M. Fujita, D. Oguro, M. Miyazawa, H. Oka, K. Yamaguchi, K. Ogura, *Nature* **1995**, *378*, 469-471.
36. S. Kitagawa, R. Kitaura, S. Noro, *Angew. Chem. Int. Ed.* **2004**, *43*, 2334-2375.
37. R. E. Morris, L. Brammer, *Chem. Soc. Rev.* **2017**, *46*, 5444.
38. T. Ma, E. A. Kapustin, S. X. Yin, L. Liang, Z. Zhen, J. Niu, L. Li, Y. Wang, J. Su, J. Li, X. Wang, W. D. Wang, W. Wang, J. Sun, O. M. Yaghi, *Science* **2018**, *361*, 48-52.
39. L. Liang, Y. Qiu, W. D. Wang, J. Han, Y. Luo, W. Yu, G. Yin, Z. Wang, L. Zhang, J. Ni, J. Niu, J. Sun, T. Ma, W. Wang, *Angew. Chem. Int. Ed.* **2020**, *59*, 17991-17995.
40. H. J. Buser, D. Schwarzenbach, W. Petter, A. Ludi, *Inorg. Chem.* **1977**, *16*, 2704-2710.
41. World Health Organization. *WHO Model List of Essential Medicines*, **2019**.
42. K. A. Hofmann, F. Küspert, *Z. Anorg. Allg. Chem.* **1897**, *15*, 204.
43. J. H. Rayner, H. M. Powell, *J. Chem. Soc.* **1952**, 319-328.
44. B. F. Hoskins, R. Robson, *J. Am. Chem. Soc.* **1990**, *112*, 1546-1554.
45. H. Li, M. Eddaoudi, M. O'Keeffe, O. M. Yaghi, *Nature* **1999**, *402*, 276-279.
46. W. Clegg, D. R. Harbron, C. D. Homan, P. A. Hunt, I. R. Little, B. P. Straughan, *Inorg. Chim. Acta* **1991**, *186*, 51-60.
47. M. Eddaoudi, J. Kim, N. Rosi, D. Vodak, J. Wachter, M. O'Keeffe, O. M. Yaghi, *Science* **2002**, *295*, 469-472.
48. O. M. Yaghi, *J. Am. Chem. Soc.* **2016**, *138*, 15507-15509.
49. S. S. Y. Chui, M. F. Lo, J. P. H. Charmant, A. G. Orpen, I. D. Williams, *Science* **1999**, *283*, 1148-1150.

50. J. E. Mondloch, W. Bury, D. Fairen-Jimenez, S. Kwon, E. J. DeMarco, M. H. Weston, A. A. Sarjeant, S. T. Nguyen, P. C. Stair, R. Q. Snurr, O. K. Farha, J. T. Hupp, *J. Am. Chem. Soc.* **2013**, *135*, 10294-10297.
51. F. Millange, C. Serre, G. Férey, *Chem. Commun.* **2002**, 822-823.
52. X. Huang, J. Zhang, X. Chen, *Chinese Science Bulletin* **2003**, *46*, 1531-1534.
53. X. Huang, Y. Lin, J. Zhang, X. Chen, *Angew. Chem. Int. Ed.* **2006**, *45*, 1557-1559.
54. K. S. Park, Z. Ni, A. P. Côté, J. Y. Chaoi, R. Huang, F. J. Uribe-Romo, H. K. Chae, M. O’Keeffe, O. M. Yaghi, *Proc. Natl. Acad. Sci. U.S.A.* **2006**, *103*, 10186-10191.
55. M. Arhangelskis, A. D. Katsenis, N. Novendra, Z. Akimbekov, D. Gandrath, J. M. Marrett, G. Ayoub, A. J. Morris, O. K. Farha, T. Frišćić, A. Navrotsky, *Chem. Mater.* **2019**, *31*, 3777-3783.
56. R. Banerjee, A. Phan, B. Wang, C. Knobler, H. Furukawa, M. O’Keeffe, O. M. Yaghi, *Science* **2008**, *319*, 939-943.
57. J. Li, P. M. Bhatt, M. Eddaoudi, Y. Liu, *Adv. Mater.* **2020**, *32*, 2002563-2002563.
58. L. Wang, T. Song, L. Huang, J. Xu, C. Li, C. Ji, L. Shan, L. Wang, *CrystEngComm* **2011**, *13*, 4005-4009.
59. S. Nandi, P. De Luna, T. D. Daff, J. Rother, M. Liu, W. Buchanan, A. I. Hawari, T. K. Woo, R. Vaidhyanathan, *Sci. Adv.* **2015**, *1*, e1500412.
60. Z. Niu, X. Cui, T. Pham, P. C. Lan, H. Xing, K. A. Forrest, L. Wojtas, B. Space, S. Ma, *Angew. Chem. Int. Ed.* **2019**, *58*, 10138-10141.
61. E. Martinez-Ahumada, A. López-Olvera, V. Jancik, J. E. Sánchez-Bautista, E. González-Zamora, V. Martis, D. R. Williams, I. A. Ibarra, *Organometallics* **2020**, *39*, 883-915.
62. S. M. T. Abtab, D. Alezi, P. M. Bhatt, A. Shkurenko, Y. Belmabkhout, H. Aggarwal, L. J. Weseliński, N. Alsadun, U. Samin, M. N. Hedhili, M. Eddaoudi, *Chem* **2018**, *4*, 94-105.
63. X. Wang, W. Xu, J. Gu, X. Yan, M. Guo, G. Zhou, S. Tong, M. Ge, Y. Liu, C. Chen, *Nanoscale* **2019**, *11*, 17782-17790.
64. Y. Belmabkhout, P. M. Bhatt, K. Adil, R. S. Pillai, A. Cadiau, A. Shkurenko, G. Maurin, G. Liu, W. J. Koros, M. Eddaoudi, *Nat. Energy* **2018**, *3*, 1059-1066.
65. A. Cadiau, Y. Belmabkhout, K. Adil, P. M. Bhatt, R. S. Pillai, A. Shkurenko, C. Martineau-Corcós, G. Maurin, M. Eddaoudi, *Science* **2017**, *356*, 731-735.
66. W. Morris, C. J. Doonan, H. Furukawa, R. Banerjee, O. M. Yaghi, *J. Am. Chem. Soc.* **2008**, *130*, 12626-12627.
67. J. Canivet, S. Aguado, Y. Schuurman, D. Farnisseng, *J. Am. Chem. Soc.* **2013**, *135*, 4195-4198.
68. H. M. Titi, J. M. Marrett, G. Dayaker, M. Arhangelskis, C. Mottillo, A. J. Morris, G. P. Rachiero, T. Frišćić, R. D. Rogers, *Sci. Adv.* **2019**, *5*, eaav9004.
69. M. Ding, X. Cai, H. Jiang, *Chem. Sci.* **2019**, *10*, 10209-10230.
70. J. Yang, A. Grzech, F. M. Mulder, T. J. Dingemans, *Chem. Commun.* **2011**, *47*, 5244-5246.
71. Q. Shi, Z. Chen, Z. Song, J. Li, J. Dong, *Angew. Chem. Int. Ed.* **2011**, *30*, 672-675.
72. P. J. Beldon, L. Fábíán, R. S. Stein, A. Thirumurugan, A. K. Cheetham, T. Frišćić, *Angew. Chem. Int. Ed.* **2010**, *49*, 9640-9643.
73. A. D. Katsenis, A. Puškarić, V. Štrukil, C. Mottillo, P. A. Julien, K. Užarević, M. Pham, T. Do, S. A. J. Kimber, P. Lazić, O. Magdysyuk, R. E. Dinnebier, I. Halasz, T. Frišćić, *Nat. Commun.* **2015**, *6*, 6662.
74. Z. Akimbekov, A. D. Katsenis, G. P. Nagabhushana, G. Ayoub, M. Arhangelskis, A. J. Morris, T. Frišćić, A. Navrotsky, *J. Am. Chem. Soc.* **2017**, *139*, 7952-7957.

75. N. Novendra, J. M. Marrett, A. D. Katsenis, H. M. Titi, M. Arhangelskis, T. Friščić, A. Navrotsky, *J. Am. Chem. Soc.* **2020**, *142*, 21720-21729.
76. L. Takacs, *Chem. Soc. Rev.* **2013**, *42*, 7649-7659.
77. S. L. James, C. J. Adams, C. Bolm, D. Braga, P. Collier, T. Friščić, F. Grepioni, K. D. M. Harris, G. Hyett, W. Jones, A. Krebs, J. Mack, L. Maini, A. G. Orpen, I. P. Parkin, W. C. Shearouse, J. W. Steed, D. C. Waddell, *Chem. Soc. Rev.* **2012**, *41*, 413-447.
78. M. C. Lea, *Am. J. Sci.* **1893**, *46*, 413.
79. J. L. Do, T. Friščić, *ACS Cent. Sci.* **2017**, *3*, 13-19.
80. T. Friščić, S. L. Childs, S. A. A. Rizvi, W. Jones, *CrystEngComm* **2009**, *11*, 418-426.
81. M. Klimakow, P. Klobes, A. F. Thünnemann, K. Rademann, F. Emmerling, *Chem. Mater.* **2010**, *22*, 5216-5221.
82. G. Ayoub, B. Karadeniz, A. J. Howarth, O. K. Farha, I. Đilović, L. S. Germann, R. E. Dinnebier, K. Užarević, T. Friščić, *Chem. Mater.* **2019**, *31*, 5494-5501.
83. K. Užarević, T. C. Wang, S. Moon, A. M. Fidelli, J. T. Hupp, O. K. Farha, T. Friščić, *Chem. Commun.* **2016**, *52*, 2133-2136.
84. K. Komatsu, G. Wang, Y. Murata, T. Tanaka, K. Fujiwara, *J. Org. Chem.* **1998**, *63*, 9358-9366.
85. Y. X. Shi, K. Xu, J. K. Clegg, R. Ganguly, H. Hirao, T. Friščić, F. García, *Angew. Chem. Int. Ed.* **2016**, *55*, 12736-12740.
86. Z. Zhang, Z. Peng, M. Hao, J. Gao, *Synlett* **2010**, *19*, 2835-2838.
87. M. Zbačnik, I. Nogalo, D. Cinčić, B. Kaitner, *CrystEngComm* **2015**, *17*, 7870-7877.
88. R. Thorwirth, A. Stolle, B. Ondruschka, A. Wild, U. S. Schubert, *Chem. Commun.* **2011**, *47*, 4370-4372.
89. D. A. Fulmer, W. C. Shearouse, S. T. Mendoza, J. Mack, *Green Chem* **2009**, *11*, 1821-1825.
90. T. Seo, T. Ishiyama, K. Kubota, H. Ito, *Chem. Sci.* **2019**, *10*, 8202-8210.
91. Q. Cao, J. L. Howard, E. Wheatley, D. L. Browne, *Angew. Chem. Int. Ed.* **2018**, *57*, 11339-11343.
92. E. Tillberg, D. Peters, T. Frejd, *J. Organomet. Chem.* **2004**, *689*, 3778-3781.
93. S. Lou, Y. Mao, D. Xu, J. He, Q. Chen, Z. Xu, *ACS Catal.* **2016**, *6*, 3890-3894.
94. L. Chen, M. O. Bovee, B. E. Lemma, K. S. M. Keithley, S. L. Pilson, M. G. Coleman, J. Mack, *Angew. Chem. Int. Ed.* **2015**, *54*, 11084-11087.
95. V. P. Balema, J. W. Wiench, M. Pruski, V. K. Pecharsky, *J. Am. Chem. Soc.* **2002**, *124*, 6244-6245.
96. R. Thorwirth, F. Bernhardt, A. Stolle, B. Ondruschka, J. Asghari, *Eur. J. Chem.* **2010**, *16*, 13236-13242.
97. J. Mack, D. Fulmer, S. Stofel, N. Santos, *Green Chem.* **2007**, *9*, 1041-1043.

Connecting text for Chapter 2

Chapter 2 concerns the solid-state reactivity of inclusion compounds between a molecular guest and its halogen-bonded (XB) supramolecular cage-like host. Whereas the examples of solid-state reactivity detailed in the Introduction of this Thesis concerned the crystal-to-crystal reactions of molecules in the solid state, this work explores an alternative type of reactivity where a host and guest react with each other upon grinding to form molecular products. These materials ultimately illustrate a method for the pre-formulation of a substrate and reagent in appropriate stoichiometry for rapid, on-demand derivatization by simple mechanochemical reaction with a base.

Chapter 2: A hexameric halogen-bonded phosphonium salt cage for encapsulation and solid-state transformation of small-molecule carbonyl compounds

This work corresponds to a manuscript currently in preparation for submission, co-authored by Dr. Hatem M. Titi and Dr. Tomislav Friščić.

2.1 Abstract

We report a hexameric supramolecular cage assembled from the components of a Wittig-type phosphonium salt, held together by charge-assisted R-Br \cdots Br \cdots Br-R halogen bonds. The cage reliably encapsulates small polar molecules, including aldehydes and ketones, to provide host-guest systems in which components are pre-formulated in a near-ideal stoichiometry for a base-activated Wittig olefination in the solid-state. These pre-formulated solids enable a molecular-level “baking powder” approach for solvent-free Wittig reactions, based on a so far unexplored design of solid-state reactivity, in which the host for molecular inclusion also acts as a complementary reagent for the chemical transformation of an array of guests. These solids can also act as supramolecular equivalents to their Wittig olefination products in the context of Sonogashira-type coupling between the nascent gem-dihaloolefins and terminal acetylenes under mechanochemical grinding conditions.

2.2 Intro

Formation of multi-component crystals, such as cocrystals, lattice inclusion compounds and solid solutions, is one of the principal crystal engineering strategies for the design of reactivity of organic solids.¹ Molecular inclusion has provided access to a range of transformations, including photodimerizations,² isomerizations,³ photochemical oxidations,⁴ decarbonylations,⁵ Diels-Alder reactions,⁶ and more.⁷ In the majority of cases, the host molecule or lattice acts as a chemically inert container, with reactivity confined to the included guests.⁸ More recent work in the field of metal-organic frameworks (MOFs) has introduced the concept of a “crystal as a molecule”,

wherein inclusion of a small molecule guest leads to functionalization of a suitably designed host framework.⁹

Here, we present a different and, to the best of our knowledge, so far unexplored approach to the design of reactivity in organic solids, where the host component acts both as a container for inclusion and a reagent for chemical derivatization for a diversity of guests. We show the pre-formulation of two reactants into a single, well-defined crystalline material that can be used for “on demand” solvent-free reactions induced by grinding with solid base.

2.3 Results and discussion

Key to this work is the herein observed ability of the salt (dibromomethyl)triphenylphosphonium bromide $(\text{PPh}_3\text{CHBr}_2)^+\text{Br}^-$ (**1**) to reliably form small molecule inclusion compounds in the solid-state, based on a self-assembled hexameric cages held by charge-assisted halogen bonds (XB). Whereas phosphonium salts of the general type $(\text{PPh}_3\text{CHX}_2)^+\text{X}^-$ ($\text{X} = \text{Cl}, \text{Br}, \text{I}$) have been studied extensively¹⁰ in the context of the Wittig Olefination reaction where they are precursors to synthetically valuable gem-dihaloolefins,¹¹ their structures and solid-state properties have been largely unexplored. Compound **1** was synthesized according to a procedure reported by Wolkoff,¹² and was recrystallized from acetonitrile (MeCN) to give large, colorless crystals. Single crystal X-ray structure analysis revealed that the crystals are composed of hexameric cages, each containing six ordered MeCN molecules, held together by $\text{R}-\text{Br} \cdots \text{Br} \cdots \text{Br}-\text{R}$ halogen bonds as part of a motif entirely unique among the set of reported, mostly dimeric, halogen bonded capsules.¹³ This material (**1**•MeCN) could be readily desolvated by exposure to 130 °C under high vacuum for 12 hours, forming a new phase (**1**) with a distinct powder X-ray diffraction (PXRD) pattern. Dissolution of **1** in hot nitrobenzene followed by slow cooling to room temperature afforded colorless crystals, which were found to be solvent-free $(\text{PPh}_3\text{CHBr}_2)^+\text{Br}^-$ by single crystal X-ray diffraction. The PXRD pattern simulated for the structure of **1** matched to that of the bulk material. Compound **1** was found to reliably form the halogen bonded (XB) cage structure observed in **1**•MeCN. Recrystallization of **1** from a set of 11 additional small-molecule polar liquids (Fig. 1c) provided colorless crystalline solids of **1**•guest whose PXRD patterns were, in all cases, almost identical to that of **1**•MeCN, indicating their isostructurality to it. Diffraction-quality single

crystals were obtained for 9 of these additional materials, revealing the anticipated inclusion of solvent guest into the hexameric cage. In most structures, the guest molecules were sufficiently ordered to reveal six of them located inside the cage, with the electronegative portions of each molecule engaging in short C-H...O or C-H...N (for **1**•MeCN) bonding with the phenyl groups of **1**. In almost all cases, residual electron density was also found at the center of each cage, but could not be modelled, indicating the presence of additional, highly disordered guest.

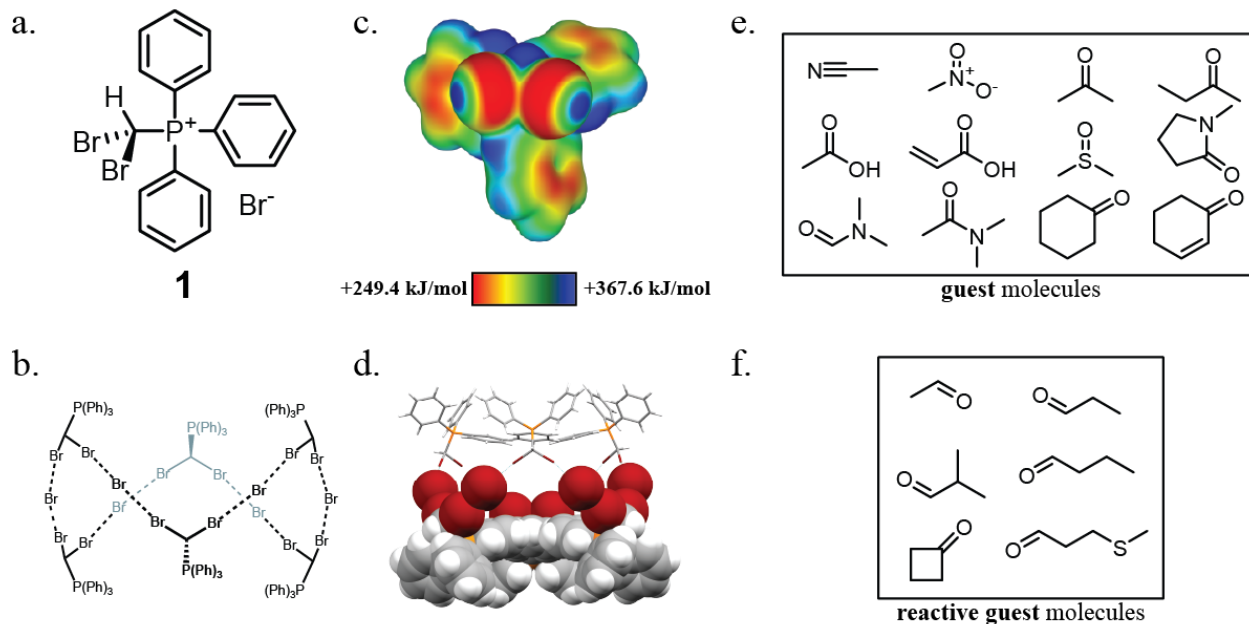


Figure 2.1: Overview of XB cage based on **1, and its molecular guests.** a) The salt (dibromomethyl)triphenylphosphonium bromide, **1**. b) Chemical diagram of the hexameric cage based on **1**. c) Electrostatic surface potential (ESP) map of the cation (dibromomethyl)triphenylphosphonium cation at an 0.0025 a.u. isosurface level. d) Single crystal X-ray structure of **1**•MeCN with the acetonitrile guest omitted. Top half of the cage is displayed as capped sticks, bottom half shown in space fill mode. e) Guest molecules included in cage. f) Guest molecules included in cage which can react with the cage *via* milling with base.

The amount of **guest** included in each hexameric cage was further validated using proton nuclear magnetic resonance spectroscopy (^1H NMR) in CDCl_3 solution and thermogravimetric analysis (TGA). Analysis by ^1H NMR revealed between 6 and 7 **guest** molecules per cage for most **1**•**guest** materials, commensurate with the X-ray single crystal structures, and in support of the presence of additional, heavily disordered guests in some **1**•**guest** materials. Similar results were obtained using TGA, where the amount of included guest was evaluated by the height of the mass loss step observed on heating each **1**•**guest** material under a flow of N_2 . The number of guest molecules per

cage for each **1**•guest material, as determined by NMR and TGA, is tabulated in Appendix A, section A.7.

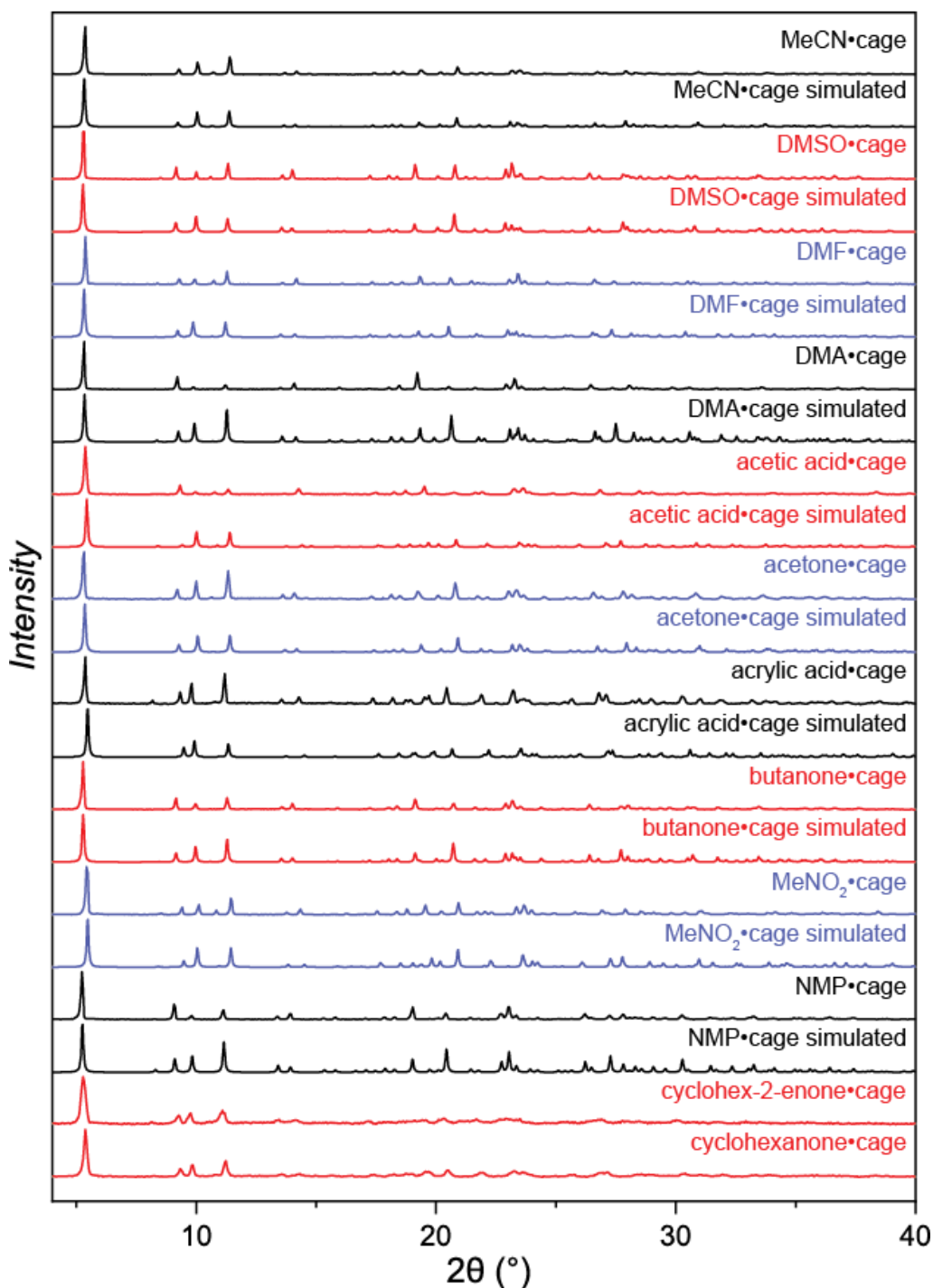


Figure 2.2: The salt **1** recrystallized from hot liquid guest produces cage-type inclusion compounds whose structures could be solved by single crystal x-ray diffraction. Bulk powders grown in the same fashion show PXRD patterns which match those simulated from the crystal structures, confirming their phase purity.

This reliable encapsulation of small polar molecules encouraged us to explore the possibility of encapsulating aldehydes and ketones, the reactive complement to the Wittig-type character of **1**, to create cage-type materials where the guest would be susceptible to controlled chemical modification by its host. Such an arrangement supposes that there is a sufficient barrier to the reaction between the host and guest so that the solid-state complex could be isolated, stored and characterized without spontaneous reaction. In this case, **1** represents a stable precursor to the phosphorus ylide which can react with carbonyl compounds to form olefins and is easily and reliably accessibly by exposure of **1** to a base.

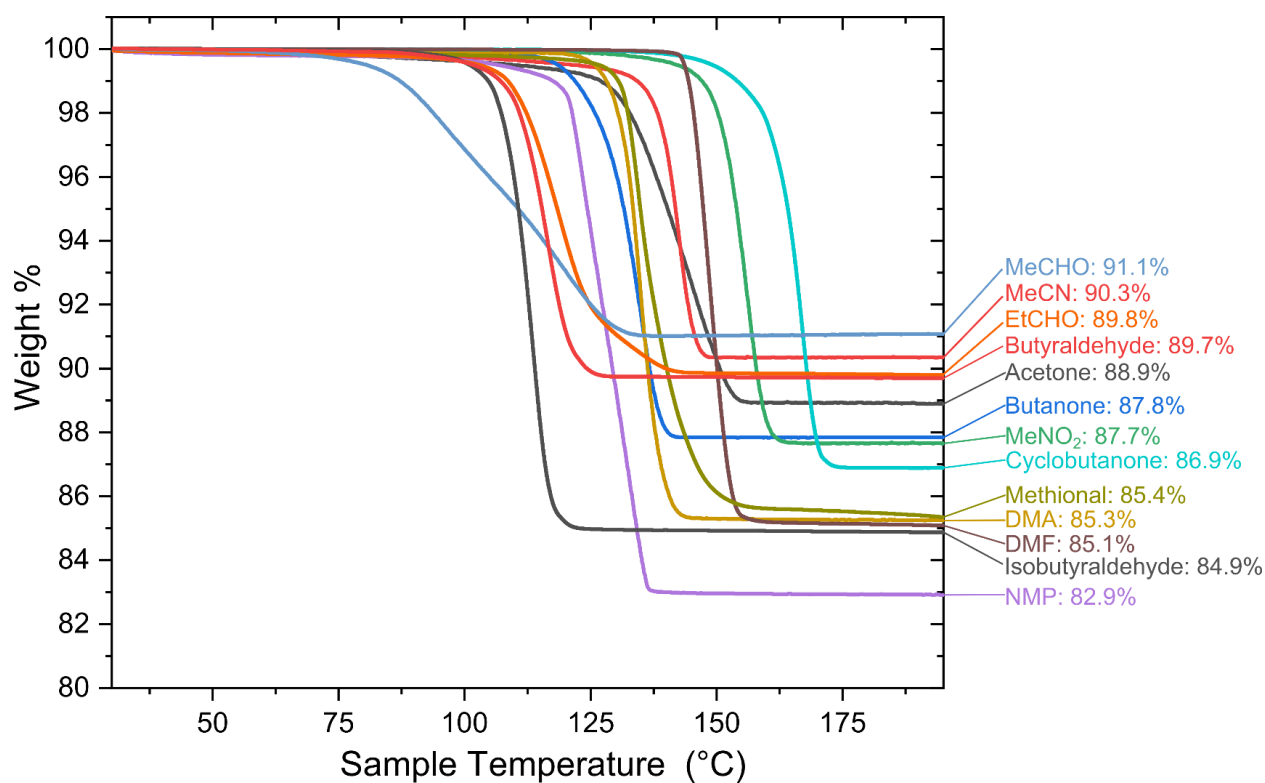


Figure 2.3: For most **1•guest** materials, thermogravimetric analysis (TGA) of the powdered samples in an atmosphere of nitrogen reveals a mass loss at temperatures between 75 °C and 175 °C, which is interpreted as to the loss of **guest** molecules from the cage. Guest loadings can be calculated from this loss of mass, as shown in table A.7.1. of Appendix A. TGA thermograms for materials which do not release the guest molecules in one clean step are also included in Appendix A.

A set of aldehydes and a cyclic ketone were selected as reactive guest molecules for this purpose. (Fig. 2.1f) The salt **1** could be recrystallized directly from cyclobutanone and 3-methylthiopropionaldehyde (methional) by slow cooling to yield colorless crystals isostructural to **1•MeCN**, as confirmed by their PXRD patterns and, in the case of cyclobutanone, scXRD structure. The other reactive guest molecules dissolved **1** negligibly so, for these guests, the

inclusion compounds were obtained by soaking **1** in an excess of the pure liquid guest, overnight. Soaking produced microcrystalline materials whose PXRD patterns indicated isostructurality to **1**•MeCN. Single crystals of the **1**•reactive guest materials containing acetaldehyde and propionaldehyde were obtained by crystallization from a mixture of the reactive guest and a solvent which dissolves **1** but does not enter the cage, nitrobenzene and diethylpropionamide, respectively. For butyraldehyde and isobutyraldehyde, placing a small amount of **1** in a large excess of the liquid guest overnight yielded single crystals suitable for scXRD analysis. Crystal structures could not be obtained for **1**•methional and for **1**•butyraldehyde, but the PXRD patterns of their microcrystalline powders indicate isostructurality to the other XB cages.

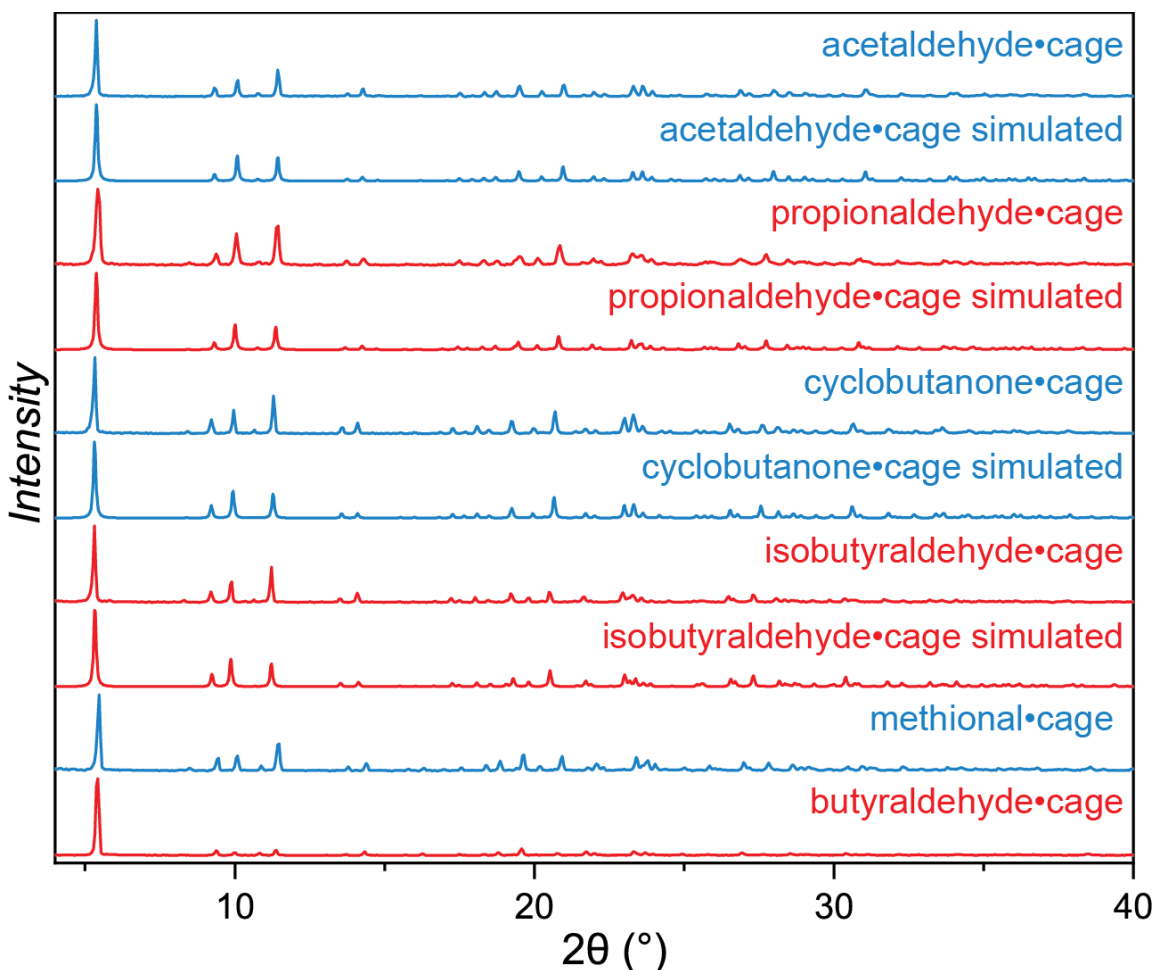


Figure 2.4: PXRD patterns of **1**•reactive guest materials compared to the patterns simulated from scXRD structures, when available.

An alternative method of loading **1** with a reactive guest to form **1**•reactive guest is ball-milling. In a typical experiment, 100 mg of **1** and 100 μ l of the guest were milled for between 5 and 30

minutes in a 15 mL zirconia milling jar, with one 3.2 g zirconia milling ball, leading to the formation of the **1**•reactive guest XB cage as identified by PXRD. Importantly, milling **1** on its own did not lead to the formation of a cage-type phase, instead causing the amorphization of **1** evidenced by the disappearance of well-defined peaks in the PXRD diffractogram. (Appendix A)

All six **1**•reactive guest materials were analyzed by ¹H NMR and TGA which indicated between four and seven guests per cage. Small molecules like acetaldehyde fill the cage in higher quantities and produce materials with closer to seven guests per cage, while larger guests fill the cage in lower numbers, as low as four per cage. Crucially, ¹H NMR spectra for all **1**•reactive guest materials showed the presence of only **1** and the guest molecular species, confirming that the host and guest are stable when in contact and that there is no reactivity between the host and reactive guest in the XB cage.

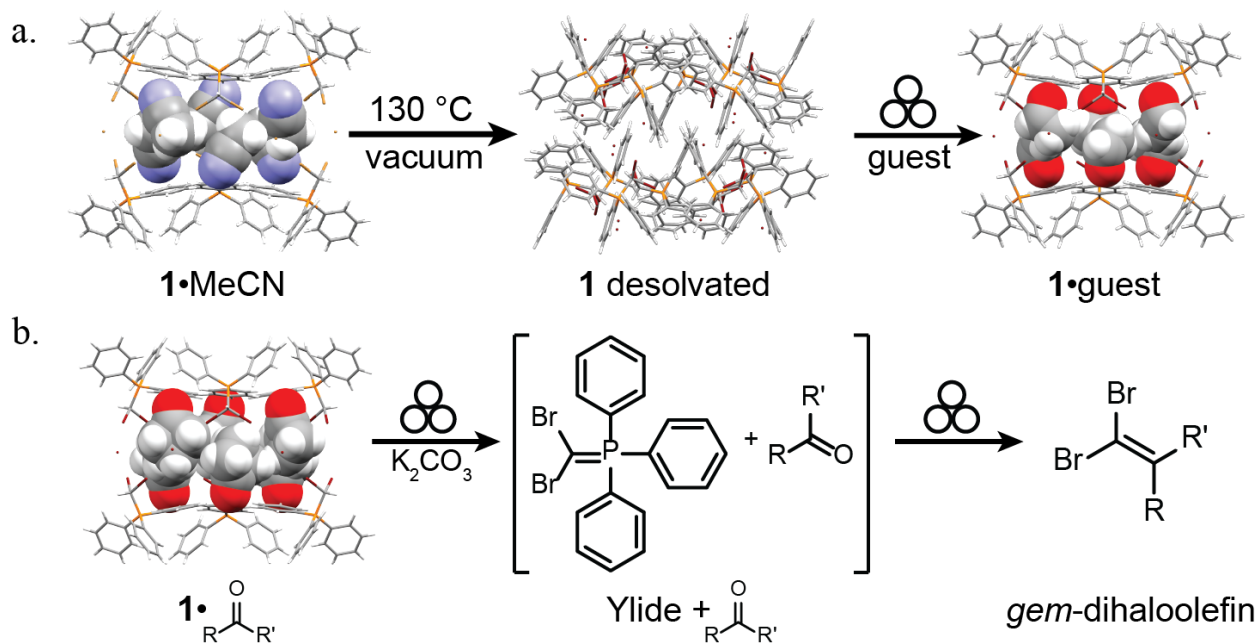


Figure 2.5: Transformations of **1.** a) **1**•MeCN can be desolvated to form **1** by exposure to vacuum at 130 °C, and **1** can be solvated by milling with, soaking in, or recrystallization from a guest. b) The **1**•reactive guest materials can be milled with K_2CO_3 to induce a Wittig reaction.

To explore the reactive potential of the **1**•reactive guest materials, 90 mg of each material was milled with 1.1 equivalents of K_2CO_3 for 30 minutes in a zirconia milling jar with a single 3.2 g zirconia milling ball. Immediate ¹H NMR analysis of the product showed the complete or near-

complete absence of **1** and the presence of triphenylphosphine oxide, consistent with a Wittig Olefination reaction.¹⁴ The NMR signals of the reactive guests were either significantly reduced or completely absent, replaced by those of the 1,1-dibromoalkene products expected from a Wittig olefination reaction using **1**. (Spectra included in Appendix A) Conversions were determined by comparison of ¹H NMR signal integrations for the reactive guest with those of the 1,1-dibromoalkene product. (Table 2.1) Conversions were generally high (> 90%) for the aldehyde-based reactions but were lower for cyclobutanone. In the case of isobutyraldehyde, the reaction produces a mixture of products for which analysis has, so far, been difficult.

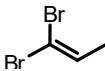
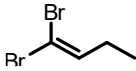
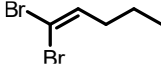
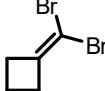
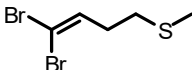
Product	Time (min)	Conversion
	30	98 %
	30	94 %
	30	99%
	60	68 %
	30	99 %

Table 2.1: ¹H NMR conversions for the mechanochemical Wittig reactions between **1** and its **reactive guest**. In all cases, 1.1 equivalents of K₂CO₃ were used as the base. See Appendix section A.9.2. for details of conversion calculations.

The so-far described **1**•**reactive guest** materials represent a rare case where a supramolecular host has encapsulated a molecular species which it is capable of derivatizing. The robustness of the supramolecular cage motif, evident by its persistence when encapsulating a wide array of small polar molecules, presents the opportunity to include any sufficiently small and polar substrate molecule in a predictable, stable, and stoichiometrically-suitable fashion for on-demand derivatization. For volatile liquid carbonyl-containing substrates like acetaldehyde, propionaldehyde, and cyclobutanone, this arrangement also provides the additional benefit of

mitigating issues related to the storage and measurement of these liquids. Whereas small-molecule aldehydes and ketones are volatile, with boiling points between 20° C and 100° C, their associated **1•reactive guest** forms are stable to much greater temperatures, as shown by their TGA thermograms. (Figure 2.6) Additionally, the formation of the **1•reactive guest** materials by crystallization, soaking, or milling acts as a means by which to automatically select a stoichiometrically-appropriate quantity of substrate.

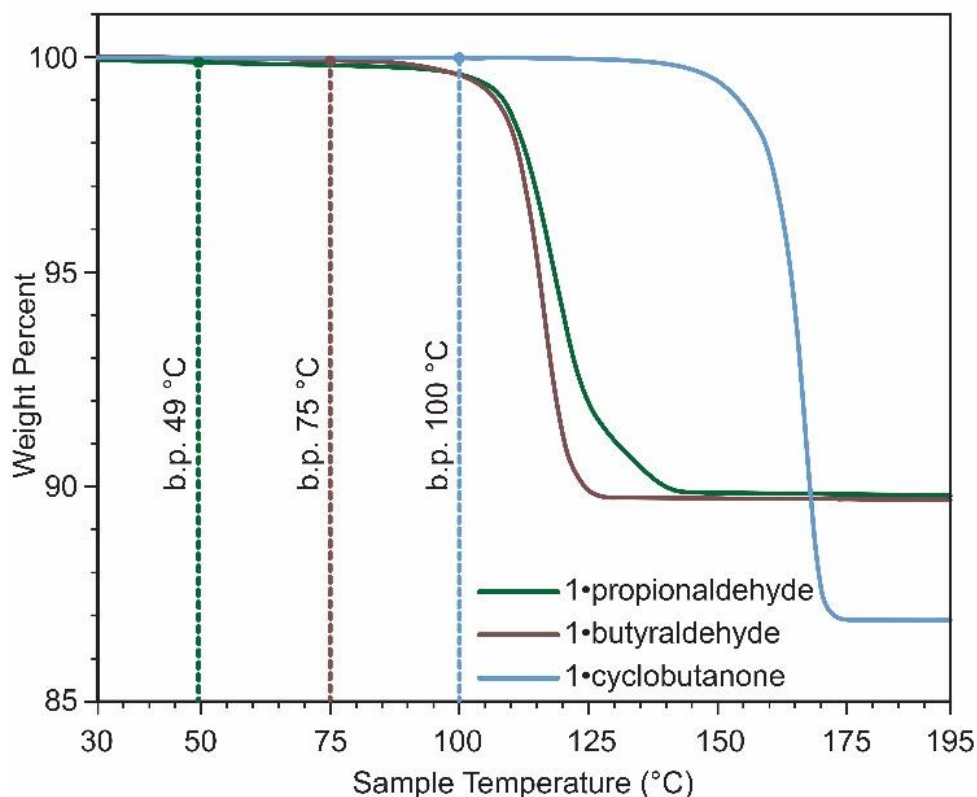


Figure 2.6: Encapsulation of some aldehydes mitigates their volatility. **1•reactive guest** materials containing propionaldehyde, butyraldehyde, and cyclobutanone stabilize these guests to temperatures beyond even their boiling points.

Based on the reliability and simplicity of the olefination reactions of **1** with its guests, we hypothesized that the **1•reactive guest** materials could act as supramolecular surrogates for their Wittig reaction products in the context of further chemical derivatization. This arrangement would allow for the replacement of volatile, reactive *gem*-dihaloolefins with their precursor **1•reactive guest** assemblies for use in subsequent reactions. To validate this possibility, we focused on the palladium-catalyzed Sonogashira cross-coupling of alkynes with vinyl halides.¹⁵ (Figure 2.7) Milling **1•butyraldehyde** with 2 equivalents of anhydrous K₂CO₃ and 2.2 equivalents of

(trimethylsilyl)acetylene in the presence of 10 mol % of PdCl₂(dppf)₂ and 8 mol % of CuI for 30 minutes in a zirconia milling jar with one 3.2 g milling ball led to the one-pot conversion of butyraldehyde to a mixture of mono- and di-coupled Sonogashira products with a significant amount of the intermediate *gem*-dihaloolefin remaining. Optimization of the milling reaction by increasing the milling time, quantity of base, and quantity of (trimethylsilyl)acetylene allowed for the near-complete disappearance of the *gem*-dihaloolefin intermediate and yields of 52 % for the di-coupled (enediyne) and 22% for the mono-coupled (eneyne) Sonogashira products as determined by ¹H NMR spectroscopy. (Table 2.2) The enediyne Sonogashira product was isolated by column chromatography for the best performing reaction (number 6), giving an isolated yield of 45 %, in good agreement with the 52 % determined by ¹H NMR. Interestingly, it was found that the sesquihydrate of K₂CO₃ generally performed better than the anhydrate as a base in milling experiments. Attempts to perform this one-pot Sonogashira reaction using K₂CO₃ as a base in solution have, in all cases, produced uniformly lower conversions to the Sonogashira products than did the optimized milling protocol, highlighting the efficiency and simplicity which is enabled by this solid-state one-pot methodology. (Appendix A)

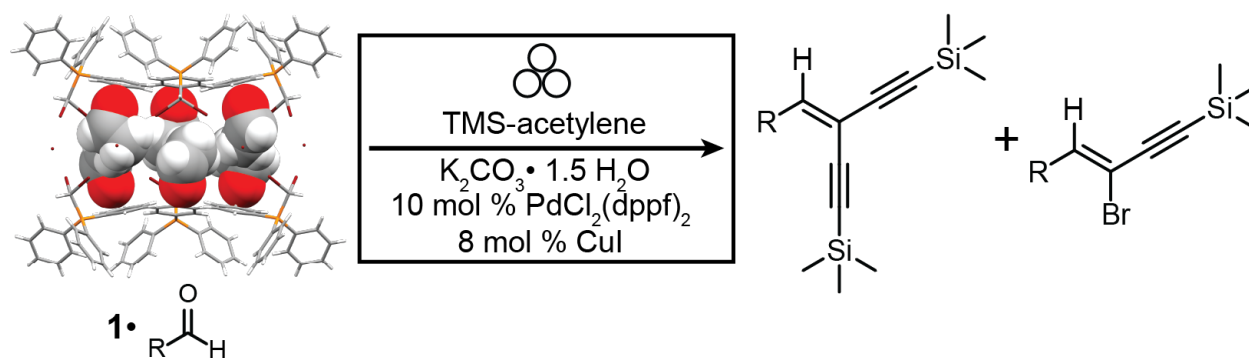


Figure 2.7: **1**•butyraldehyde reacts mechanochemically as part of a one-pot reaction involving olefination followed by Sonogashira coupling to produce a mixture of eneyne and dienyne products.

Next, we endeavored to expand the cage motif of **1**•guest to congeners containing chlorine and iodine instead of bromine. To this end, (dichloromethyl)triphenylphosphonium chloride, **2**, was synthesized according to a modified version of a procedure reported by Appel¹⁶ and was recrystallized from acetonitrile to yield single crystals suitable for scXRD analysis. We report that, instead of a cage-type structure, **2** adopts a dense-packed non-solvated form where R-Cl⋯Cl⁻ interactions are absent, outcompeted by R-H⋯Cl⁻ hydrogen-bonding interactions. All attempts to crystallize **2** as the cage form have been unsuccessful. The apparent inaccessibility of the cage

structure for **2** is rationalized by the weak σ -hole character of the XB donors when compared to those for the more polarizable bromine and iodine.

Reaction number	K ₂ CO ₃ (equivalents)	TMS-Acetylene (equivalents)	Time (min)	1,1-dibromoolefin	Eneyne	Eneidyne
1	2 (anhydrous)	2.2	30	17 %	17 %	17%
2	2	2.2	30	9 %	17 %	22%
3	2.5	2.2	30	9 %	35 %	39%
4	2.5	3.3	30	9%	43 %	22%
5	2.5	3.3	90	trace	22%	52% <i>isolated: 45 %</i>
6	2.5	3.3	180	trace	4%	40%

Table 2.2: Optimization of reaction conditions for the one-pot conversion of encapsulated aldehydes to eneyne and enedyne Sonogashira products. Conversions determined by ¹H NMR (see Appendix A, section A.9.3.) All K₂CO₃ was used in its sesquihydrate form, except as noted in reaction number 1.

Iodine, being even more polarizable than bromine, often engages in halogen bonding with even greater propensity. Indeed, heating iodoform with one equivalent of triphenylphosphine to reflux in acetonitrile gave primarily (diiodomethyl)triphenylphosphonium iodide, **3**, as a yellow solid whose PXRD pattern suggested a structure similar the cage form of **1•MeCN**. (Appendix A) Dissolution in nitromethane followed by rapid crystallization under high vacuum yielded crystals which were suitable for scXRD and revealed an XB cage isostructural to those formed by **1**. (Fig. 2.8) However, **3** has proven particularly prone to decomposition to form (iodomethyl)triphenylphosphonium iodide, **4**, whose structure we also report here. (Fig. 2.9) Crystallizations of **3** involving heating have resulted in the total decomposition of **3** to **4**, making completely impossible the use of heat-based recrystallizations to purify **3**, or to grow single crystals of it. Additionally, **3** has not yet been synthesized in bulk without significant amounts of an unidentified crystalline impurity visible in the PXRD. Work is ongoing to explore inclusion compounds and reactivity associated with **3**.

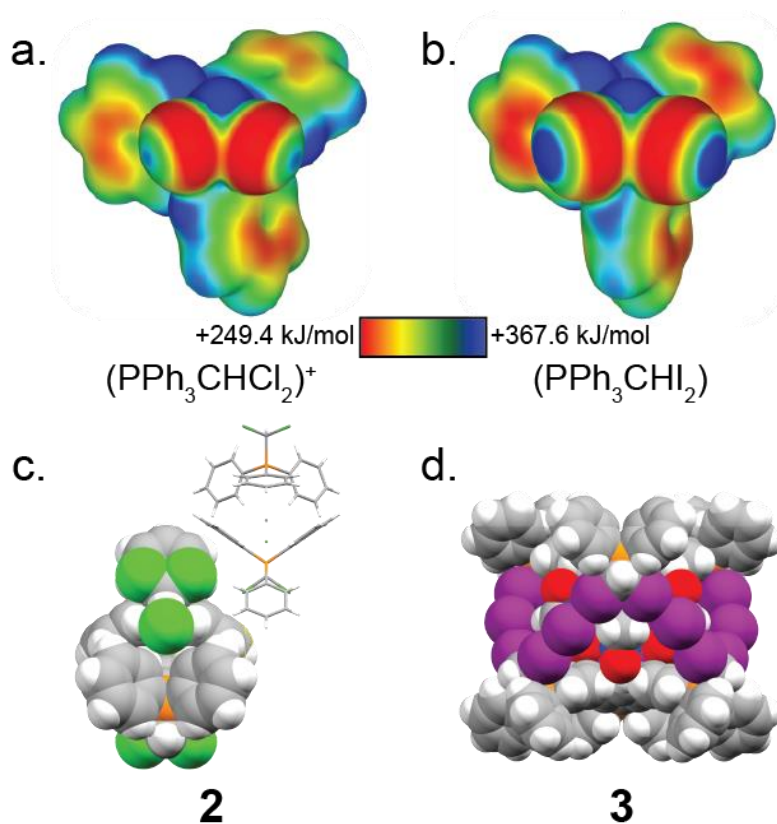


Figure 2.8: Overview of structures of 2 and 3. a) Electrostatic surface potential of the (dichloromethyl)triphenylphosphonium cation, **2**, plotted at an 0.0025 a.u. isosurface level. b) Electrostatic surface potential of the (diiodo)triphenylphosphonium cation, **3**, plotted at an 0.0025 a.u. isosurface level. c) Crystal structure of **2**, with one formula unit displayed as a space-fill model, and one formula unit displayed as capped sticks. d) Crystal structure of **4**, which adopts the XB cage structure with nitromethane as the guest.

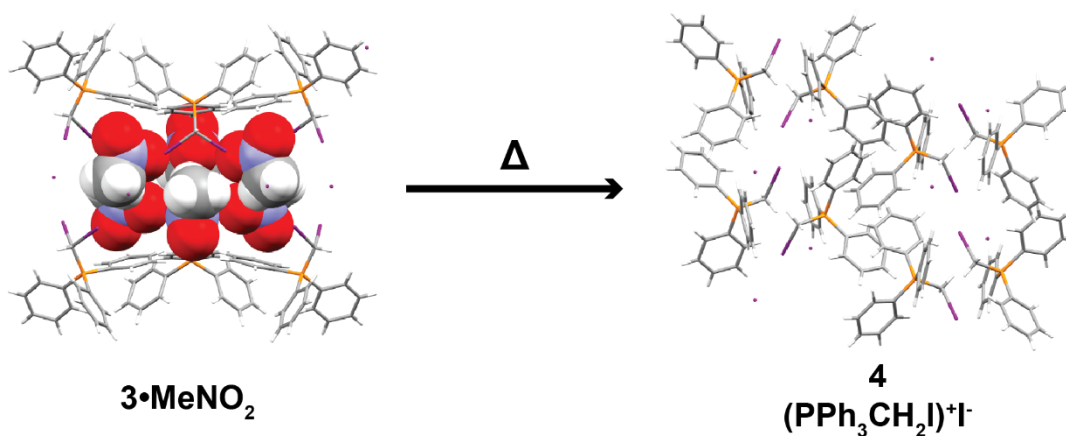


Figure 2.9: The salt **3** converts to its monoiodinated analogue, **4**, when dissolved in solvent and heated, or left to crystallize in open air for extended periods of time.

2.4 Conclusion

The work presented herein represents a proof-of-principle that a supramolecular host can encapsulate molecular species which are susceptible to specific and controlled chemical transformation by the host itself. This strategy of pre-assembled substrate encapsulated by reagent in a near-ideal stoichiometric ratio is a rarely-explored strategy for organic reactivity which allows for the rapid “on-demand” derivatization of a substrate by grinding with base and provides the additional benefits of sequestering volatile liquids substrates into a solid form. Work is ongoing to expand this methodology to additional carbonyl-containing substrates, and to develop additional one-pot synthetic methodologies which take advantage of these ability of these host-guest assemblies to act as surrogates for their reaction products for further derivatization.

References

1. a) L. R. MacGillivray, G. S. Papaefstathiou, T. Friščić, T. D. Hamilton, D. K. Bučar, Q. Chu, D. B. Varshney, and I. G. Georgiev, *Acc. Chem. Res.* **2008**, *41*, 280-291; b) L. R. MacGillivray, G. S. Papaefstathiou, in *Encyclopedia of Supramolecular Chemistry: Solid-State Chemistry/Topochemistry* (eds. J. L. Atwood and J. W. Steed), Marcel Dekker Inc., New York, **2004**, pp.1316-1321.
2. a) M. Yoshizawa, Y. Takeyama, T. Kusukawa, M. Fujita, *Angew. Chem. Int. Ed.* **2002**, *41*, 1347-1349; b) K. Tanaka, E. Mochizuki, N. Yasui, Y. Kai, I. Miyahara, K. Hirotsu, F. Toda, *Tetrahedron* **2000**, *56*, 6853-6865; c) J. N. Moorthy, K. Venkatesan, R. G. Weiss, *J. Org. Chem.* **1992**, *57*, 3292-3297.
3. a) C. J. Otoloski, A. M. Raj, G. Sharma, R. Prabhakar, V. Ramamurthy, C. G. Elles, *J. Phys. Chem. A* **2019**, *123*, 5061-5071; b) T. Iwasawa, E. Mann, J. Rebek, *J. Am. Chem. Soc.* **2006**, *128*, 9308-9309; c) M. Canton, A. B. Grommet, L. Pesce, J. Gemen, S. Li, Y. Diskin-Posner, A. Credi, G. M. Pavan, J. Andréasson, R. Klajn, *J. Am. Chem. Soc.* **2020**, *142*, 14557-14565.
4. a) A. Natarajan, L. S. Kaanumalle, S. Jockusch, C. L. D. Gibb, B. C. Gibb, N. J. Turro, V. Ramamurthy, *J. Am. Chem. Soc.* **2007**, *129*, 4132-4133; b) M. Yoshizawa, S. Miyagi, K. Ishiguro, M. Fujita, *J. Am. Chem. Soc.* **2004**, *126*, 9172-9173.
5. a) C. L. D. Gibb, A. K. Sundaresan, V. Ramamurthy, B. C. Gibb, *J. Am. Chem. Soc.* **2008**, *130*, 4069-4080; b) L. S. Kaanumalle, C. L. D. Gibb, B. C. Gibb, V. Ramamurthy, *J. Am. Chem. Soc.* **2004**, *126*, 14366-14367.
6. a) J. Kang, J. Rebek, *Nature* **1997**, *385*, 50-52; b) J. Kang, G. Hilmersson, J. Santamaría, J. Rebek, *J. Am. Chem. Soc.* **1998**, *120*, 3650-3656; c) J. H. Kim, S. V. Lindeman, J. K. Kochi, *J. Am. Chem. Soc.* **2001**, *123*, 4951-4959.
7. D. J. Cram, M. E. Tanner, R. Thomas, *Angew. Chem. Int. Ed. Engl.* **1991**, *30*, 1024-1027.
8. M. Yoshizawa, J. K. Klosterman, M. Fujita, *Angew. Chem. Int. Ed.* **2009**, *48*, 3418-3438;

9. W. Morris, C. J. Doonan, H. Furukawa, R. Banerjee, O. M. Yaghi, *J. Am. Chem. Soc.* **2008**, *130*, 12626-12627.
10. a) N. B. Desai, N. McKelvie, F. Ramirez, *J. Am. Chem. Soc.* **1962**, *84*, 1745-1747. b) A. J. Speziale, K. W. Ratt, *J. Am. Chem. Soc.* **1962**, *84*, 854-859; c) P. Michel, D. Gennet, A. Rassat, *Tetrahedron Lett.* **1999**, *40*, 8575-8578.
11. a) G. Chelucci, *Chem. Rev.* **2012**, *112*, 1344-1462; b) J. Uenishi, K. Matsui, *Tetrahedron Lett.* **2001**, *42*, 4353-4355; c) J. Uenishi, K. Matsui, H. Ohmiya, *J. Organomet. Chem.* **2002**, *653*, 141-149; d) W. Ye, J. Mo, T. Zhao, B. Xu, *Chem. Commun.* **2009**, 3246-3248; e) K. Jouvin, A. Coste, A. Bayle, F. Legrand, G. Karthikeyan, K. Tadiparthi, G. Evano, *Organometallics* **2012**, *31*, 7933-7947.
12. P. Wolkoff, *Can. J. Chem* **1975**, *53*, 1333-1335.
13. a) C. B. Aakeröy, A. Rajbanshi, P. Metrangolo, G. Resnati, M. F. Parisi, J. Desper, T. Pilati, *CrystEngComm* **2012**, *14*, 6366-6368; b) N. K. Beyeh, F. Pan, K. Rissanen, *Angew. Chem. Int. Ed.* **2015**, *54*, 7303-7307; c) O. Dumele, B. S. Schreib, U. Warzok, N. Trapp, C. A. Schalley, F. Diederich, *Angew. Chem. Int. Ed.* **2017**, *56*, 1152-1157; d) C. J. Massena, N. B. Wageling, D. A. Decato, E. M. Rodriguez, A. M. Rose, O. M. Berryman, *Angew. Chem. Int. Ed.* **2016**, *55*, 12398-12402; e) L. Turunen, A. Peuronen, S. Forsblom, E. Kalenius, M. Lahtinen, K. Rissanen, *Eur. J. Chem.* **2017**, *23*, 11714-11718.
14. a) V. P. Balema, J. W. Wiench, M. Pruski, V. K. Pecharsky, *J. Am. Chem. Soc.* **2002**, *124*, 6244-6245; b) F. Toda, H. Akai, *J. Org. Chem.* **1990**, *55*, 3447-3450.
15. a) D. A. Fulmer, W. C. Shearouse, S. T. Medonza, J. Mack, *Green Chem.* **2009**, *11*, 1821-1825; b) L. Chen, D. Leslie, M. G. Coleman, J. Mack, *Chem. Sci.* **2018**, *9*, 4650-4661; c) R. Thorwirth, A. Stolle, B. Ondruschka, *Green Chem.* **2010**, *12*, 985-991.
16. R. Appel, W. Morbach, *Synthesis* **1977**, *10*, 699-700.

Connecting text for Chapter 3

Chapter 3 explores copper-based zeolitic imidazolate frameworks (ZIFs) which have, surprisingly, been scarcely reported in the literature. Crystal structure predictions (CSP) have been performed by collaborators in the groups of Prof. Mihails Arhangel'skis and Prof. Andrew J. Morris to reveal that ZIFs based on copper(II) nodes and 2-methyl-2-vinyl- and 2-ethynylimidazolate linkers adopt high-density non-porous phases. These phases were subsequently obtained experimentally in our laboratory. Moreover, the unsaturated chemical functionalities of the vinyl- and ethynyl-based materials confer hypergolicity, the property of ignition on contact with an oxidizer, to these materials. Hypergolicity is an important property for fuels and fuel additives in the aerospace industry.

In keeping with the theme of this Thesis, these materials have properties which are a result of the combined influence of their chemical identities, which induce hypergolicity, and their crystal structures, which contribute to their high energy densities.

Chapter 3: *Ab Initio* metal-organic framework crystal structure prediction reveals elusive copper(II) imidazolate frameworks

This work corresponds to a manuscript currently in preparation for submission, co-authored by Yizhi Xu, Dr. Hatem M. Titi, Dr. James P. Darby, Prof. Robin D. Rogers, Prof. Andrew J. Morris, Prof. Mihails Arhangel'skis, and Prof. Tomislav Frišćić.

3.1 Abstract

We report the first *ab initio* crystal structure prediction for a set of divalent copper-based zeolitic imidazolate frameworks (ZIFs), a type of metal-organic framework (MOF), revealing the existence of elusive copper ZIFs based on 2-substituted imidazolate linkers. Framework materials consisting of divalent copper nodes and 2-methylimidazole, 2-vinylimidazole, and 2-ethynylimidazole linkers are computationally predicted and each found to adopt dense, nonporous frameworks. Experimental efforts confirm the predictions, and each material is synthesized from solution as both single crystals and microcrystalline powders. The vinyl- and ethynyl-functionalized ZIFs are found to be hypergolic, that is they ignite on contact with an oxidizer, and their predicted combustion energies are significantly higher than previously reported hypergolic MOFs and ZIFs.

3.2 Introduction

Metal-organic frameworks (MOFs) have become one of the most popular classes of functional solid materials due to their modularity, diversity, and suitability for an increasingly wide set of applications. To date, MOFs have been designed for purposes including gas sorption,¹ gas separation,² sensing,³ drug delivery,⁴ aerospace propulsion,^{5,6} catalysis,^{7,8} and more.⁹ However, MOF design remains an exercise of trial and error, where a combination of an organic linker and a metallic node often adopt crystal structures which cannot be foreseen by intuition or the principles of reticular chemistry¹⁰ alone.¹¹ Given the central function which crystal structure plays in the function of MOF materials, the lack of reliable and universal crystal structure prediction (CSP) methodologies for them represents a serious gap in the toolset which researchers have to design stable and functional MOFs with predictable solid-state structures. This is in stark contrast

to the fields of purely inorganic and purely organic molecular materials, where CSP has been demonstrated as a highly versatile method of materials design.^{12,13}

Recently, computational approaches for MOF CSP based on density functional theory (DFT) have been reported by our team. While these methods have accurately predicted the existence of already reported MOF structures¹⁴ and have also been used to propose putative structures for experimentally unexplored systems,¹⁵ no examples of *ab initio* CSP-guided MOF discovery have been yet reported. In this work, we present the first example of the use of CSP to predict MOF structures which are subsequently found to exist experimentally. Specifically, we show the accurate prediction of phases for the system of divalent copper nodes and 2-methylimidazolate (**HMeIm**), 2-vinylimidazole (**HVIm**) and 2-ethynylimidazole (**HAIm**) imidazolate linkers, leading to the synthesis of hypergolic ZIF materials, those which ignite upon contact with an oxidizer and are of great use in the aerospace propulsion industry, with greater energy density than previously reported hypergolic ZIFs.⁵

Zeolitic imidazolate frameworks (ZIFs) are a subset of MOFs which are based on divalent metal nodes and imidazolate organic linkers, and are one of the most widely-studied classes of MOFs.¹⁶ Due to the 145° metal-ligand-metal bonding geometry of the imidazolate linker, ZIF materials often adopt structures and topologies which mimic natural zeolites.¹⁷ While ZIFs based on zinc,¹⁸ cobalt,¹⁹ and cadmium²⁰ are common in the literature, those based on copper are surprisingly few, with only a set of materials based on divalent copper nodes and unsubstituted imidazolate linkers reported.^{21,22,23} Given the great attention paid to metal imidazolates in the literature and the increasing list of elements which have been used as nodes for ZIF-type materials, we were curious to investigate why copper had not been used more extensively for this purpose. We selected the system involving divalent copper nodes and **HVIm** linkers as our first target of MOF CSP, as we reported previously that this ligand is capable of inducing hypergolicity in ZIFs when used as a linker.

3.3. Results and discussion

We performed CSP for the putative Cu(**VIm**)₂ framework using a combination of the *ab initio* random structure searching (AIRSS) algorithm²⁴ and the Wyckoff alignment of molecules (WAM) algorithm¹⁴ taking isolated Cu atoms and isolated **VIm** linkers in 1:2 stoichiometric ratio, and introducing them at random positions within a unit cell of arbitrary dimensions. Thousands of such

structures were generated for combinations comprising one, two, three, and four ZIF formula units per primitive unit cell, and these randomly-generated structures were energy-minimized using PBE functional combined with Grimme D2 dispersion correction. (see Appendix B for details).

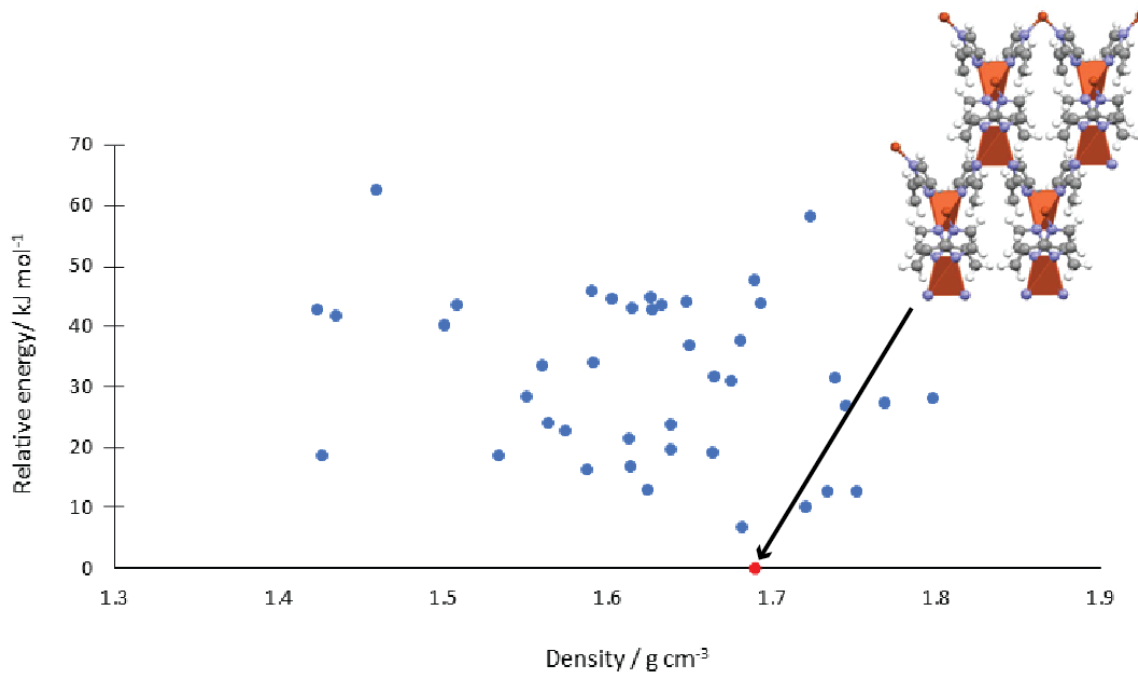


Figure 3.1: Generated structures for the putative $\text{Cu}(\text{VIm})_2$ framework, plotted based on their relative energies and densities. The structure with the lowest energy, marked in red, is a nonporous *diamondoid*-topology framework.

Calculations were performed in the plane-wave DFT code CASTEP. The optimized structures were ranked in the order of increasing energies, duplicate pairs were merged, and the unique low energy structures were reoptimized using a more accurate energy model based on the PBE functional and many-body dispersion (MBD*) correction scheme.²⁵ The energies of the final set of structures were plotted against their densities, revealing the general trend of increasing stability with increased density (Figure 3.1). The structure with calculated global energy minimum was found to be a dense, nonporous structure with a diamondoid (*dia*) topology. This result presented the possibility that higher-energy hypergolic materials may be accessible for this system due to the dense nature of the predicted crystal structure. Encouraged by the initial result for $\text{Cu}(\text{VIm})_2$, we performed the CSP of the $\text{Cu}(\text{MeIm})_2$ and $\text{Cu}(\text{AIm})_2$ systems. Gratifyingly, as in the case for $\text{Cu}(\text{VIm})_2$, initial predictions for these materials have revealed dense structures of *dia* topology as

the global energy minima, once again suggesting that these Cu-based ZIFs could have superior energy densities to porous ZIFs.

Based on the results of these CSP calculations, we decided to evaluate energy densities of the predicted MOFs by calculating their enthalpies of combustion. Energy density is a metric of special importance in the field of energetic materials and aerospace propulsion where it is one of the most important factors governing the feasibility of a fuel for wide-spread use. Recent combustion calorimetric analysis of MOF combustion has revealed that MOFs, especially the nitrogen-rich ZIFs, possess energy densities which are on par with traditional fuels and energetic materials like gasoline, TNT, and hydrazine, and are tunable based on the chemical identities of the linker and node, but also on the structure the MOF adopts in the solid-state.²⁶ Unsurprisingly, the open and porous nature of many MOFs is a limiting factor for their energy density, and all previously reported hypergolic MOFs adopt porous structures to the detriment of their energy density. In the case of the materials described herein, the volumetric energy densities (E_v) were calculated using CASTEP DFT code to be 39.5 kJ cm^{-3} , 45.1 kJ cm^{-3} and 43.8 kJ cm^{-3} for Cu(**MeIm**)₂, Cu(**VIm**)₂ and Cu(**AIm**)₂, respectively, calculated for their reaction with O₂ to form solid CuO and N₂, CO₂, and H₂O gas. These energy densities all twice exceed those of the most energy-dense previously reported Co-, Zn- and Cd-based hypergolic MOFs. While this is mostly a result of the increased density of the copper-based materials, their molar and gravimetric energy densities are also uniformly higher than the previously reported ZIFs.⁵

ZIF	$\Delta E_c / \text{kJ mol}^{-1}$	$E_g / \text{kJ g}^{-1}$	$E_v / \text{kJ cm}^{-3}$
Cu(AIm) ₂	-7004.146	-28.530	-43.754
Cu(MeIm) ₂	-6058.846	-27.109	-39.478
Cu(VIm) ₂	-7036.912	-28.204	-45.103

Table 3.1. Calculated combustion energies (ΔE_c), gravimetric energy densities (E_g) and volumetric energy densities (E_v) as calculated by CASTEP DFT code for Cu(**MeIm**)₂, Cu(**VIm**)₂, and Cu(**AIm**)₂.

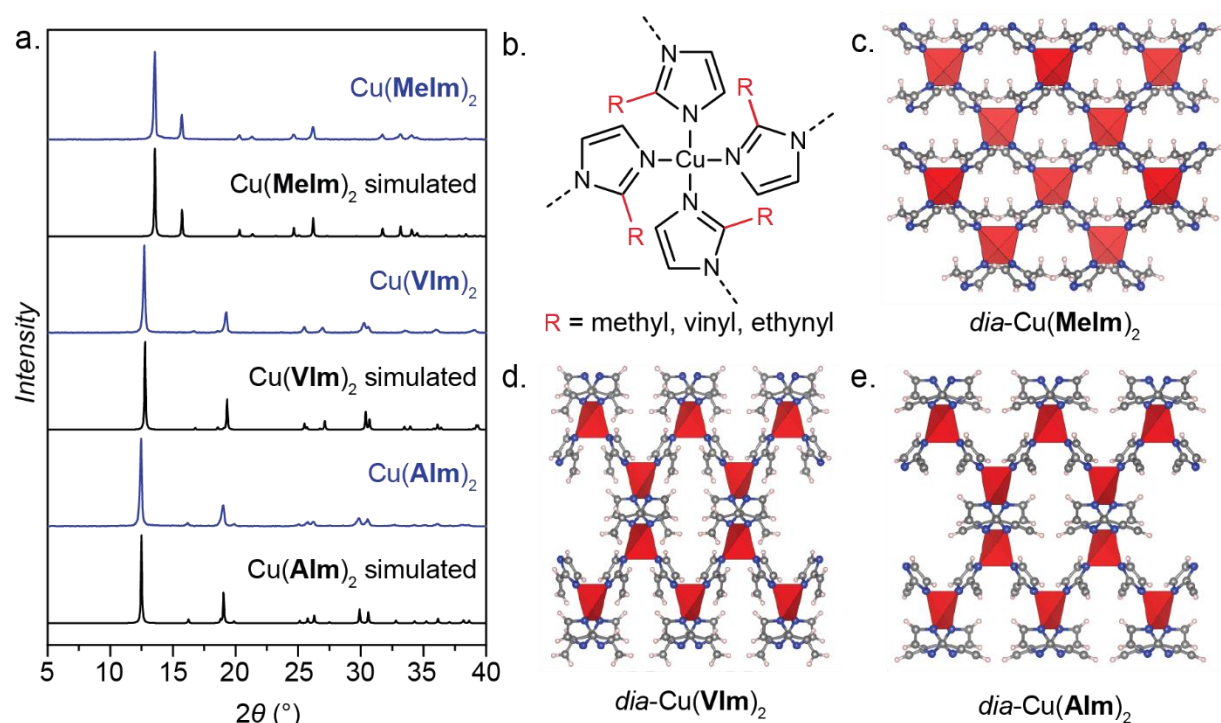


Figure 3.2. Experimental analysis and structures of $\text{Cu}(\text{MeIm})_2$, $\text{Cu}(\text{VIm})_2$, and $\text{Cu}(\text{AIm})_2$. a) PXRD patterns for bulk microcrystalline ZIFs in comparison with the simulated patterns for their crystal structures as determined by scXRD. b) Chemical scheme for the ZIFs reported herein. c) Crystal structure of $\text{Cu}(\text{MeIm})_2$. d) Crystal structure of $\text{Cu}(\text{VIm})_2$. e) Crystal structure of $\text{Cu}(\text{AIm})_2$.

Encouraged by the apparently stability of dense, closely packed copper(II) imidazolate framework materials based on **MeIm**, **VIm**, and **AIm** linkers as revealed by CSP, as well as their promising predicted energetic properties, we endeavored to synthesize these materials in the laboratory. In all three cases, adding the ligand to a solution of copper(II) sulfate in dilute aqueous ammonia led to the precipitation of a large amount of brown powder which was collected and examined under an optical microscope, revealing small (20 μm) green (with **MeIm**), blue (with **VIm**) or purple (with **AIm**) single crystals dispersed infrequently among it (Synthesis details included in Appendix B). These crystals were separated by hand and analyzed by single crystal X-ray diffraction (scXRD). Gratifyingly, the structures obtained by scXRD analysis of $\text{Cu}(\text{VIm})_2$ matched those predicted by our CSP method, and all three copper imidazolate structures, $\text{Cu}(\text{MeIm})_2$, $\text{Cu}(\text{VIm})_2$, $\text{Cu}(\text{AIm})_2$, adopt *dia*-topology crystal structures with $\text{Cu}(\text{VIm})_2$ and $\text{Cu}(\text{AIm})_2$ showing isostructurality to each other.

Phase-pure microcrystalline powders of *dia*-Cu(**MeIm**)₂ and *dia*-Cu(**AIm**)₂ could be obtained by modification of the solution methods used for the synthesis of their single-crystalline materials. However, no suitable conditions were found for the precipitation of phase-pure *dia*-Cu(**VIm**)₂ from solution. Instead, solid [Cu(NH₃)₄]SO₄·H₂O, solid **HVIm**, and a small amount of water were subject to resonant acoustic mixing²⁷ (RAM) for 20 minutes to afford the phase-pure product. For all three materials, powder X-ray diffraction (PXRD) confirmed the presence of reflections which match to the structures determined by scXRD, and each material showed no unidentified crystalline impurities. Thermogravimetric analysis (TGA) under a stream of air confirmed the purity of each material by measuring the loss of mass associated with the thermal decomposition of the ZIF to CuOe, allowed for the calculation of the metal content for each sample. Additionally, impact testing revealed that these materials were stable to 50 J impacts with no obvious signs of detonation. However, the burgundy-colored Cu(**VIm**)₂ material turned dark green after impact, and new X-ray reflections appeared in the PXRD pattern of the material after this testing.

Generally, during the synthesis and handling of *dia*-Cu(**AIm**)₂ it was apparent that rough handling, *i.e.* scraping with a spatula on the side of a vial, would induce a color change of the material from purple to dark green. This color change was always accompanied by the appearance of new, unidentified reflections in the PXRD pattern of the material. A phase-pure sample of this green form (β -phase) was obtained by ball-milling 60 mg of *dia*-Cu(**AIm**)₂ (α -phase) with 30 μ l of methanol for 20 minutes at 25 Hz in a 15 mL zirconia milling jar containing a single 3.2 g zirconia milling ball. After stirring the milled powder briefly in methanol and drying *in vacuo*, the purity of the material was confirmed by PXRD, where no reflections corresponding to the α -phase remained. TGA confirmed that the metal content of the material was unchanged. The possibility of chemical transformation of the linkers of the ZIF during milling was excluded by proton nuclear magnetic resonance (¹H NMR) analysis of the β -phase ZIF digested in dilute DCl, which showed identical signals to that of the α -phase.

The crystal structure of the β -phase was determined from PXRD data and was found to be a distorted and lower-symmetry version of the α -phase, but of identical *dia*-topology (Appendix section B.12). While the structure of the α -phase contains one crystallographically-unique imidazolate unit, the β -phases has four such symmetry-independent units. In addition, the structure

of the β -phase has two independent copper atoms, one of which has essentially square-planar coordination geometry, while the α -phase has only one crystallographically-unique copper atom.

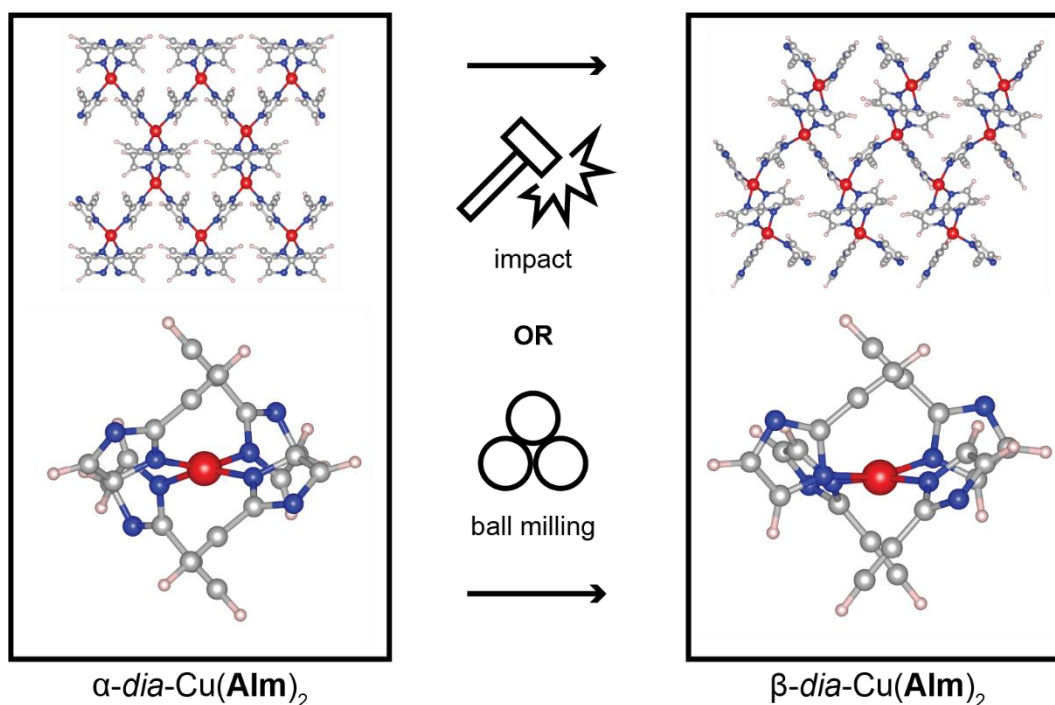


Figure 3.3. Crystal structures of α -Cu(AIm)₂ and β -Cu(AIm)₂. The α -phase converts to the β -phase upon impact or ball-milling.

Previous work in our group⁵ demonstrated the possibility of inducing hypergolicity in otherwise non-hypergolic ZIFs by functionalizing the imidazolate linkers with vinyl- (VIm) and ethynyl-based (AIm) hypergolic “trigger” moieties, producing materials with ultrafast ignition delays (IDs), the time which elapses between the contact of a material with an oxidizer and the beginning of ignition. We subjected samples of *dia*-Cu(VIm)₂, α -*dia*-Cu(AIm)₂, and β -*dia*-Cu(AIm)₂ materials to a standardized hypergolicity drop-test²⁸ where one 10 μ l drop of white fuming nitric acid (WFNA, 98% HNO₃) is released from a glass syringe 5.0 cm above a 5 mg pile of microcrystalline ZIF material in a glass vial. The first contact of the WFNA drop with the ZIF powder is captured by a high-speed video camera operating at 1000 frames/s. The time which elapses between this first contact and the first observation of ignition is considered the ID. Generally, lower IDs are considered desirable for aerospace applications, with 50 ms being the upper limit for a useful hypergolic material.²⁹ Hypergolic testing of Cu(VIm)₂, α -Cu(AIm)₂, and

β -Cu(**AIM**)₂ revealed reliable and high-performance hypergolic behavior for each material. The vinyl-functionalized material Cu(**VIM**)₂ showed an average ignition delay of 40(6) ms, producing sparks which persisted for over 200 ms. The acetylene-functionalized materials α -Cu(**AIM**)₂, and β -Cu(**AIM**)₂ showed even higher performance, producing bright flames with average ignition delays of 14(4) ms and 15(3) ms, respectively, indicating that their difference in crystal structure plays a minor role in the modulation of their energetic properties. While the IDs for Cu(**VIM**)₂, α -Cu(**AIM**)₂, and β -Cu(**AIM**)₂ are somewhat higher than their previously reported porous zinc and cobalt counterparts using the same organic ligands, they still fall well below the threshold of 50 ms, indicating adequate hypergolicity for most application. Unsurprisingly, Cu(**MeIM**)₂ shows no hypergolic behavior due to its lack of hypergolic trigger moiety.



Figure 3.4 Hypergolic testing results for the Cu(**VIM**)₂, α -Cu(**AIM**)₂, and β -Cu(**AIM**)₂ MOFs.

3.4 Conclusion

The results detailed herein represent the first example of *ab initio* CSP for the guided discovery of metal-organic frameworks. The prediction that dense, nonporous phases exist for the system of divalent copper nodes and functionalized imidazolate linkers informed the synthesis of these materials in the laboratory, ultimately yielding high performance hypergolic materials with energy densities over twice as great as previously reported ZIFs. Without the aid of *ab initio* CSP, that dense phases exist for these divalent copper systems would have been unknown, and the search for such high-energy-density systems would have been an effort of trial and error. We hope this

work will provide a basis for researchers to screen certain node and linker combinations to discover the crystalline phases which they may adopt when combined to form MOF materials.

References

1. M. Eddaoudi, H. Li, O. M. Yaghi, *J. Am. Chem. Soc.* **2000**, *122*, 1391-1397.
2. H. Bux, C. Chmelik, R. Krishna, J. Carp, *J. Membr. Sci.* **2011**, *369*, 284-289.
3. Y. Cui, R. Song, J. Yu, Y. Min, Z. Wang, C. Wu, Y. Yang, Z. Wang, B. Chen, G. Q. Qian, *Adv. Mater.* **2015**, *27*, 1420-1425.
4. S. R. Miller, D. Heurtaux, T. Baati, P. Horcajada, J. Grenèche, C. Serre, *Chem. Commun.* **2010**, *46*, 4526-4528.
5. H. M. Titi, J. M. Marrett, G. Dayaker, M. Arhangelskis, C. Mottillo, A. J. Morris, G. P. Rachiero, T. Friščić, R. D. Rogers, *Sci. Adv.* **2019**, *5*, eaav9044.
6. Y. Xu, Y. Wang, Y. Zhong, G. Lei, Z. Li, J. Zhang, T. Zhang, *Inorg. Chem.* **2021**, *60*, 5100-5106.
7. T. Wang, L. Gao, J. Hou, S. J. A. Herou, J. T. Griffiths, W. Li, J. Dong, S. Gao, M. Titirici, R. V. Kumar, A. K. Cheetham, X. Bao, Q. Fu, S. K. Smoukov, *Nat. Commun.* **2019**, *10*, 1340.
8. I. Luz, F. X. Llabrés i Xamena, A. Corma, *J. Catal.* **2010**, *276*, 134-140.
9. Y. Liu, A. J. Howarth, J. T. Hupp, O. K. Farha, *Angew. Chem. Int. Ed.* **2015**, *54*, 9001-9005.
10. O. M. Yaghi, *J. Am. Chem. Soc.* **2016**, *138*, 15507-15509.
11. A. D. Katsenis, A. Puškarić, V. Štrukil, C. Mottillo, P. A. Julien, K. Užarević, M. Pham, T. Do, S. A. J. Kimber, P. Lazić, O. Magdysyuk, R. E. Dinnebier, I. Halasz, T. Friščić, *Nat. Commun.* **2015**, *6*, 6662.
12. M. Woodley, R. Catlow, *Nat. Mater.* **2008**, *7*, 937-946.
13. R. L. Greenaway, V. Santolini, A. Pulido, M. A. Little, B. M. Alston, M. E. Briggs, G. M. Day, A. I. Cooper, K. E. Jelfs, *Angew. Chem. Int. Ed.* **2019**, *58*, 16281-16281.
14. J. P. Darby, M. Arhangelskis, A. D. Katsensis, J. M. Marrett, T. Friščić, A. J. Morris, *Chem. Mater.* **2020**, *32*, 5835-5844.
15. M. Arhangelskis, A. D. Katsenis, A. J. Morris, T. Friščić, *Chem. Sci.* **2018**, *9*, 3367-3375.
16. K. S. Park, Z. Ni, A. P. Côté, J. Y. Choi, R. Huang, F. J. Uribe-Romo, H. K. Chae, M. O'Keeffe, O. M. Yaghi, *Proc. Natl. Acad. Sci. U.S.A.* **2006**, *103*, 10186-10191.
17. A. Phan, C. J. Doonan, F. J. Uribe-Romo, C. B. Knobler, M. O'Keeffe, O. M. Yaghi, *Acc. Chem. Res.* **2010**, *43*, 58-67.
18. A. Zhu, R. Lin, Z. Qui, U. Liu, Y. Lin, J. Zhang, X. Chen, *Microporous Mesoporous Mater.* **2012**, *157*, 43-49.
19. R. Banerjee, A. Phan, B. Wang, C. Knobler, H. Furukawa, M. O'Keeffe, O. M. Yaghi, *Science* **2008**, *319*, 939-943.
20. C. A. O'Keeffe, C. Mottillo, J. Vainauskas, L. Fábrián, T. Friščić, R. W. Schurko, *Chem. Mater.* **2020**, *32*, 4273-4281.
21. G. P. Brown, S. Aftergut, *J. Polym. Sci.* **1964**, *A2*, 1839-1845.
22. M. Inoue, M. Kishita, M. Kubo, *Inorg. Chem.* **1965**, *4*, 626-628.
23. N. Masciocchi, S. Bruni, E. Cariati, F. Cariati, S. Galli, A. Sironi, *Inorg. Chem.* **2001**, *40*, 5897-5905.
24. C. J. Pickard, R. J. Needs, *J. Phys. Condens. Matter* **2011**, *23*, 053201.

25. M. Arhangel'skoi's, A. D. Katsenis, N. Novendra, Z. Akimbekov, D. Gandrath, J. M. Marrett, G. Ayoub, A. J. Morris, O. K. Farha, T. Frišćić, A. Navrostky, *Chem. Mater.* **2019**, *31*, 3777-3783.
26. H. M. Titi, M. Arhangel'skis, A. D. Katsenis, C. Mottillo, G. Ayoub, J. L. Do, A. M. Fidelli, R. D. Rogers, T. Frišćić, *Chem, Mater.* **2019**, *31*, 4882-4888.
27. H. M. Titi, J. L. Do, A. J. Howarth, K. Nagapudi, T. Frišćić, *Chem. Sci.* **2020**, *11*, 7578-7584.
28. G. P. Rachiero, H. M. Titi, R. D. Rogers, *Chem. Commun.* **2017**, *53*, 7736-7739.
29. S. Li, H. Gao, J. M. Shreeve, *Angew. Chem. Int. Ed.* **2014**, *126*, 3013-3016.

Chapter 4: Conclusions and outlook

The two experimental Chapters in this Thesis present crystalline materials whose functions lie at the intersection of their chemical identities and their solid-state structural features. The inclusion compounds detailed in Chapter 2 can encapsulate a range of molecular guests due to the robust halogen-bonding motif which allows for the reliable formation of isostructural cages in the solid-state. The reactivity between the host and the guest, on the other hand, is a function of their chemical identities which are complimentary for the Wittig olefination reaction upon exposure to base. The hypergolic copper-based ZIFs presented in Chapter 3 have high energy densities as a result of their dense crystal structures, setting them apart from the previously reported, porous hypergolic materials. However, their reactivity with white fuming nitric acid, *i.e.* hypergolicity, is principally a result of the unsaturated chemical functionalities installed on the framework linkers.

The concept of pairing a given chemical functionality or reactivity with a certain crystal structure is not a new one, with one of the most relevant examples being the pharmaceutical industry's quest to crystallize biologically-active molecules in structures which are, for example, not prone to polymorphic conversion or are amenable to tableting. Other examples include the design of ZIFs for post-synthetic modification, detailed in Chapter 1, or the crystal engineering which resulted in any of the [2+2] photodimerizations detailed in the same Chapter. This Thesis presents two new examples of crystal engineering for the creation of functional materials. In the case of the halogen-bonded cages, the discovery of a supramolecular host which is a precursor to the reagent responsible for the Wittig olefination enabled us to study a so-far unexplored approach to solid state reactivity, where a host can derivatize a guest but be stored as a stable solid in advance.

The crystal structure prediction of metal imidazolates to reveal dense-phase copper ZIFs represents a fundamentally new approach for the discovery of MOF materials. Computational evaluation indicated that the use of an alternative metal node, copper(II), instead of the more common zinc, cobalt, or cadmium ones enabled the synthesis of high-energy-density hypergolic materials for potentially useful propulsion applications. In this work, the consideration of framework density allowed for materials to be synthesized which match previously reported materials in hypergolic performance but outdo them considerably in the very important metric of energy content.

It is our hope that both contributions detailed in Chapters 2 and 3 will provide a foundation for exciting new approaches to design functional solid materials. The synthetic approach detailed in Chapter 2, involving the formation of reactive solid-state supramolecular assemblies, could be expanded to include a wide range of reactive guests, including ketones and aldehydes which were not used herein. However, this strategy could be used, more generally, to inform the design of reactive host-guest materials with other types of organic reactivity. While this will require clever molecular design and crystal engineering, I hope that approaches for the reliable design of such materials could be developed, providing easy access to reactive host guest materials for any given organic transformation. Ultimately, these types of materials could serve to simplify the mechanochemical synthesis of organic materials by providing solid, easily-stored materials for on-demand reaction.

The CSP methodology presented in Chapter 3 should provide a roadmap for future endeavors to interrogate the phase landscape of MOFs. The structure of MOFs is central to their function, and this computational methodology should be useful in the design of porous and otherwise functional MOFs which do not lose their function as a result of polymorphic conversion to more stable forms. For example, we see the opportunity to discover porous MOF materials whose structures are also the most stable in their phase landscape, providing porous materials which could, potentially, be more stable in real-world application involving molecular absorption or separation. This work also provides a synthetic precedent for the synthesis of 2-substituted copper(II) imidazolate frameworks, a class of materials which has been conspicuously absent from the literature. The expansion of this set of materials using other 2-substituted imidazolate linkers is likely to lead to the discovery of materials with interesting properties and structures, as has been the case with zinc-, cobalt-, and cadmium- frameworks based on this type of linkers.

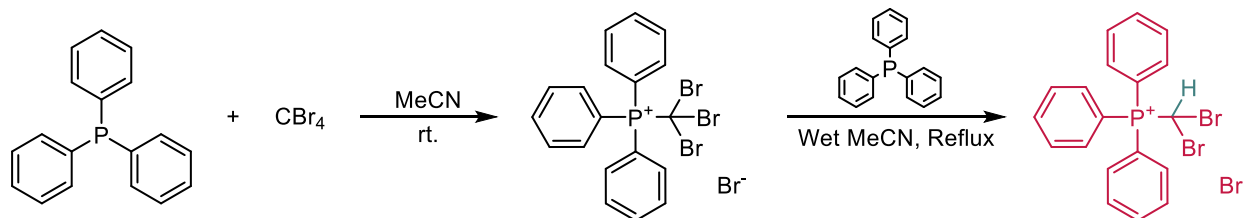
Appendix A: A hexameric halogen-bonded phosphonium salt cage for encapsulation and solid-state transformation of small-molecule carbonyl compounds

A.1. Materials

Carbon tetrabromide (99%), acetaldehyde ($\geq 99\%$), acrylic acid (99%), dimethylacetamide (DMA) ($\geq 99\%$), nitromethane (MeNO_2) ($\geq 95\%$), N-methyl-2-pyrrolidone (NMP) (99%), nitrobenzene (99%), iodoform (99%), benzene (anhydrous, 99.8%), carbon tetrachloride (99.9%) and copper(I) iodide ($\geq 99.5\%$) were obtained from Sigma Aldrich. Triphenylphosphine (99%), cyclohex-2-enone (98%), propionaldehyde (97%), isobutyraldehyde (99%), butyraldehyde (96%), 3-(methylthio)propionaldehyde (methional) (97%), cyclobutanone ($\geq 98\%$), diethyl propionamide ($\geq 95\%$), (trimethylsilyl)acetylene (98%) and 1,1'-bis(diphenylphosphino)ferrocene-palladium(II) dichloride dichloromethane complex (98%) were obtained from Oakwood Chemical. Dimethyl sulfoxide (DMSO) (99.9%), dimethyl formamide (DMF) (99.8%), acetic acid (99.5%), and potassium carbonate (99%) were obtained from ACP Chemicals. Butanone (99.9%), and acetone (99.5%) were obtained from Fischer chemical. All chemicals were used without purification, except benzene which was stored over molecular sieves and subject to three cycles of freeze-pump-thaw degassing under argon before use in solution experiments.

A.2. Synthetic Methods

A.2.1. Synthesis of (dibromomethyl)triphenylphosphonium bromide (1)



Scheme A.1 Reaction scheme for the synthesis of **1**.

The salt **1** was synthesized according to a procedure previously reported by Wolkoff.¹ The general scheme for this reaction is shown above. The product of synthesis is microcrystalline **1•MeCN** which can be recrystallized carefully from acetonitrile to yield single crystal suitable for single crystal X-ray diffraction analysis (scXRD). Yield for step 1 is 84 %. Yield for step 2 is 44%.

A.2.2. Desolvation of 1•MeCN to form desolvated 1

Microcrystalline **1•MeCN** was exposed to 130 °C under high vacuum for 14 hours to yield desolvated **1**. Recrystallization of this powder by slow cooling from nitrobenzene produces single crystals suitable for scXRD analysis which reveal the structure of desolvated **1**.

A.2.3. Procedure for synthesis of 1•guest materials

Materials of the type **1•guest** were formed by recrystallization of **1** from hot liquid guest followed by collection by filtration. In the case of **1** grown from non-volatile liquids (NMP, DMF, DMA, acetic acid, acrylic acid, DMSO, cyclohexanone, cyclohex-2-enone), the solid product is rinsed with benzene during the filtration step before drying on the frit for 5 minutes. In the case of cyclohexanone and cyclohex-2-enone, precipitation of the cage material is particularly slow (~48 hrs) and was carried out in the freezer (-18 °C). In the cases where single crystal structures were collected, suitable crystals were collected from the mother liquor by pipette before filtration.

A.2.4. Procedure for the synthesis of reactive 1•guest materials

Bulk powders of the **1•reactive guest** materials used in all milling experiments were obtained by soaking 200 mg (0.39 mmol) of **1** in 1 mL of the liquid guest for 24 hours followed by filtration and washing with benzene. Single crystals of **1•acetaldehyde** were grown by recrystallization of **1** from a hot mixture of 50 v/v% acetaldehyde in nitrobenzene. Single crystals of **1•propionaldehyde** are grown in the same fashion from a 50 v/v% mixture of propionaldehyde in N,N-diethylpropionamide. Single crystals of **1•butyraldehyde** and **1•isobutyraldehyde** were obtained by adding a very small amount (~5 mg) of **1** to a large excess (1 mL) of liquid aldehyde and letting the powder soak for 24 hours to yield single crystals. X-ray quality single crystals **1•cyclobutanone** could be obtained by simple recrystallization of **1** from the hot liquid cyclobutanone.

A.2.5. Procedure for the synthesis of reactive 1•guests by milling

Bulk powders of the **1•reactive guest** materials can also be obtained by ball-milling **1** with the guest liquid. 100 mg (0.19 mmol) of **1** and 100 μL of the liquid guest are added to a 15 mL zirconia milling jar with a single zirconia ball of 3.2 g mass. The mixture is milled for 5 to 30 minutes (see PXRD data for specific times) at 30 Hz using a FormTech Scientific FTS-1000 shaker mill.

A.2.6. General Procedure for the Mechanochemical Wittig Olefination via 1•guest

90 mg of **1•reactive guest** and 1.1 equivalents of K_2CO_3 (between 22.1 mg and 24.5 mg depending on the guest loading, as shown in table A.7.1.) are added to a 15 mL zirconia milling jar with a single 3.2 g zirconia ball, and the mixture is milled for 30 minutes at 25 Hz. Analysis proceeds immediately by ^1H NMR spectroscopy in CDCl_3 and conversion is determined by the comparison of integrations of characteristic peaks of the starting materials and product. The *gem*-dibromoolefin product is purified either by distillation or column chromatography; specifics for each sample are listed in section A.8.

A.2.7. Procedure for the One-Pot Wittig/Sonogashira Derivatization via 1•guest

In a typical experiment, 90 mg of **1•reactive guest** material is added to a 15 mL zirconia milling jar with one 3.2 g zirconia ball. 10 mol % $\text{PdCl}_2(\text{dppf})\cdot\text{CH}_2\text{Cl}_2$, 8 mol % CuI , potassium carbonate, and (trimethylsilyl)acetylene are added and the mixture is milled at 30 Hz. The required mass of catalyst was calculated based on the quantity of butyraldehyde assuming a loading of 5 molecules per cage. The temperature of the reaction mixtures immediately after milling were measured using an infrared thermometer and were found to never exceed 29 $^\circ\text{C}$. Chemical analysis proceeds immediately by ^1H NMR spectroscopy in CDCl_3 . Purification of the product(s) proceeds by column chromatography of the jar contents; specifics for each product are listed in section A.8.

A.2.9. Procedure for the One-Pot Wittig/Sonogashira Derivatization Attempts in Solution

For each experiment, 90 mg of **1•butyraldehyde**, 2 mL of anhydrous benzene degassed by three cycles of freeze-pump-thaw under argon, base, PdCl₂(**dppf**) (10 mol %), CuI (8 mol %), and (trimethylsilyl)acetylene were added to a sealed, oven-dried vial and stirred under argon for the listed time. Reactions using diisopropylethylamine mimic conditions used by Uenishi *et al.* for the coupling of terminal acetylenes with 1,1-dibromoolefins.² Workup for all reactions involved the removal of solvent *in vacuo* before ¹H NMR analysis of the crude product mixtures. Yields were determined by ¹H NMR as explained in section A.9.3.

Table A.2.1. Conditions and conversions for solution-based one-pot Wittig/Sonogashira derivatizations

Base	Solvent	Reaction time	Reaction temperature	Wittig product	Sonogashira products
2.5 eq. K ₂ CO ₃	Benzene	90 min	RT	Yes	No
2.5 eq. K ₂ CO ₃ sesquihydrate	Benzene	90 min	RT	Yes	No
2.5 eq. K ₂ CO ₃	Benzene	24 hours	RT	Yes	No
2.5 eq. K ₂ CO ₃ sesquihydrate	Benzene	24 hours	RT	No	Mono: 17% Di: 8%
2.5 eq. K ₂ CO ₃	Benzene	90 min	40 °C	Yes	No
2.5 eq. K ₂ CO ₃ sesquihydrate	Benzene	90 min	40 °C	Yes	No
2.5 eq. K ₂ CO ₃	Benzene	24 hours	40 °C	Yes	No
2.5 eq. K ₂ CO ₃ sesquihydrate	Benzene	24 hours	40 °C	No	Mono: < 5% Di: 14%
4 eq. <i>i</i> -Pr ₂ NH See Ref. 2	Benzene	90 min	RT	Yes	No
4 eq. <i>i</i> -Pr ₂ NH See Ref. 2	Benzene	90 min	40 °C	Yes	No
4 eq. <i>i</i> -Pr ₂ NH See Ref. 2	Benzene	24 hours	RT	Yes	Mono: 9% Di: none
4 eq. <i>i</i> -Pr ₂ NH See Ref. 2	Benzene	24 hours	40 °C	Yes	Mono: 7% Di: none

A.2.10. Procedure for the synthesis of (dichloromethyl)triphenylphosphonium chloride (2)

The salt **2** was synthesized according to a modified procedure reported by Appel *et al.*,³ scaled down 100-fold. 2 mL (20.7 mmol) of carbon tetrachloride and 524 mg (2 mmol) of triphenylphosphine were added to a mixture of 4.2 mL benzene and 0.8 mL acetonitrile. The

mixture was heated to 50 °C in a sealed vial with rapid stirring. After 5 minutes, the mixture turned a pale yellow, and the vial was opened to the air with continued stirring. After 10 minutes, a white precipitate formed which was isolated by filtration and washed with a minimal amount of benzene. The yield was 55%. Crystals for scXRD structural analysis were obtained by slow evaporation of a solution of this material in acetonitrile.

A.2.11. Procedure for the synthesis of (diiodomethyl)triphenylphosphonium iodide (3) and (iodomethyl)triphenylphosphonium iodide (4)

1.18 g (3 mmol) of iodoform and 787 mg (3 mmol) of triphenylphosphine were added to 5 ml of acetonitrile and dissolved fully by sonication. The mixture was refluxed for 5 minutes, until a deep red paste formed on the walls of the vessel. This paste was broken up by hand with a glass rod and by submersion of the sealed vessel in a sonicating bath, converting it to a yellow powder in the process. This powder was collected by filtration was suspended in 10 mL of acetonitrile and again collected by filtration before drying briefly on the frit. After collection, the product was stored under an inert atmosphere. Single crystals of **3**•MeNO₂ were grown by evaporation of a solution of this powder in nitromethane under high vacuum over the course of approximately 20 minutes. Longer evaporations and those involving heat produced single crystals of the species (iodomethyl)triphenylphosphonium iodide, **4**, whose crystal structure we also report here.

A.3. Electrostatic surface potential (ESP) calculations

Electrostatic surface potential maps were calculated for the cations of salts **1**, **2**, and **3**, based on their structures after geometry optimization using Gaussian 16⁴ at the B3LYP/cc-pVTZ level of theory.⁵ The basis set aug-cc-pVTZ was used for the iodine atoms of **3**, and was sourced from the basis set exchange.⁶ ESPs were visualized in Vesta.⁷

A.4. Instrumental Methods

A.4.1. Nuclear magnetic resonance spectroscopy (NMR)

Solution ¹H and ¹³C nuclear magnetic resonance spectra were collected using either a Varian Inova 500 MHz spectrometer operating at 500 MHz for ¹H nuclei and 125 MHz for ¹³C nuclei or a Varian

VNMR 500 MHz spectrometer operating at the same frequencies. Chemical shifts are reported relative to CDCl_3 ($\delta = 7.26$ ppm for ^1H ; $\delta = 77.16$ ppm for ^{13}C).

A.4.2. Mass spectrometry (MS)

GCMS data was obtained using a Bruker Scion single quadrupole GC/MS. APCI-MS data was obtained using a Bruker Maxis Impact API QqTOF spectrometer.

A.4.3. Thermogravimetric Analysis (TGA)

Thermogravimetric analysis was performed using a Mettler Toledo TGA/DSC 1 instrument. The samples (approximately 10 mg per measurement) were placed in 70 μL open-top alumina crucibles and measurements were conducted under a stream of nitrogen gas (50 ml min^{-1}) from room temperature to 200 $^\circ\text{C}$ at a rate of $10 \text{ }^\circ\text{C min}^{-1}$.

A.4.4. Powder x-ray diffraction (PXRD)

Powder X-ray diffraction data was collected using a Bruker D2 PHASER diffractometer which was outfitted with a LynxEye liner position-sensitive detector using nickel filtered $\text{CuK}\alpha$ X-ray radiation.

A.4.5. Single crystal structure determinations

Single crystal X-ray diffraction (SCXRD) data were measured on a Bruker D8 Venture diffractometer equipped with a Photon 200 area detector, and $I\mu\text{S}$ microfocus X-ray source (Bruker AXS, $\text{CuK}\alpha$ source). Measurements were carried out at 180(2) K for **1**, **1·MeNO₂**, **1·acetic acid**, and **1·acrylic acid**, and 153(2) K for **1·DMA**, while the rest were mounted at 298(2) K. Crystals were coated with a thin layer of paratone oil before mounting on the diffractometer. Structural solutions were carried out using the SHELXTL package.⁸ The parameters were refined for all data by full-matrix-least-squares refinement of F^2 using SHELXL.⁹ The structures **1·MeCN**, **1·acetone**, **1·2-butanone**, **1·acetic acid**, **1·DMSO**, **1·acetaldehyde**, and **1·cyclobutanone** exhibit disorders that were modeled successfully, however due to the large thermal motion apparent for **1·MeCN**, the guest molecules were modeled isotopically for this material. The crystal structure of **4** was found to be twinned by inversion. Crystalline compounds **1·MeCN**, **1·MeNO₂**, **1·acetone**, **1·acetic acid**, **1·acrylic acid**, **1·DMSO**, **1·NMP**, **1·DMF**, **1·isobutyraldehyde**, and **1·propionaldehyde** contain disordered guest molecules positioned on a 3-fold screw axis, and

therefore cannot be reliably modeled by discrete atoms. The electron density corresponding to these symmetry-disordered guests were subtracted using the SQUEEZE procedure, as included in the PLATON software package.¹⁰ All of the non-hydrogen atoms were refined with anisotropic thermal parameters. All hydrogen atoms were constrained to ride on their carrier atom.

Table A.4.1. Crystallographic data for scXRD crystal structures.

Compound	1	1·MeCN	1·MeNO ₂	1·acetone	1·2-butanone	1·acetic acid	1·acrylic acid	1·DMSO	1·NMP	1·DMF
Empirical formula	C ₁₉ H ₁₆ Br ₃ P	C ₂₁ H ₁₉ Br ₃ NP	C ₂₀ H ₁₉ Br ₃ NO ₂ P	C ₂₂ H ₂₂ Br ₃ OP	C ₂₃ H ₂₄ Br ₃ OP	C ₂₁ H ₂₀ Br ₃ O ₂ P	C ₂₂ H ₂₀ Br ₃ O ₂ P	C ₂₁ H ₂₂ Br ₃ OPS	C ₂₄ H ₂₅ Br ₃ NOP	C ₂₂ H ₂₃ Br ₃ NOP
<i>M_r</i>	515.02	556.07	576.06	573.09	587.12	575.07	587.08	593.14	614.15	588.11
<i>T/K</i>	180(2)	298(2)	180(2)	298(2)	298(2)	180(2)	180(2)	298(2)	298(2)	298(2)
Crystal system	monoclinic	trigonal	trigonal	trigonal	trigonal	trigonal	trigonal	trigonal	trigonal	trigonal
Space group	C2/c	<i>R</i> -3	<i>R</i> -3	<i>R</i> -3	<i>R</i> -3	<i>R</i> -3	<i>R</i> -3	<i>R</i> -3	<i>R</i> -3	<i>R</i> -3
<i>a/Å</i>	17.7546(4)	33.1499(5)	32.270(2)	33.0003(6)	33.4263(4)	32.4936(8)	32.283(2)	33.4643(5)	33.612(2)	33.1823(9)
<i>b/Å</i>	15.5320(3)	33.1499(5)	32.270(2)	33.0003(6)	33.4263(4)	32.4936(8)	32.283(2)	33.4643(5)	33.612(2)	33.1823(9)
<i>c/Å</i>	28.3321(6)	11.1629(2)	11.3230(8)	11.1350(2)	11.2099(2)	11.3322(8)	11.5522(8)	11.1613(2)	11.4292(7)	11.4506(3)
<i>α/°</i>	90	90	90	90	90	90	90	90	90	90
<i>β/°</i>	99.2280(10)	90	90	90	90	90	90	90	90	90
<i>γ/°</i>	90	120	120	120	120	120	120	120	120	120
<i>V/Å³</i>	7711.9(3)	10623.6(4)	10211.4(15)	10501.6(4)	10847.0(3)	10361.9(9)	10426.7(15)	10824.5(4)	11182.4(17)	10918.7(7)
<i>Z</i>	16	18	18	18	18	18	18	18	18	18
<i>ρ_{calc}/g cm⁻³</i>	1.774	1.565	1.686	1.631	1.618	1.659	1.683	1.638	1.642	1.610
<i>μ/mm⁻¹</i>	8.506	7.007	7.381	7.126	6.914	7.259	7.230	7.725	6.750	6.883
<i>F</i> (000)	4000.0	4896.0	5076.0	5076.0	5220.0	5076.0	5184.0	5256.0	5472.0	5220.0
2θ range for data collection/°	6.32 to 144.588	8.498 to 144.72	8.426 to 145.472	8.522 to 144.792	8.458 to 144.352	10.89 to 144.722	8.282 to 145.226	11.318 to 144.396	5.258 to 144.34	5.326 to 145.218
Index ranges	-21 ≤ <i>h</i> ≤ 20, -12 ≤ <i>k</i> ≤ 19, -34 ≤ <i>l</i> ≤ 34	-40 ≤ <i>h</i> ≤ 40, -40 ≤ <i>k</i> ≤ 40, -13 ≤ <i>l</i> ≤ 5	-39 ≤ <i>h</i> ≤ 39, -39 ≤ <i>k</i> ≤ 31, -11 ≤ <i>l</i> ≤ 14	-40 ≤ <i>h</i> ≤ 40, -40 ≤ <i>k</i> ≤ 40, -13 ≤ <i>l</i> ≤ 8	-31 ≤ <i>h</i> ≤ 41, -41 ≤ <i>k</i> ≤ 30, -8 ≤ <i>l</i> ≤ 13	-40 ≤ <i>h</i> ≤ 40, -40 ≤ <i>k</i> ≤ 40, -13 ≤ <i>l</i> ≤ 9	-28 ≤ <i>h</i> ≤ 39, -39 ≤ <i>k</i> ≤ 37, -14 ≤ <i>l</i> ≤ 11	-41 ≤ <i>h</i> ≤ 41, -40 ≤ <i>k</i> ≤ 41, -8 ≤ <i>l</i> ≤ 13	-41 ≤ <i>h</i> ≤ 41, -41 ≤ <i>k</i> ≤ 41, -14 ≤ <i>l</i> ≤ 11	-40 ≤ <i>h</i> ≤ 40, -40 ≤ <i>k</i> ≤ 40, -10 ≤ <i>l</i> ≤ 14
Reflections collected	67258	25997	17041	58815	20559	26076	20408	61014	76439	74379
Independent reflections	7620 [R _{int} = 0.0643, R _{sigma} = 0.0295]	4593 [R _{int} = 0.0364, R _{sigma} = 0.0284]	4416 [R _{int} = 0.0366, R _{sigma} = 0.0330]	4613 [R _{int} = 0.0416, R _{sigma} = 0.0167]	4617 [R _{int} = 0.0312, R _{sigma} = 0.0254]	4448 [R _{int} = 0.0306, R _{sigma} = 0.0226]	4593 [R _{int} = 0.0539, R _{sigma} = 0.0439]	4702 [R _{int} = 0.0371, R _{sigma} = 0.0183]	4907 [R _{int} = 0.0943, R _{sigma} = 0.0277]	4798 [R _{int} = 0.0540, R _{sigma} = 0.0203]
Data/restraints/parameters	7620/54/415	4593/42/230	4416/18/245	4613/253/263	4617/222/266	4448/280/275	4593/0/254	4702/309/263	4907/18/272	4798/338/255
<i>S</i>	1.029	1.064	1.042	1.083	1.077	1.041	1.054	1.065	1.086	1.056
Final R indexes [I ≥ 2σ(I)]	R ₁ = 0.0328, wR ₂ = 0.0806	R ₁ = 0.0372, wR ₂ = 0.0977	R ₁ = 0.0278, wR ₂ = 0.0647	R ₁ = 0.0291, wR ₂ = 0.0655	R ₁ = 0.0291, wR ₂ = 0.0700	R ₁ = 0.0336, wR ₂ = 0.0880	R ₁ = 0.0411, wR ₂ = 0.0957	R ₁ = 0.0393, wR ₂ = 0.1037	R ₁ = 0.0419, wR ₂ = 0.1021	R ₁ = 0.0445, wR ₂ = 0.1179
Final R indexes [all data]	R ₁ = 0.0433, wR ₂ = 0.0878	R ₁ = 0.0407, wR ₂ = 0.1014	R ₁ = 0.0308, wR ₂ = 0.0674	R ₁ = 0.0357, wR ₂ = 0.0711	R ₁ = 0.0317, wR ₂ = 0.0723	R ₁ = 0.0355, wR ₂ = 0.0898	R ₁ = 0.0457, wR ₂ = 0.0994	R ₁ = 0.0412, wR ₂ = 0.1059	R ₁ = 0.0741, wR ₂ = 0.1365	R ₁ = 0.0553, wR ₂ = 0.1319
Largest diff. peak/hole / e Å⁻³	0.69/-0.47	0.69/-0.54	0.47/-0.64	1.44/-0.44	0.41/-0.52	0.99/-0.66	2.95/-0.78	1.20/-0.81	0.39/-0.63	0.65/-0.66

Table A.4.2. Crystallographic data for scXRD crystal structures.

Compound	1-DMA	1-acetaldehyde	1-isobutyraldehyde	1-cyclobutanone	1-propionaldehyde	2	3	4
Empirical formula	C ₂₃ H ₂₅ Br ₃ NOP	C ₂₁ H ₂₀ Br ₃ OP	C ₂₂ H ₂₂ Br ₃ O _{0.75} P	C ₂₃ H ₂₂ Br ₃ OP	C ₄₂ H ₄₁ Br ₆ OP ₂	C ₁₉ H ₁₆ Cl ₃ P	C ₂₀ H ₁₉ I ₃ NO ₂ P	C ₁₉ H ₁₇ I ₂ P
<i>M_r</i>	602.14	559.07	569.09	585.10	1103.15	381.64	717.03	530.09
<i>T/K</i>	153(2)	298(2)	298(2)	298(2)	298(2)	298(2)	298(2)	298(2)
Crystal system	trigonal	trigonal	trigonal	trigonal	trigonal	orthorhombic	trigonal	orthorhombic
Space group	<i>R</i> -3	<i>R</i> -3	<i>R</i> -3	<i>R</i> -3	<i>R</i> -3	<i>Pnma</i>	<i>R</i> -3	<i>Pca</i> ₂₁
<i>a/Å</i>	33.0726(18)	32.8339(5)	33.1440(5)	33.2157(4)	32.8602(12)	12.2883(2)	32.9862(15)	14.8074(2)
<i>b/Å</i>	33.0726(18)	32.8339(5)	33.1440(5)	33.2157(4)	32.8602(12)	12.5399(2)	32.9862(15)	12.4892(2)
<i>c/Å</i>	11.3690(6)	11.1368(2)	11.4650(2)	11.3174(2)	11.2660(4)	12.1077(2)	12.0449(8)	20.5366(3)
<i>α</i> ^o	90	90	90	90	90	90	90	90
<i>β</i> ^o	90	90	90	90	90	90	90	90
<i>γ</i> ^o	120	120	120	120	120	90	120	90
<i>V/Å</i> ³	10769.3(13)	10397.7(4)	10907.2(4)	10813.4(3)	10535.1(9)	1865.72(5)	11350.1(13)	3797.89(10)
<i>Z</i>	18	18	18	18	9	4	18	8
<i>ρ_{calc}</i> / g cm ⁻³	1.671	1.607	1.560	1.617	1.565	1.359	1.888	1.854
<i>μ</i> / mm ⁻¹	6.993	7.182	6.849	6.936	7.062	5.214	29.905	26.752
<i>F</i> (000)	5364.0	4932.0	5040.0	5184.0	4869.0	784.0	6048.0	2016.0
2θ range for data collection ^o	8.368 to 144.926	9.33 to 144.818	10.676 to 144.874	9.222 to 144.97	9.322 to 144.686	10.156 to 144.696	5.358 to 144.13	7.078 to 144.93
Index ranges	-40 ≤ h ≤ 40, -40 ≤ k ≤ 40, -14 ≤ l ≤ 12	-40 ≤ h ≤ 40, -40 ≤ k ≤ 40, -13 ≤ l ≤ 13	-40 ≤ h ≤ 40, -40 ≤ k ≤ 40, -14 ≤ l ≤ 10	-41 ≤ h ≤ 40, -40 ≤ k ≤ 41, -13 ≤ l ≤ 13	-33 ≤ h ≤ 40, -40 ≤ k ≤ 40, -5 ≤ l ≤ 13	-15 ≤ h ≤ 15, -15 ≤ k ≤ 15, -14 ≤ l ≤ 14	-40 ≤ h ≤ 40, -39 ≤ k ≤ 40, -14 ≤ l ≤ 11	-16 ≤ h ≤ 18, -15 ≤ k ≤ 15, -25 ≤ l ≤ 25
Reflections collected	70134	71554	74083	71483	25610	33961	23348	76797
Independent reflections	4728 [R _{int} = 0.0379, R _{sigma} = 0.0146]	4570 [R _{int} = 0.0601, R _{sigma} = 0.0218]	4764 [R _{int} = 0.0488, R _{sigma} = 0.0198]	4760 [R _{int} = 0.0421, R _{sigma} = 0.0163]	4601 [R _{int} = 0.0644, R _{sigma} = 0.0522]	1936 [R _{int} = 0.0645, R _{sigma} = 0.0201]	4966 [R _{int} = 0.1053, R _{sigma} = 0.0679]	7463 [R _{int} = 0.0464, R _{sigma} = 0.0242]
Data /restraints /parameters	4728/12/265	4570/219/257	4764/225/254	4760/30/275	4601/221/244	1936/0/112	4966/24/248	7463/25/398
<i>S</i>	1.067	1.046	1.046	1.053	1.029	1.053	1.047	1.054
Final R indexes [I > 2σ (I)]	R ₁ = 0.0295, wR ₂ = 0.0693	R ₁ = 0.0313, wR ₂ = 0.0907	R ₁ = 0.0370, wR ₂ = 0.0891	R ₁ = 0.0316, wR ₂ = 0.0999	R ₁ = 0.0554, wR ₂ = 0.1595	R ₁ = 0.0371, wR ₂ = 0.0827	R ₁ = 0.0599, wR ₂ = 0.1520	R ₁ = 0.0221, wR ₂ = 0.0527
Final R indexes [all data]	R ₁ = 0.0309, wR ₂ = 0.0701	R ₁ = 0.0382, wR ₂ = 0.0980	R ₁ = 0.0420, wR ₂ = 0.0945	R ₁ = 0.0356, wR ₂ = 0.1052	R ₁ = 0.0662, wR ₂ = 0.1764	R ₁ = 0.0539, wR ₂ = 0.1000	R ₁ = 0.0976, wR ₂ = 0.1826	R ₁ = 0.0232, wR ₂ = 0.0538
Largest diff. peak/hole / e Å ⁻³	0.70/-0.48	1.09/-0.42	0.71/-0.86	1.20/-0.57	1.61/-0.79	0.30/-0.23	3.72/-1.51	0.95/-0.75

A.5. PXRD Diffractograms

A.5.1. PXRD Analysis of Reactive Cage•Guest Materials Made *via* Milling

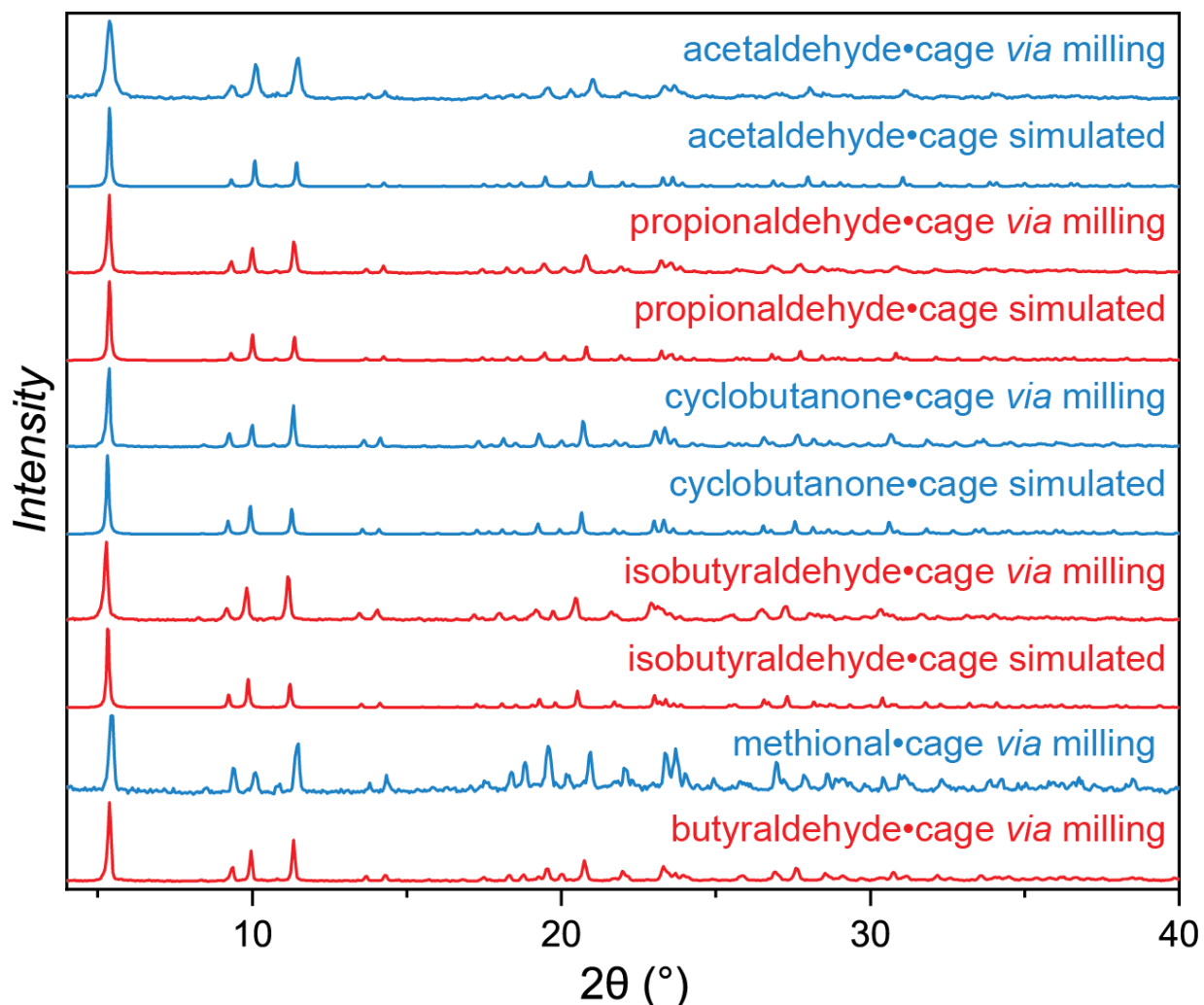


Fig A.5.1. PXRD Patterns for 1•reactive guest material made by milling. Microcrystalline 1•reactive guest materials made by milling show PXRD patterns which match those simulated from scXRD structures, if collected.

A.5.2. PXRD Analysis of the desolvation and neat ball milling of **1**

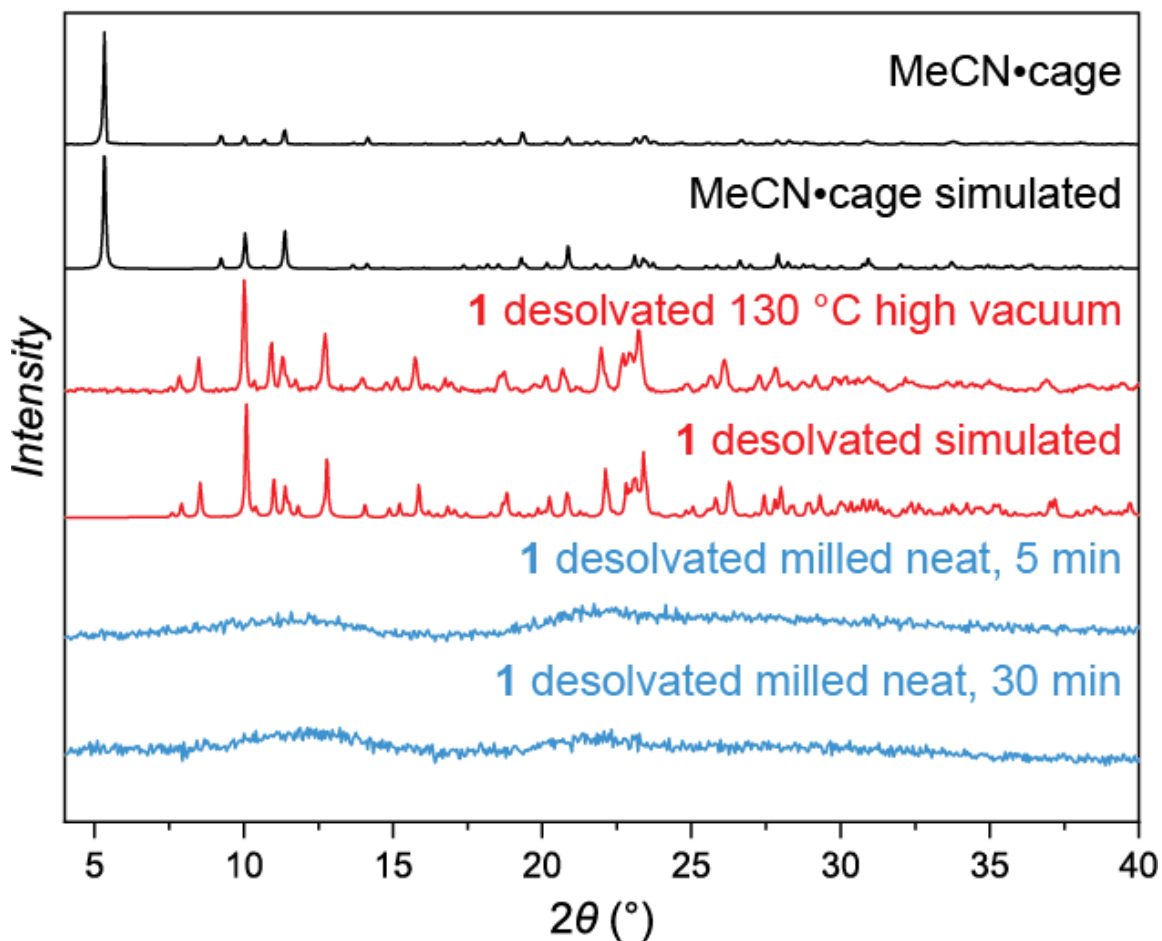


Fig A.5.2. PXRD Patterns for **1•MeCN, desolvation to **1**, and its amorphization under milling conditions.** Microcrystalline **1**•MeCN is exposed to 130 °C and high vacuum for 14 hours to cause conversion to the desolvated **1** phase. **1** rapidly becomes amorphous when milled alone under the same conditions used to incorporate reactive guests.

A.5.3 PXRD Analysis of the synthesis of **2**

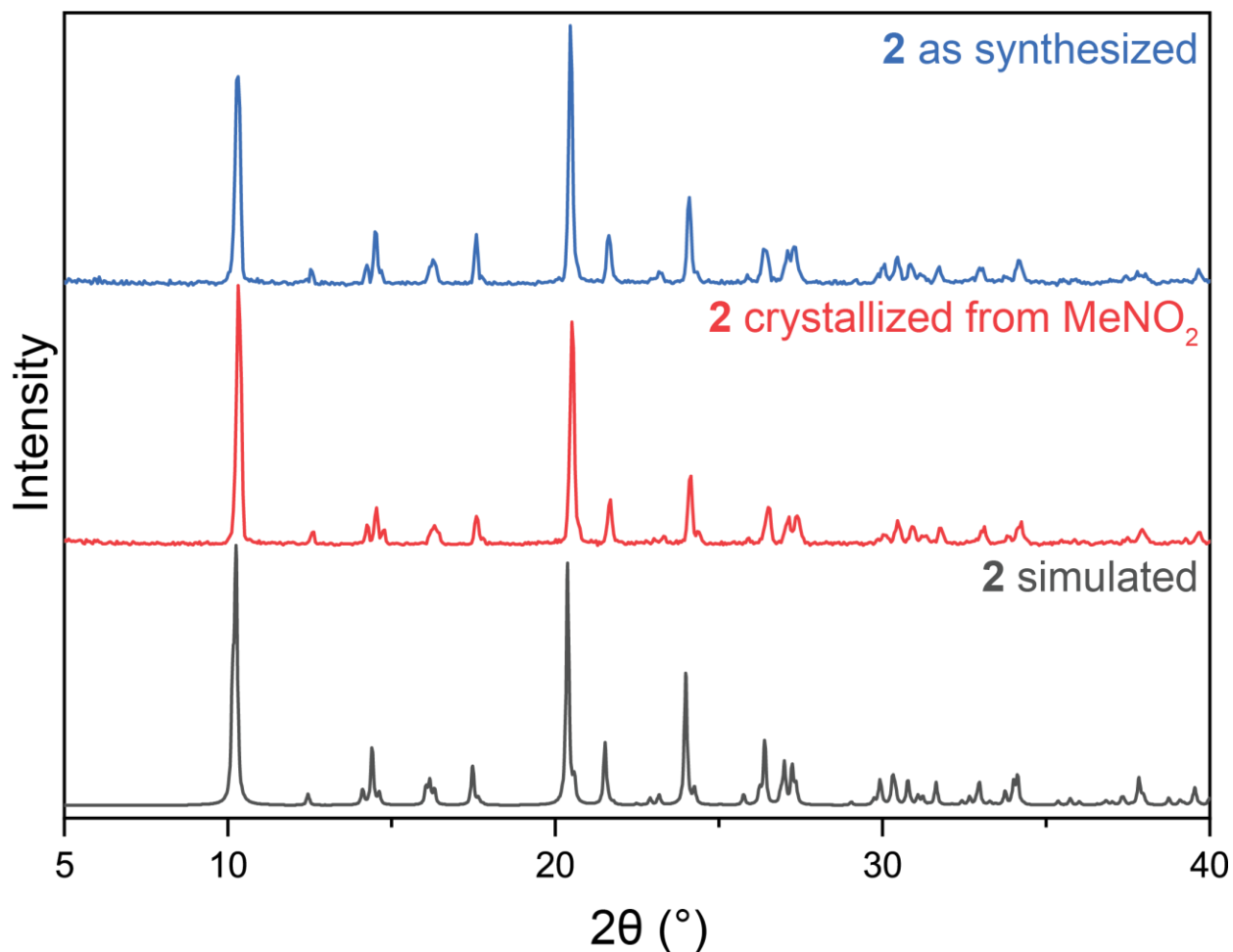


Fig A.5.3. PXRD Patterns for (dichloromethyl)triphenylphosphonium chloride, **2.** PXRD patterns of **2** as synthesized from benzene and recrystallized from nitromethane match the simulated pattern for **2** based on its scXRD structure.

A.5.4 PXRD Analysis of the synthesis of 3 and 4

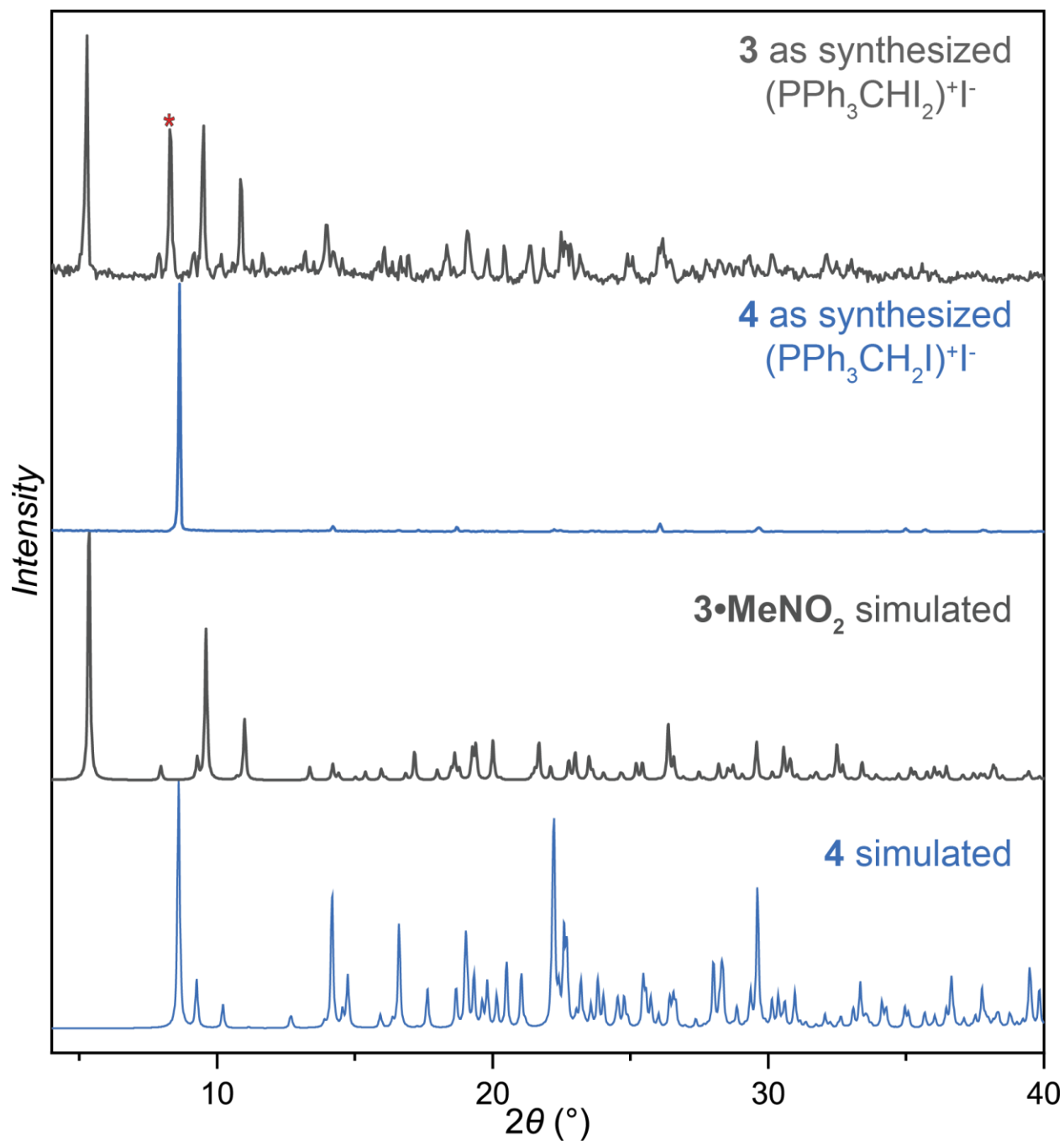


Fig A.5.4. PXRDs for the synthesis of 3, (PPh₃CHI₂)^{+I⁻}, and its decomposition product 4, (PPh₃CH₂I)^{+I⁻}. The salt 3 is synthesized with unknown crystalline impurities, a major peak of which is denoted by '*'. Attempting to recrystallize 3 from hot MeNO₂ results in the decomposition to 4. The PXRD pattern of 4 shows heavy preferred orientation, reducing the intensities of many peaks.

A.6. Thermogravimetric Analysis

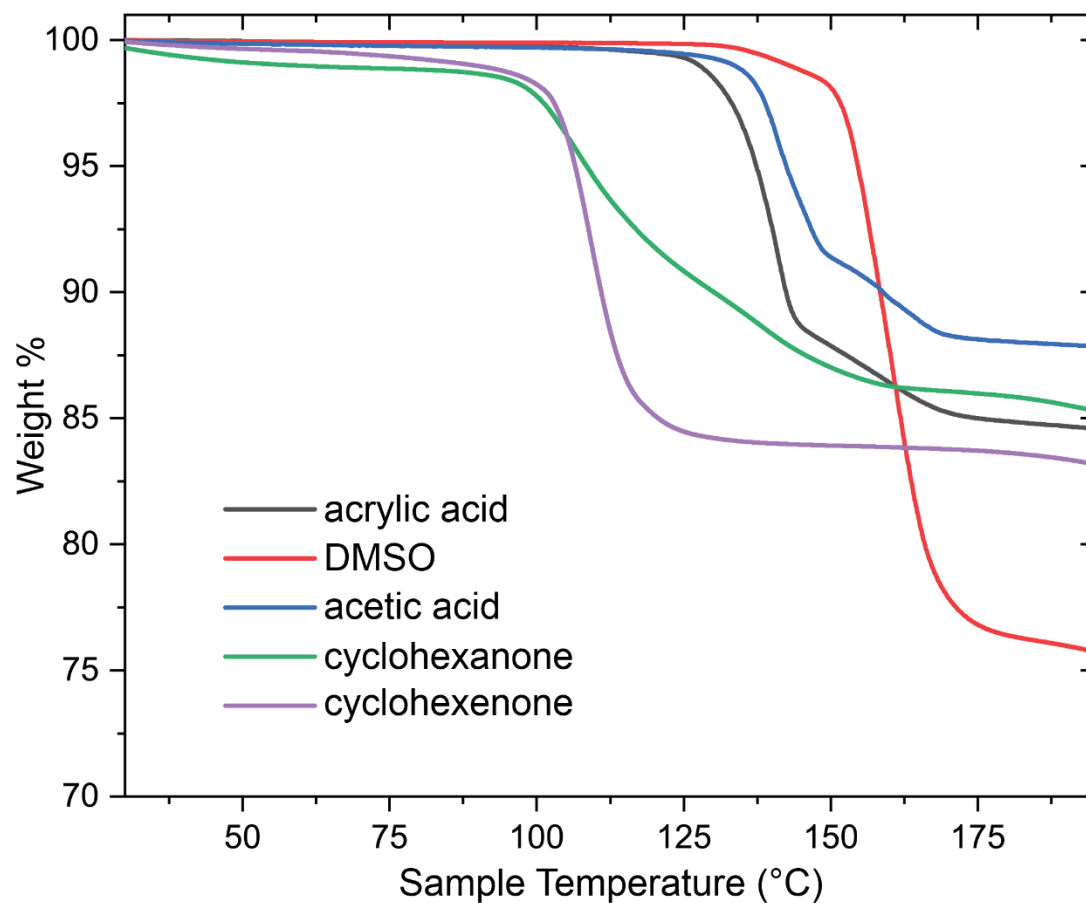


Fig A.6.1. TGA thermograms for guests which do not produce desolvated 1 in a well-defined step. For acrylic acid, acetic acid, and DMSO, no flat section is observed after the initial weight loss. For cyclohexanone and cyclohexenone, no flat initial baseline can be obtained despite careful washing and drying.

A.7. Guest loadings as determined by TGA and solution ^1H NMR

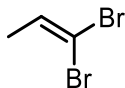
material	guests per cage (TGA)	guests per cage (^1H NMR)
1•acetaldehyde	6.9	6.5
1•MeCN	8.1	6.8
1•propionaldehyde	6.0	5.9
1•acetone	6.6	5.7
1•butanone	6.0	5.6
1•MeNO₂	7.1	6.2
1•cyclobutanone	6.7	6.2
1•methional	5.1	3.7
1•DMA	6.1	6.0
1•DMF	7.4	6.8
1•NMP	6.4	6.0
1•isobutyraldehyde	7.7	4.3
1•butyraldehyde	4.9	4.4
1•acetic acid	-	7.1
1•acrylic acid	-	-
1•DMSO	-	7.0
1•cyclohex-2-enone	-	5.4
1•cyclohexanone	-	4.4

Table A.7.1. Guests per cage as determined by TGA and ^1H NMR. Determinations based on TGA data presented in main text. By ^1H NMR, the number of guests per cage was determined by dissolving microcrystalline **1•guest** material in CDCl_3 and comparing ^1H NMR signal integrations for characteristic peaks of the host and the guest. ^1H NMR spectra shown in section A.9.

A.8. Analysis of organic products

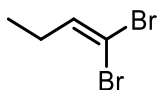
See section A.12 for raw spectra.

1,1-dibromopropene



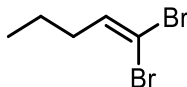
Colorless liquid isolated by distillation from the contents of the jar after milling. ^1H NMR (500 MHz, CDCl_3): 1.71 (d, $J = 6.8$ Hz, 3H), 6.46 (q, $J = 6.8$ Hz, 1H). ^{13}C NMR (125 MHz, CDCl_3): 18.5 (CH_3), 89.6 ($\text{C}_{\text{dibromo}}$), 133.5 (CH). GCMS (m/z): $[\text{M}]^+$ calculated for $\text{C}_3\text{H}_4\text{Br}_2$: 199.9; found: 200.

1,1-dibromobutene



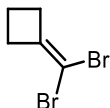
Colorless liquid, isolated by distillation from jar contents. ^1H NMR (500 MHz, CDCl_3): 1.04 (t, $J = 7.5$ Hz, 3H), 2.12 (p, $J = 7.5$ Hz, 2H), 6.40 (t, $J = 7.2$ Hz, 1H). ^{13}C NMR (125 MHz, CDCl_3): 12.3 (CH_3), 26.5 (CH_2), 88.2 ($\text{C}_{\text{dibromo}}$), 140.1 (CH). GCMS (m/z): $[\text{M}]^+$ calculated for $\text{C}_3\text{H}_4\text{Br}_2$: 213.9; found: 214.

1,1-dibromopentene



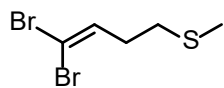
Colorless liquid, isolated by distillation from jar contents. ^1H NMR (500 MHz, CDCl_3): 0.95 (t, $J = 7.4$ Hz, 3H), 1.46 (h, $J = 7.4$ Hz, 2H), 2.09 (q, $J = 7.3$ Hz, 2H), 6.41 (t, $J = 7.2$ Hz, 1H). ^{13}C NMR (125 MHz, CDCl_3): 13.6 (CH_3), 21.2 (CH_2), 35.0 (CH_2), 88.6 ($\text{C}_{\text{dibromo}}$), 138.7 (CH). GCMS (m/z): $[\text{M}]^+$ calculated for $\text{C}_5\text{H}_8\text{Br}_2$: 227.9; found: 228.

(dibromomethylene)cyclobutane



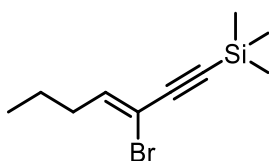
Colorless liquid, isolated by column chromatography in 100% hexanes. ^1H NMR (500 MHz, CDCl_3): 1.91 (p, $J = 8.0$ Hz, 2H), 2.63 (t, $J = 8.0$ Hz, 2H). ^{13}C NMR (125 MHz, CDCl_3): 13.4 (CH_2), 32.6 (CH_2), 78.9 ($\text{C}_{\text{dibromo}}$), 147.3 (C). GCMS (m/z): $[\text{M}]^+$ calculated for $\text{C}_5\text{H}_8\text{Br}_2$: 225.9; found: 226.

1,1-dibromo-4-methylthiobutene



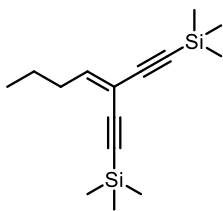
Colorless liquid, isolated by column chromatography in 100% hexanes. ^1H NMR (500 MHz, CDCl_3): 2.14 (s, 3H), 2.41 (q, $J = 7.2$ Hz, 2H), 2.59 (t, $J = 7.3$ Hz, 2H), 6.50 (t, $J = 7.1$ Hz, 1H). ^{13}C NMR (125 MHz, CDCl_3): 15.4 (CH_3), 32.0 (CH_2), 32.5 (CH_2), 90.3 ($\text{C}_{\text{dibromo}}$), 136.5 (CH). APCI-HRMS (m/z): $[\text{M}+\text{H}]^+$ calculated for $\text{C}_5\text{H}_9\text{Br}_2\text{S}$: 258.8792 ; found: 258.8786.

Monocoupled (eneyne) Sonogashira product



Yellow oil, isolated by column chromatography in 100% hexanes. Co-elutes with trimethylsilylacetylene homocoupling dimer, marked in NMR spectra. ^1H NMR (500 MHz, CDCl_3): 0.22 (s, 9H), 0.96 (t, $J = 7.4$ Hz, 3H), 1.47 (h, $J = 7.3$ Hz, 2H), 2.21 (q, $J = 7.3$ Hz, 2H), 6.35 (t, $J = 7.2$ Hz, 1H). ^{13}C NMR (125 MHz, CDCl_3): -0.3 (CH_3TMS) 13.8 (CH_3), 21.2 (CH_2), 34.0 (CH_2), 94.6 (C), 102.4 (C), 141.2 (CH). APCI-HRMS (m/z): $[\text{M}]^+$ calculated for $\text{C}_{10}\text{H}_{17}\text{BrSi}$: 244.0283; found: 244.0276.

Dicoupled (enediynes) Sonogashira product



Yellow oil, isolated by column chromatography in 100% hexanes. ^1H NMR (500 MHz, CDCl_3): 0.20 (s, 9H), 0.22 (s, 9H), 0.95 (t, $J = 7.4$ Hz, 3H), 1.47 (h, $J = 7.4$ Hz, 2H), 2.33 (q, $J = 7.4$ Hz, 2H), 6.42 (t, $J = 7.7$ Hz, 1H). ^{13}C NMR (125 MHz, CDCl_3): -0.1 (CH_3TMS), 13.8 (CH_3), 21.7 (CH_2), 32.8 (CH_2), 91.5 (C), 98.4 (C), 99.8 (C), 102.5 (C), 106.0 (C), 151.8 (CH). APCI-HRMS (m/z): $[\text{M}]^+$ calculated for $\text{C}_{15}\text{H}_{26}\text{Si}_2$: 262.1564; found: 262.1568.

A.9. ¹H NMR quantitative methods

A.9.1. Guest per cage calculation

The phenyl protons of **1** are used as a standard. Integrations are such that the signals which correspond to 6 protons of **1** are set to an integration value of 1. A characteristic peak of the guest molecule is chosen, divided by the number of protons it corresponds to on the guest, then multiplied by six to obtain the number of guests per salt **1**. Multiplying this number by 6 gives the approximate number of guest molecules per hexameric cage.

A.9.2. Wittig olefination conversion calculations

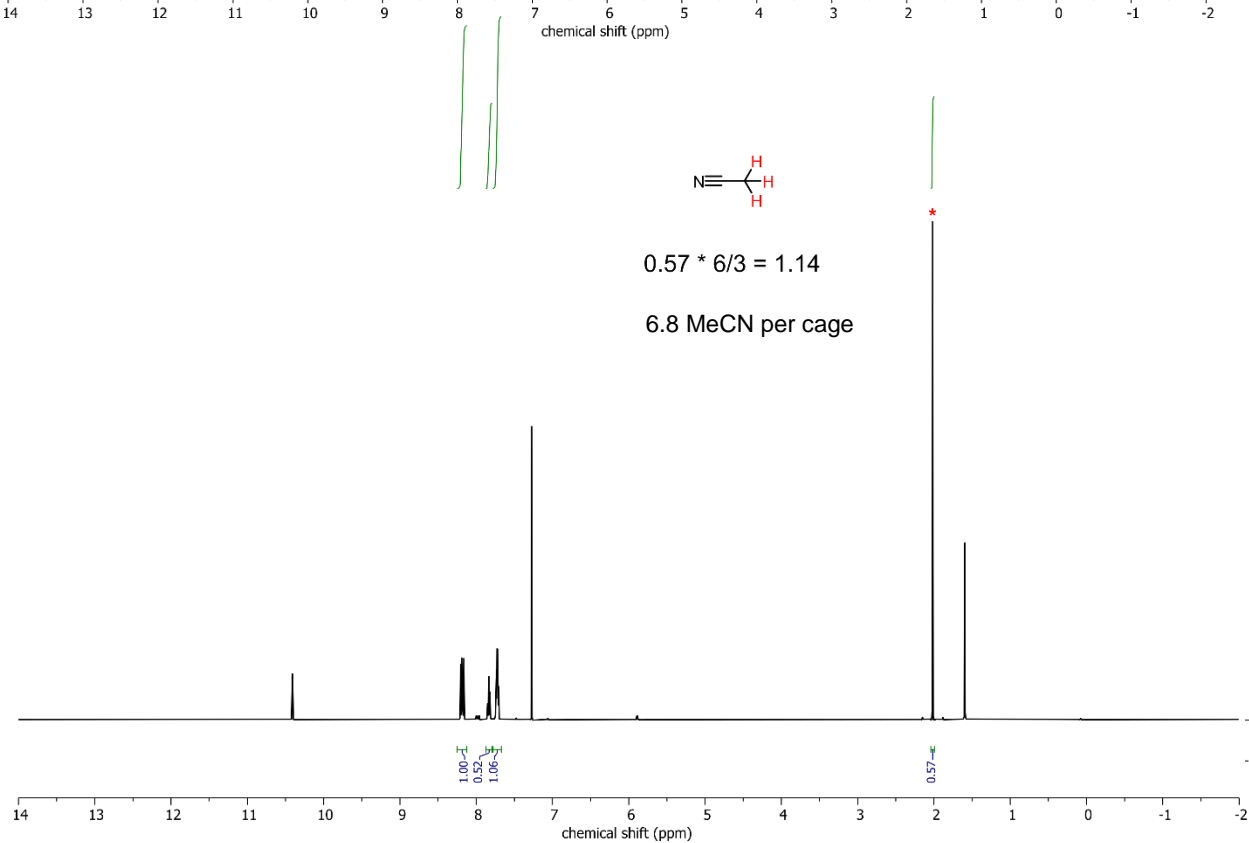
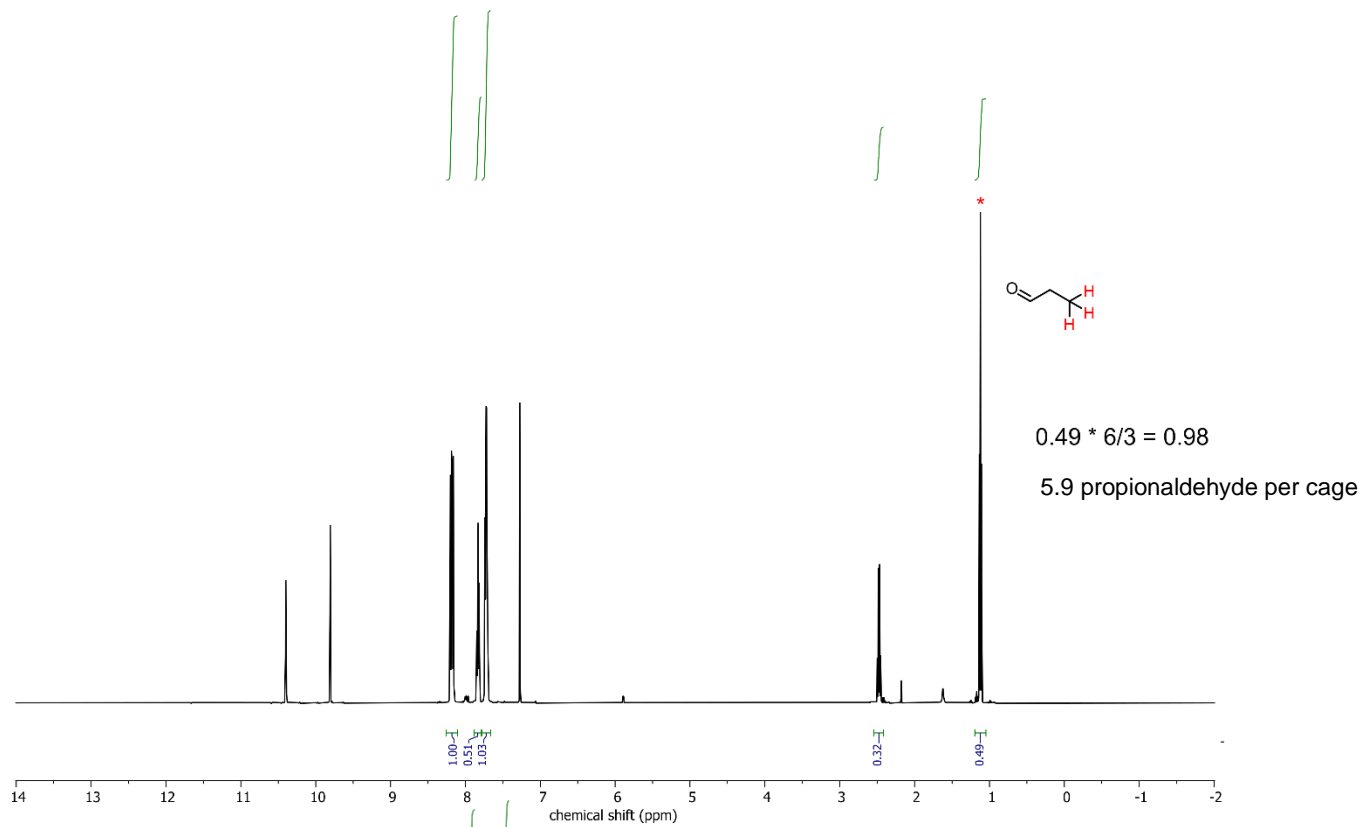
Wittig conversions were determined by comparing integrations of characteristic signals from the 1,1-dihaloolefin product with characteristic signals from the aldehyde or ketone guest.

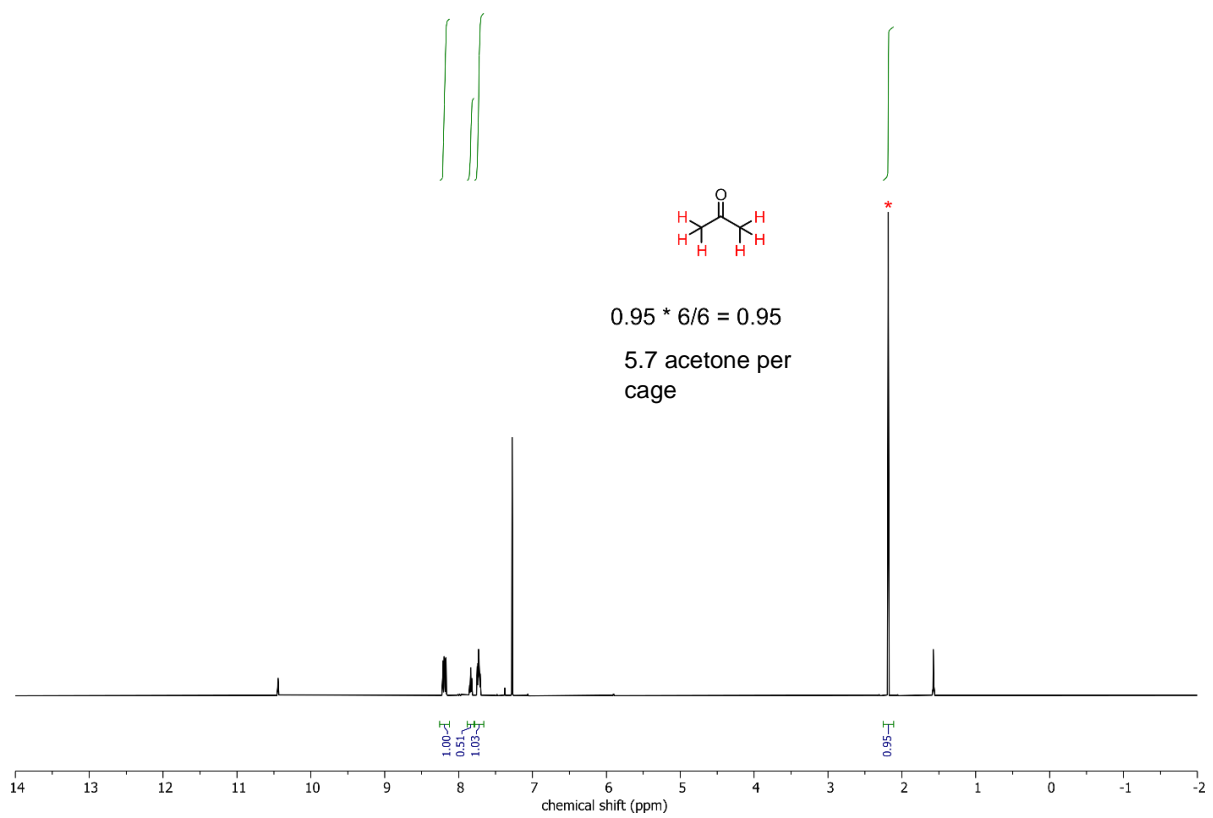
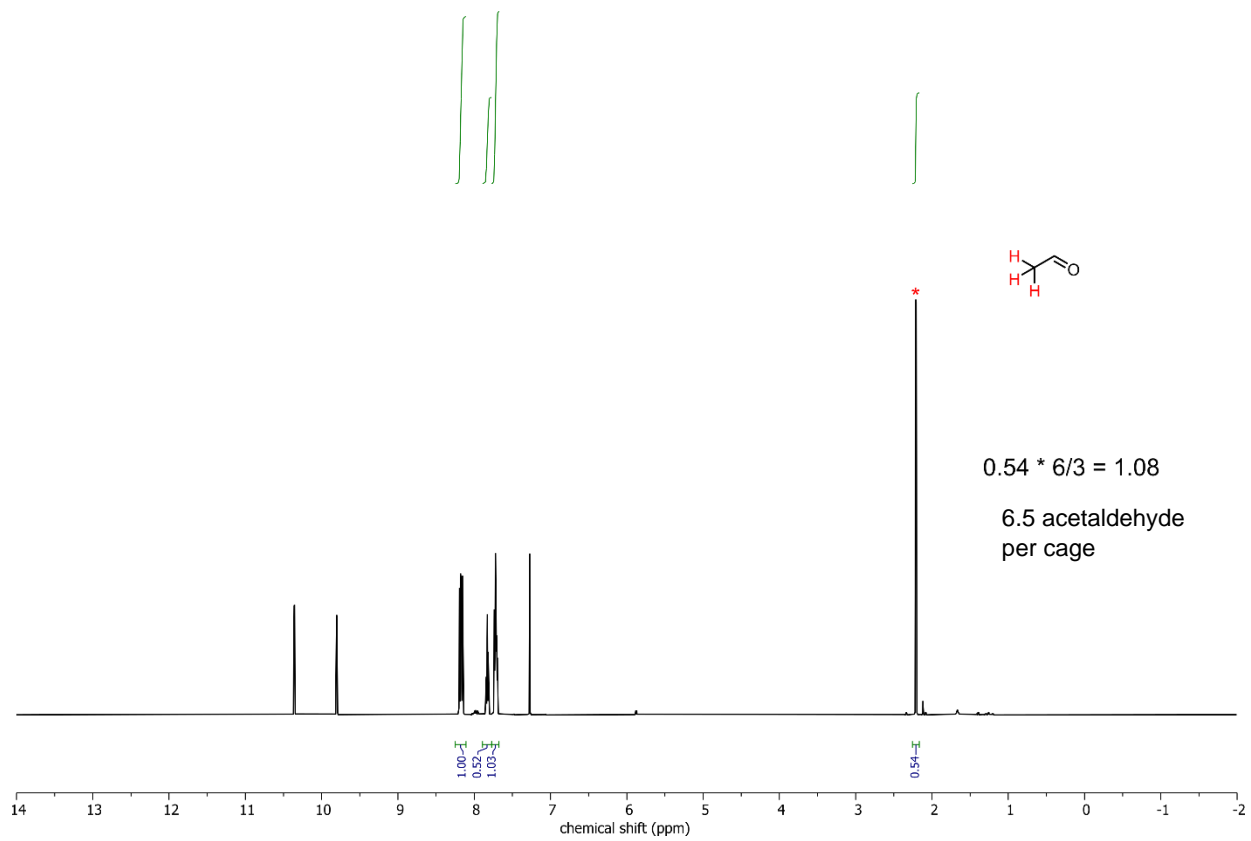
A.9.3. Sonogashira and one-pot Sonogashira/Wittig reaction conversion calculation

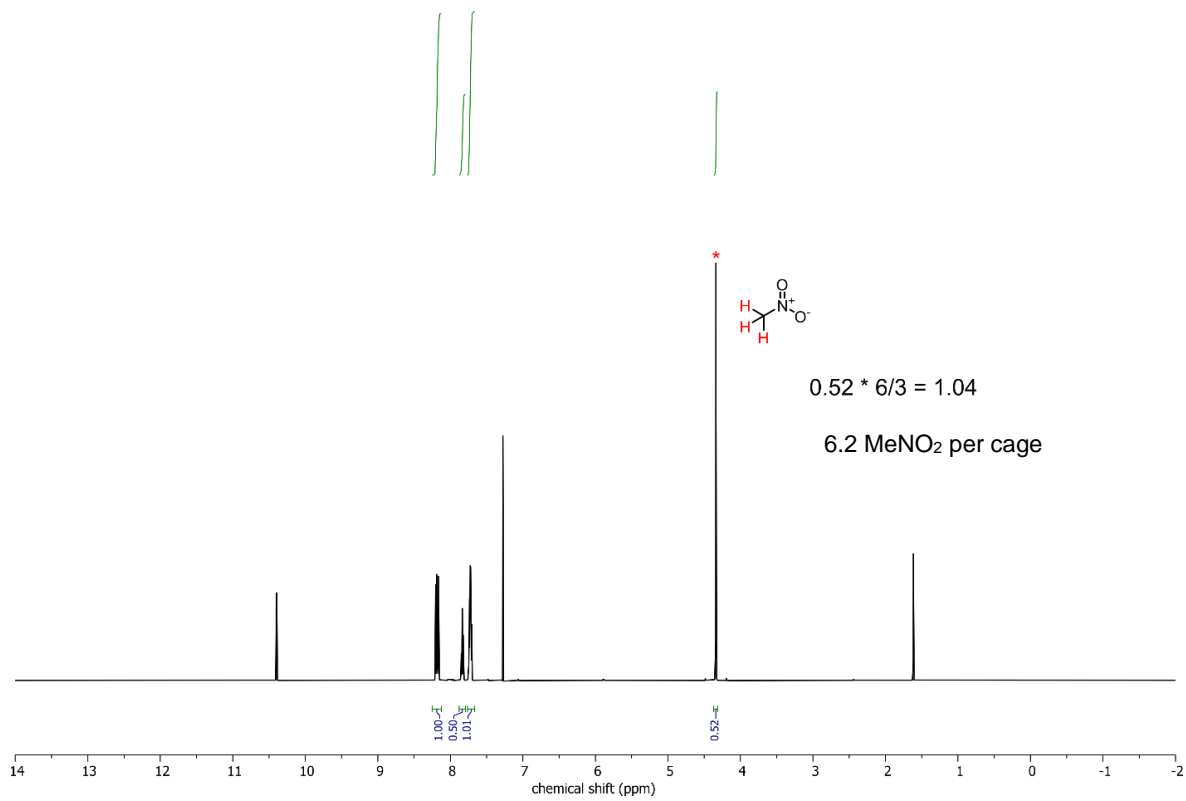
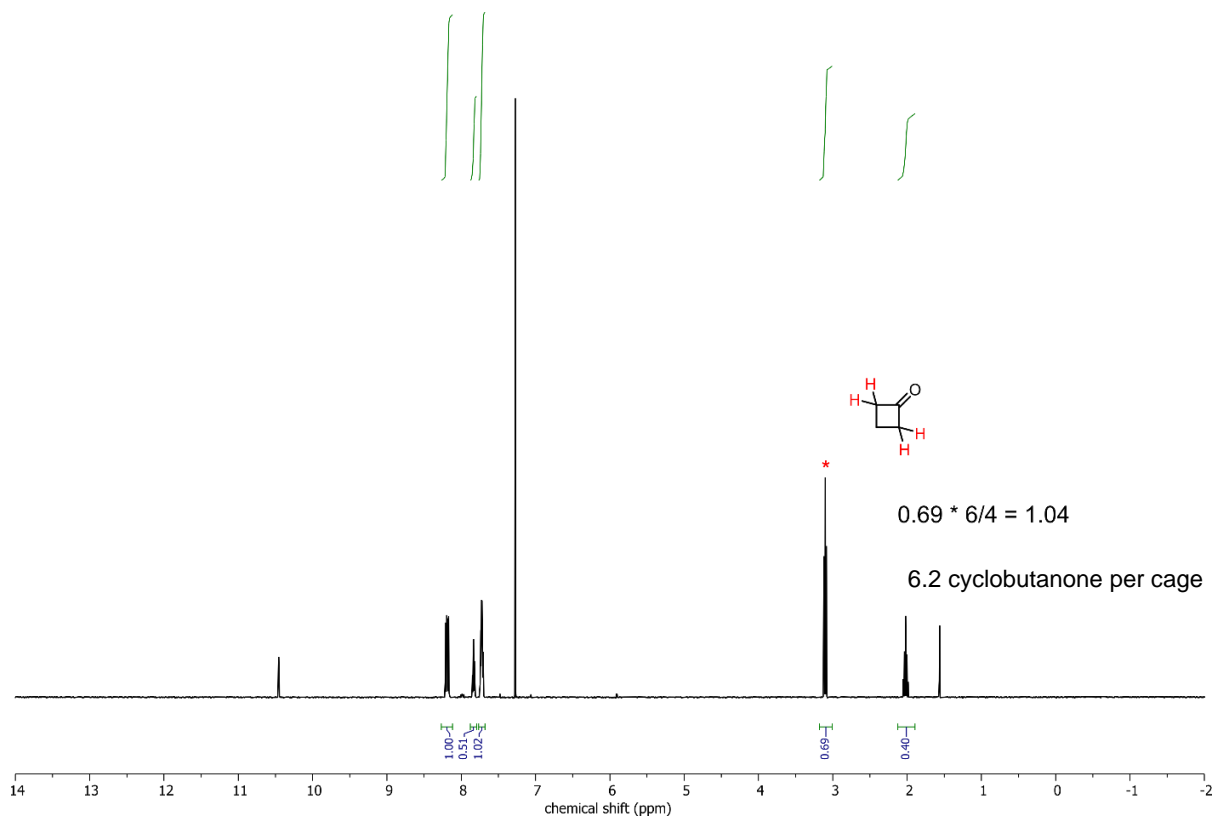
Originally, a method identical the one for the calculation of yields for the Wittig olefinations was used for the one-pot reactions, where the ¹H NMR signal integrations for starting materials and olefin products were directly compared. However, conversions did not match determined in this way showed a marked discrepancy from isolated yields, so an alternative method was used which matches yields and conversions more accurately.

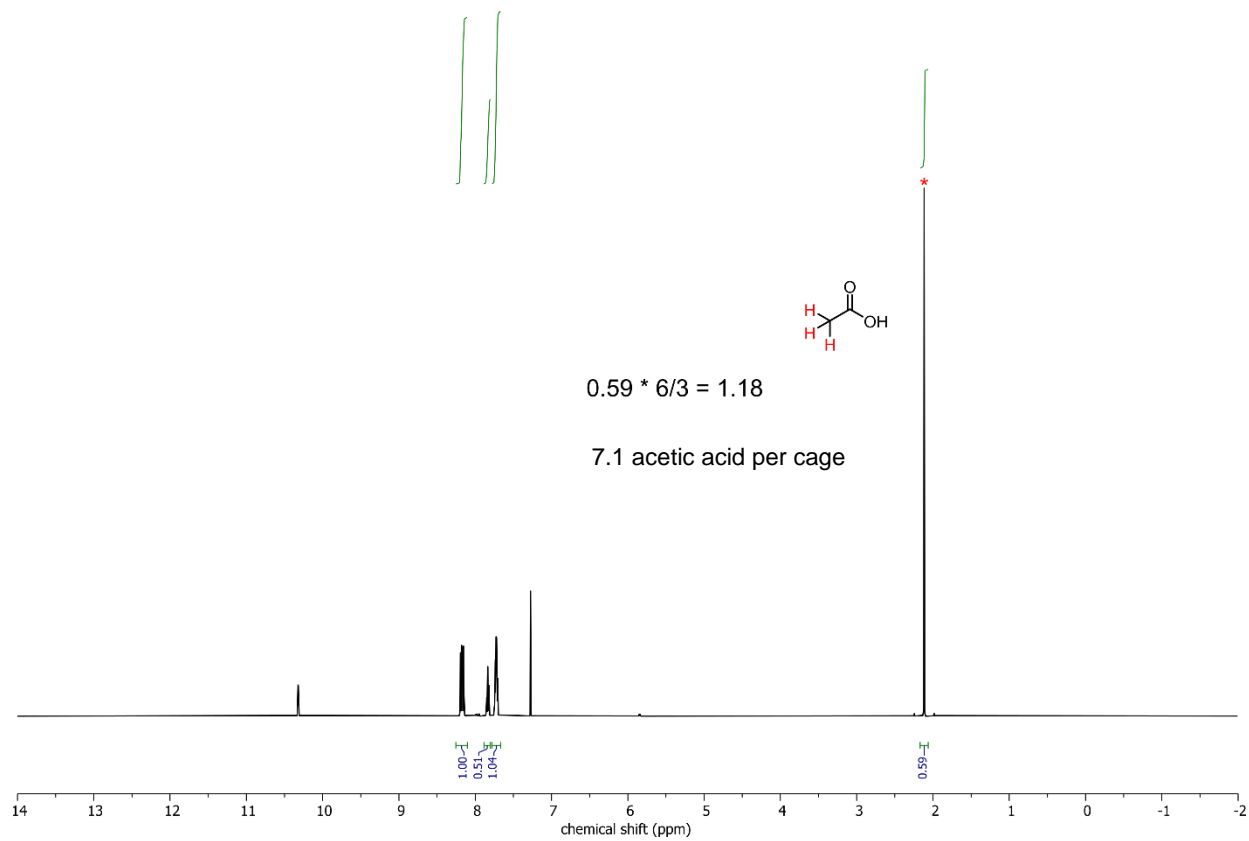
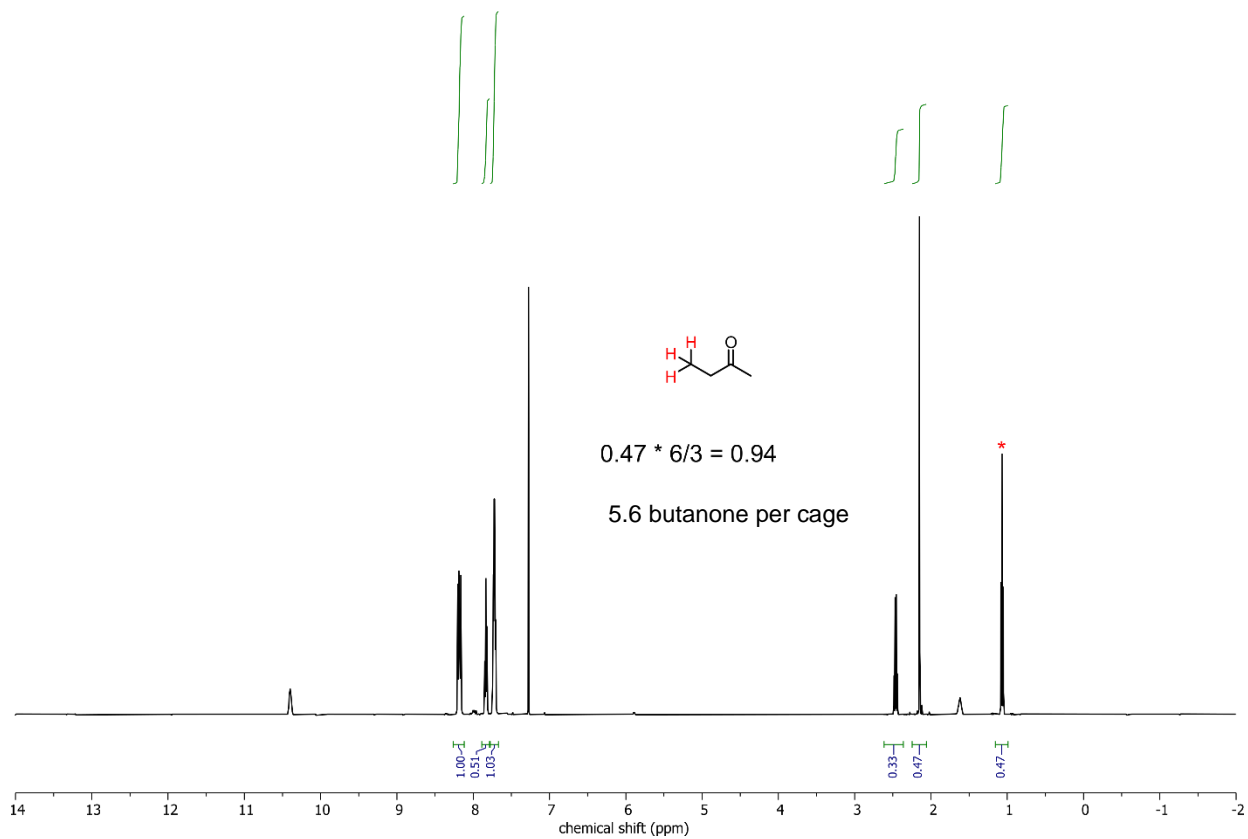
In this method, the reaction byproduct triphenylphosphine oxide (TPPO) was used as an internal standard. This method assumes that one equivalent of cage material produces one equivalent of TPPO during the reaction. Given the known initial quantity of cage material and guest, all product signal integrations can be compared to TPPO, to derive an approximate conversion. Importantly, this method accounts for reactant or product which may be lost to processes like polymerization or decomposition, so the calculated conversions are uniformly lower, but more realistic, than they are for the original method.

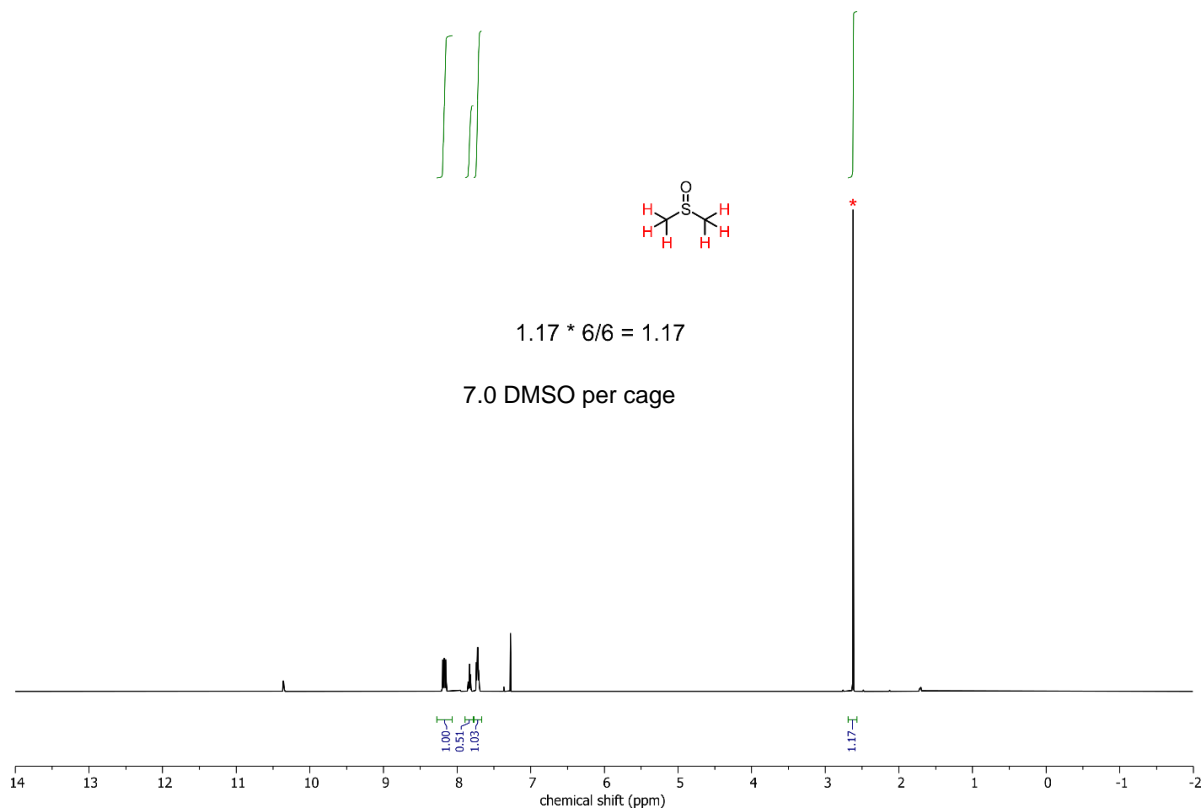
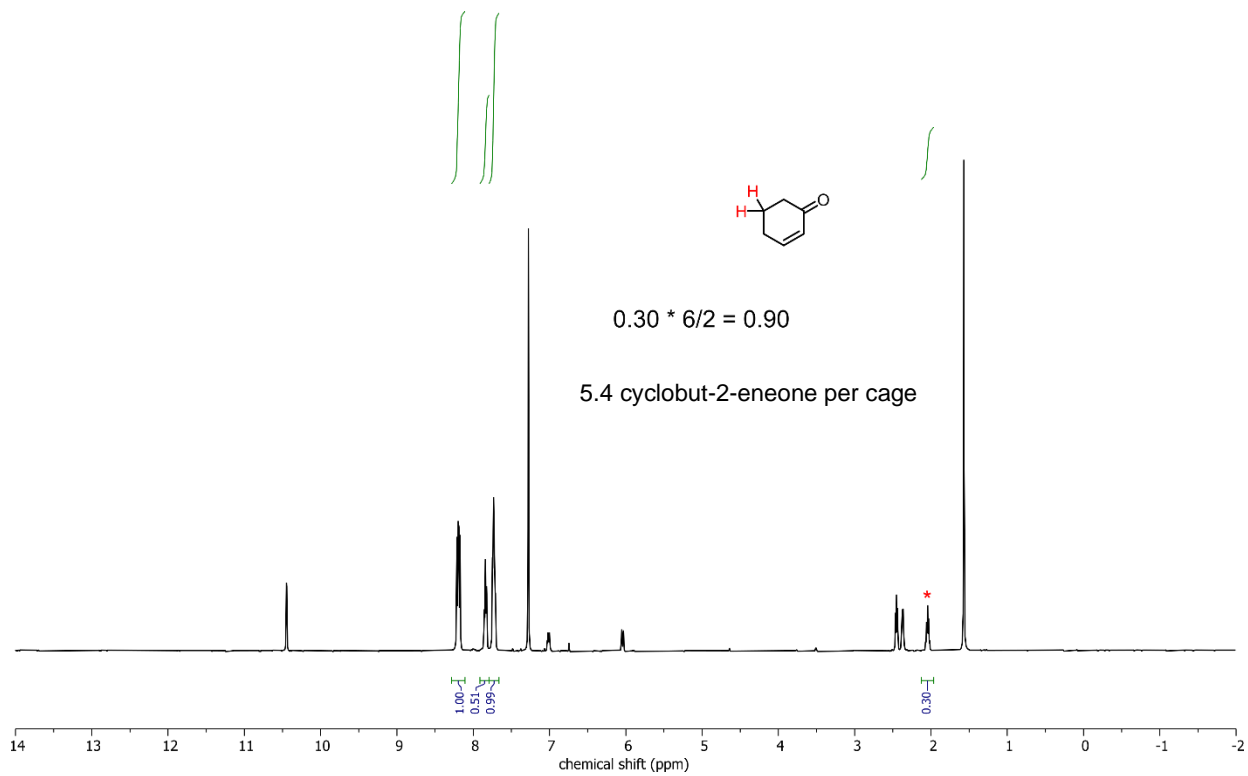
A.10. ^1H NMR spectra of 1-guest materials

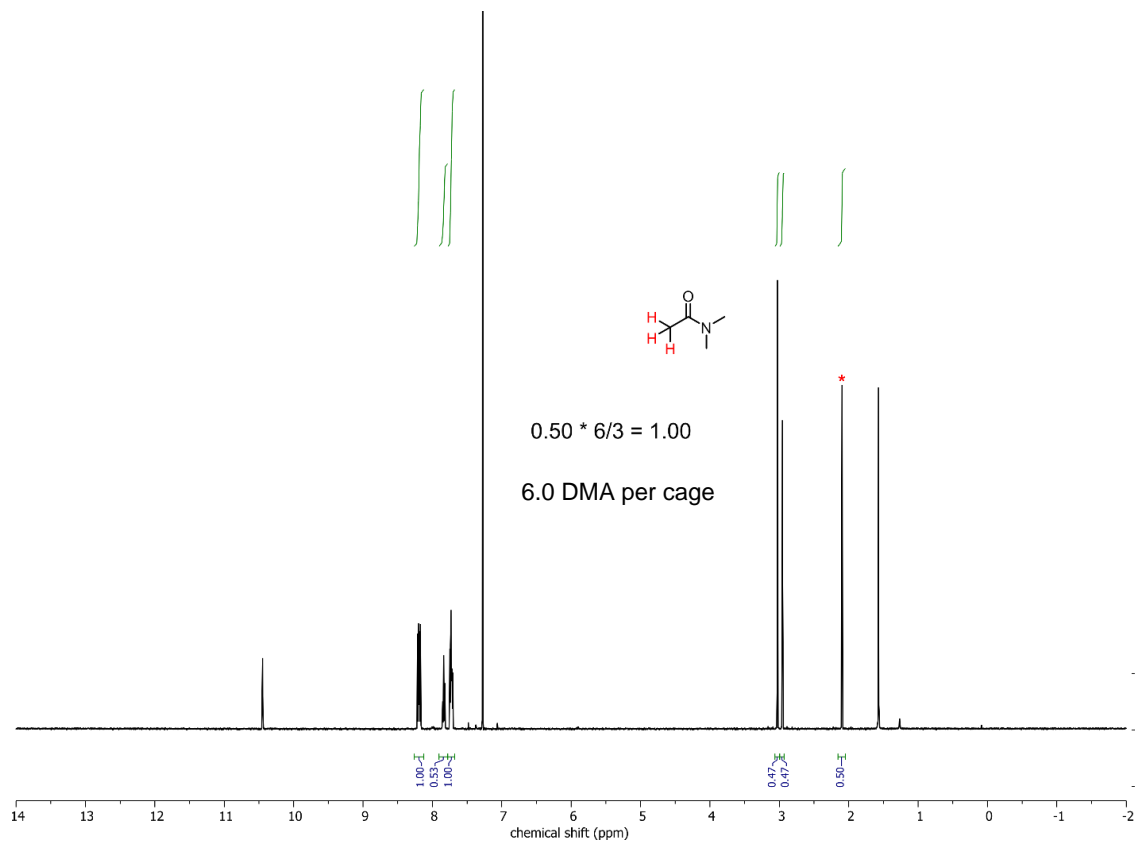
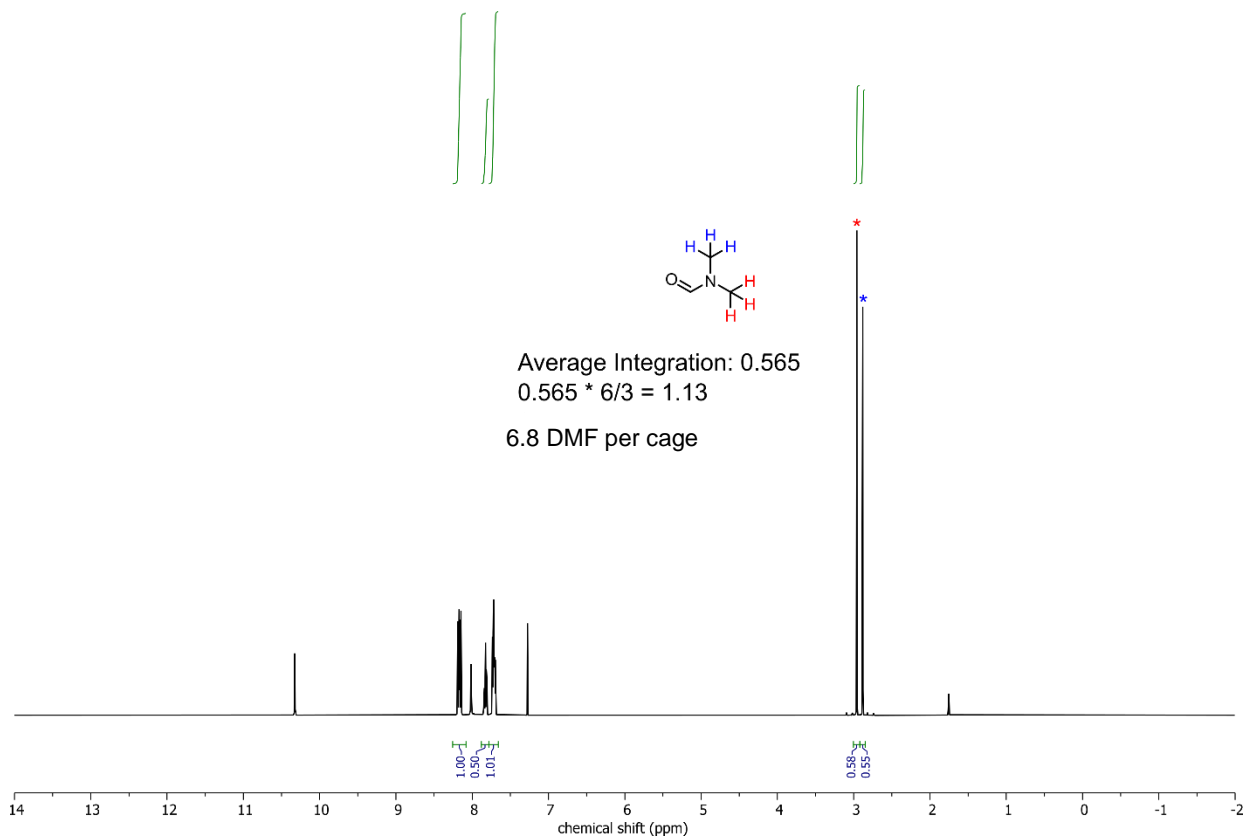


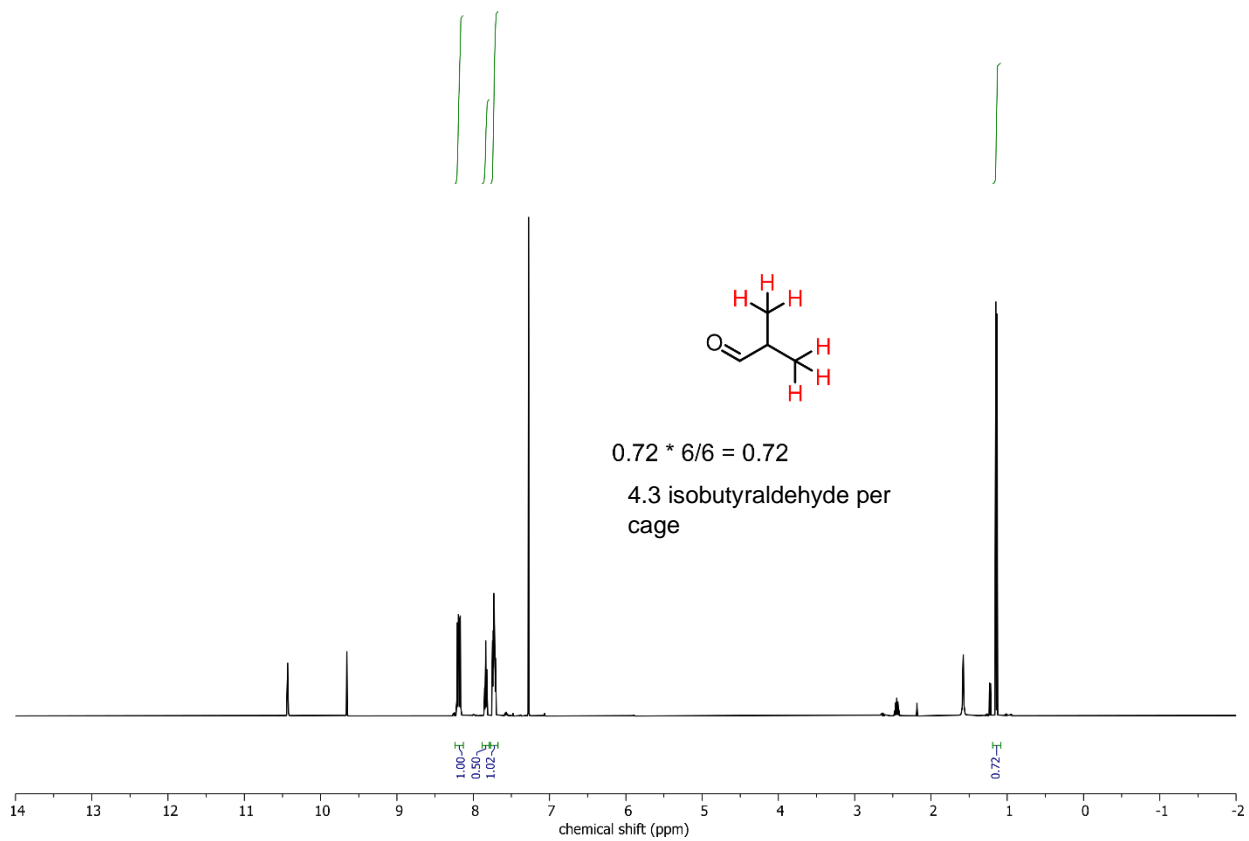
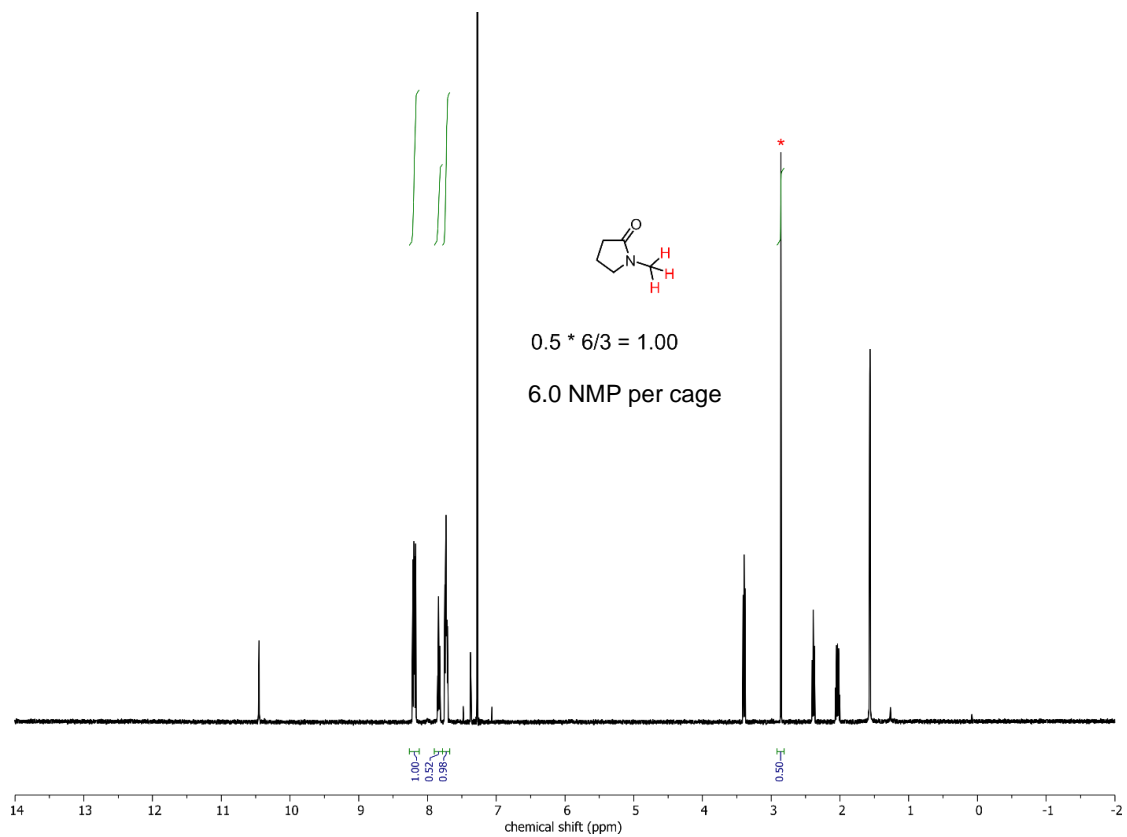


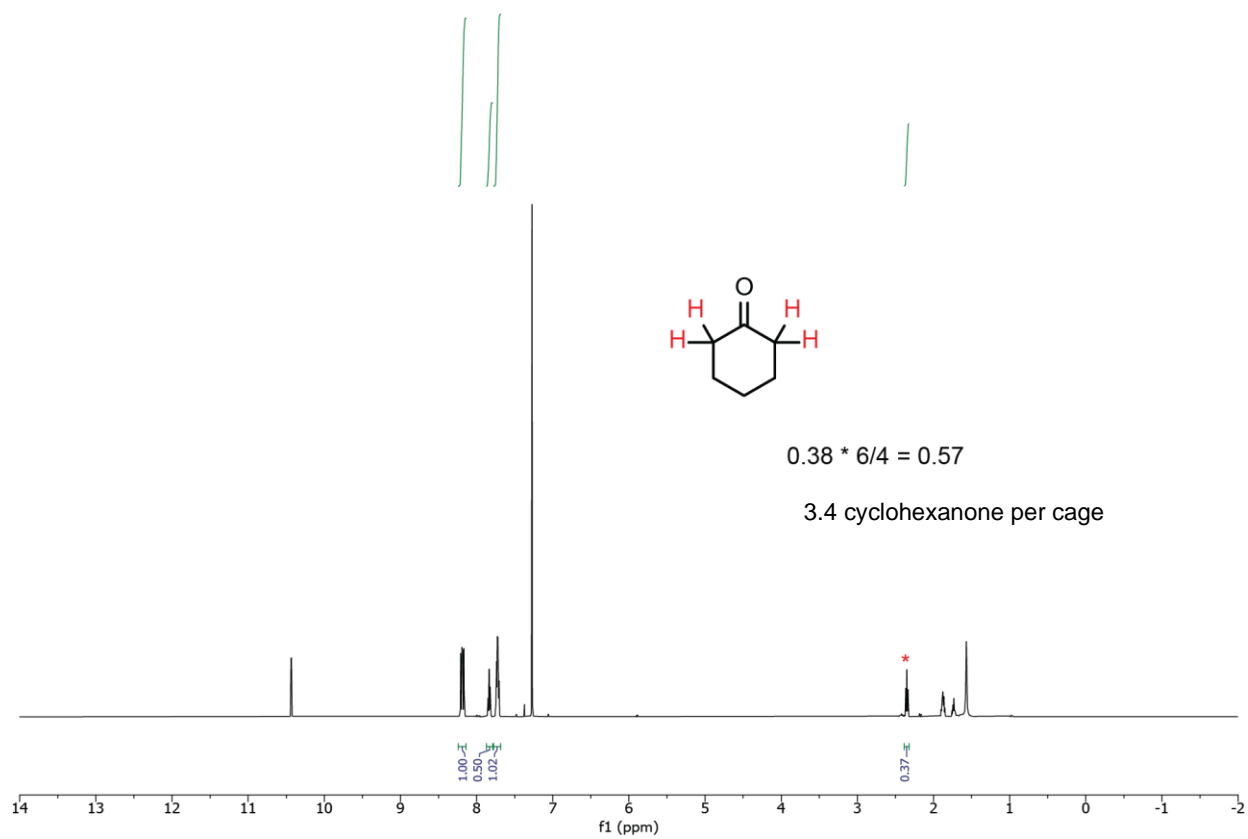
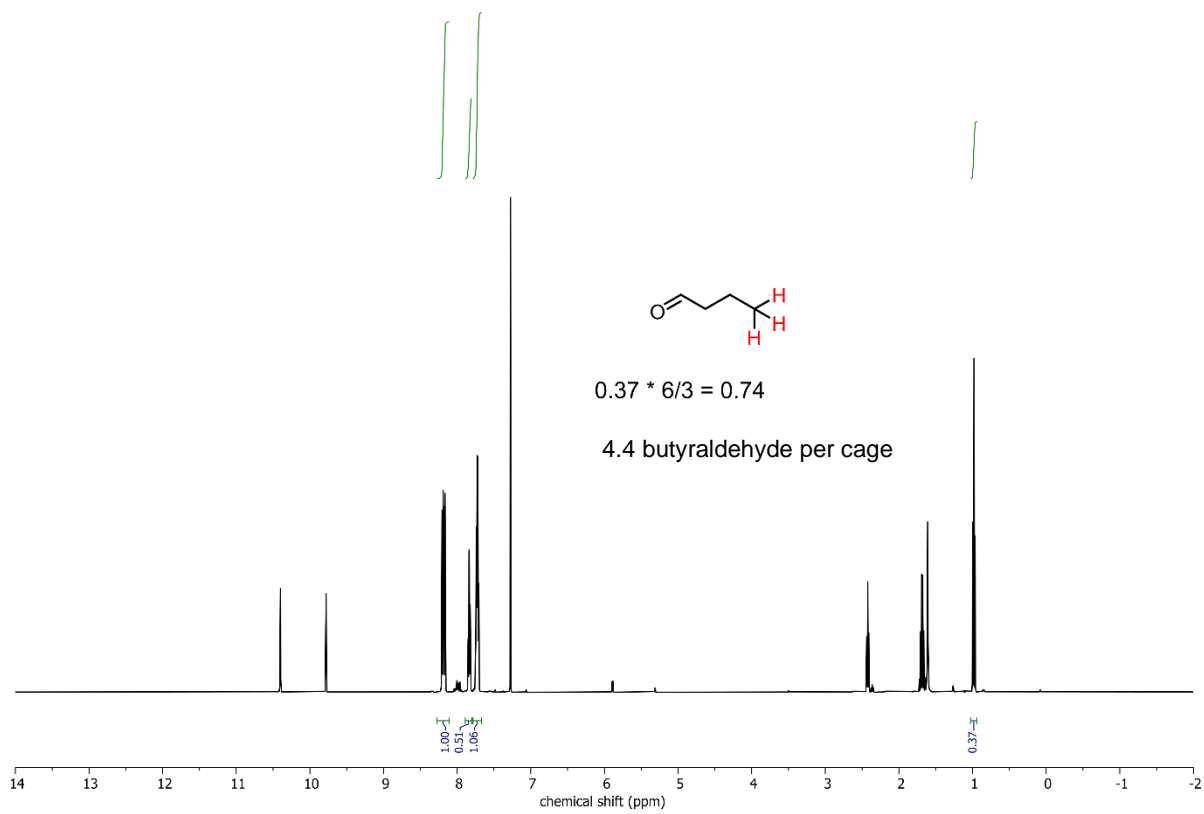




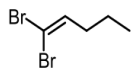




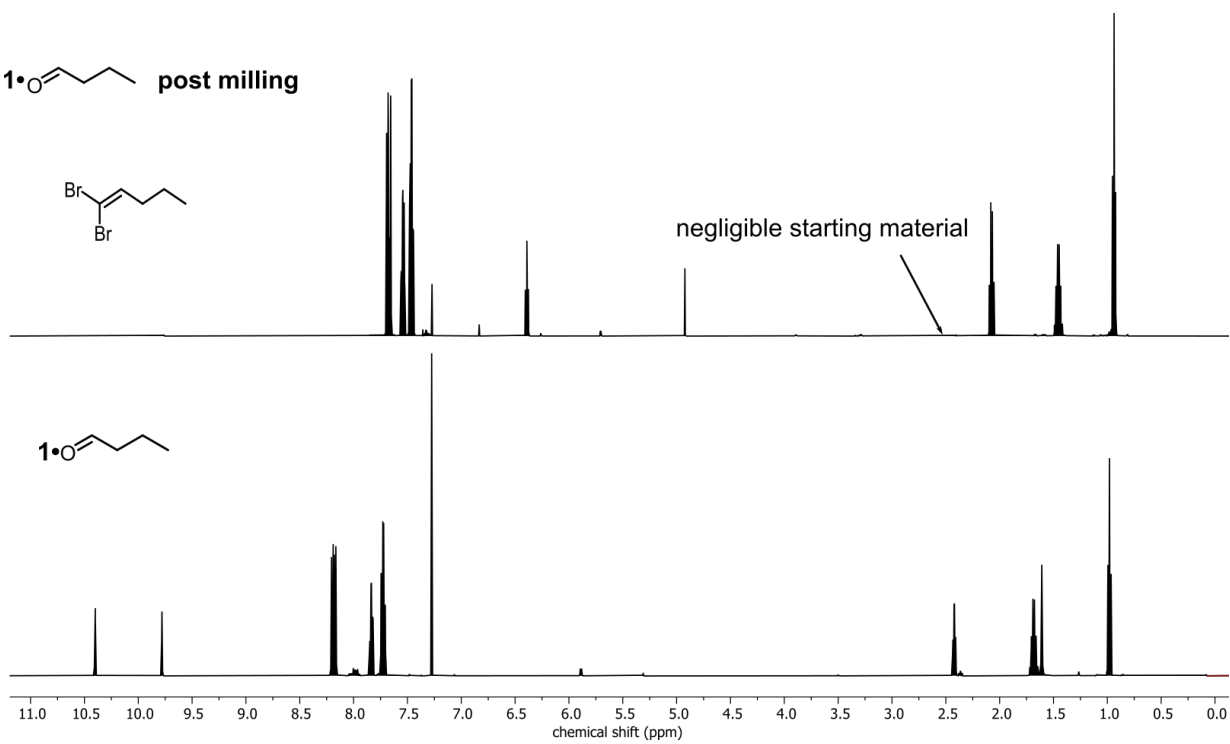




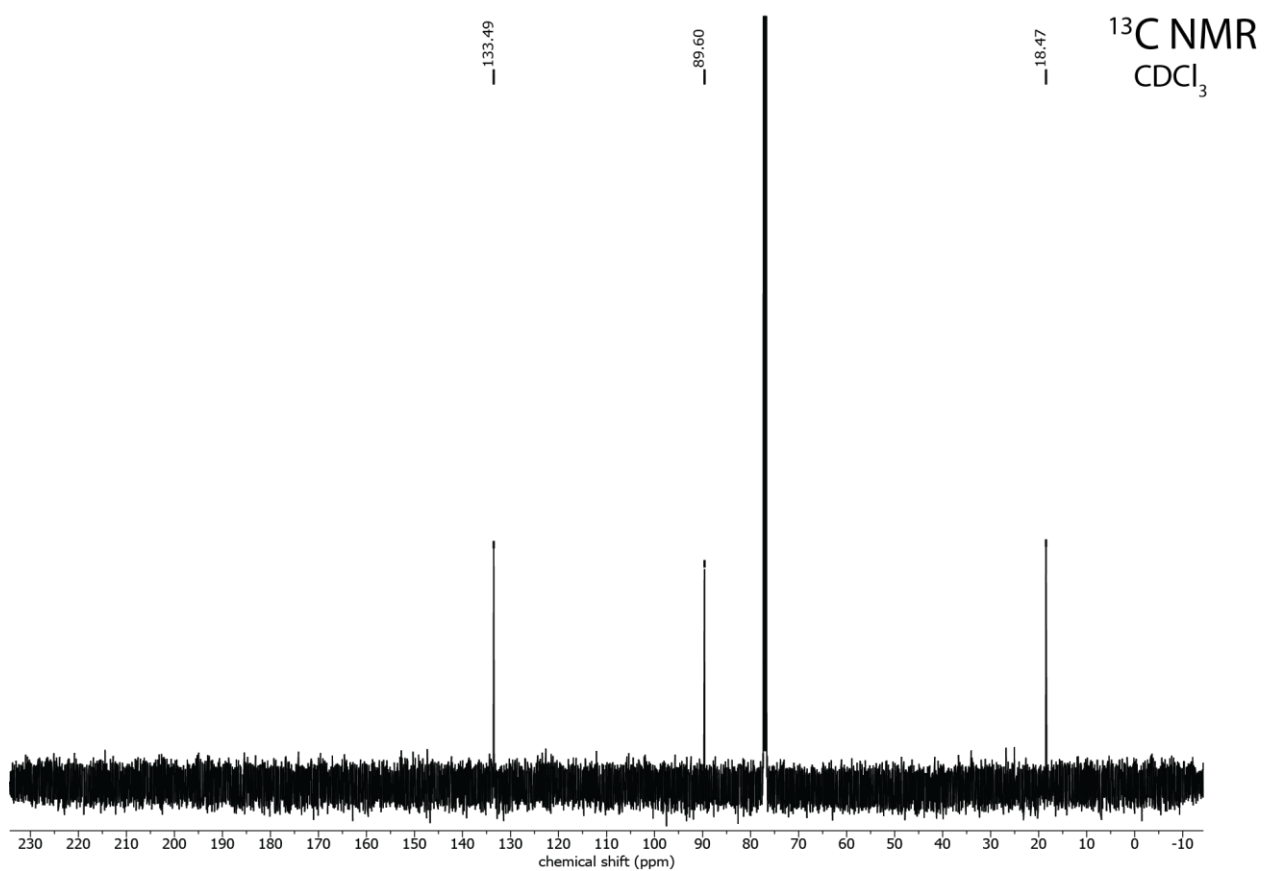
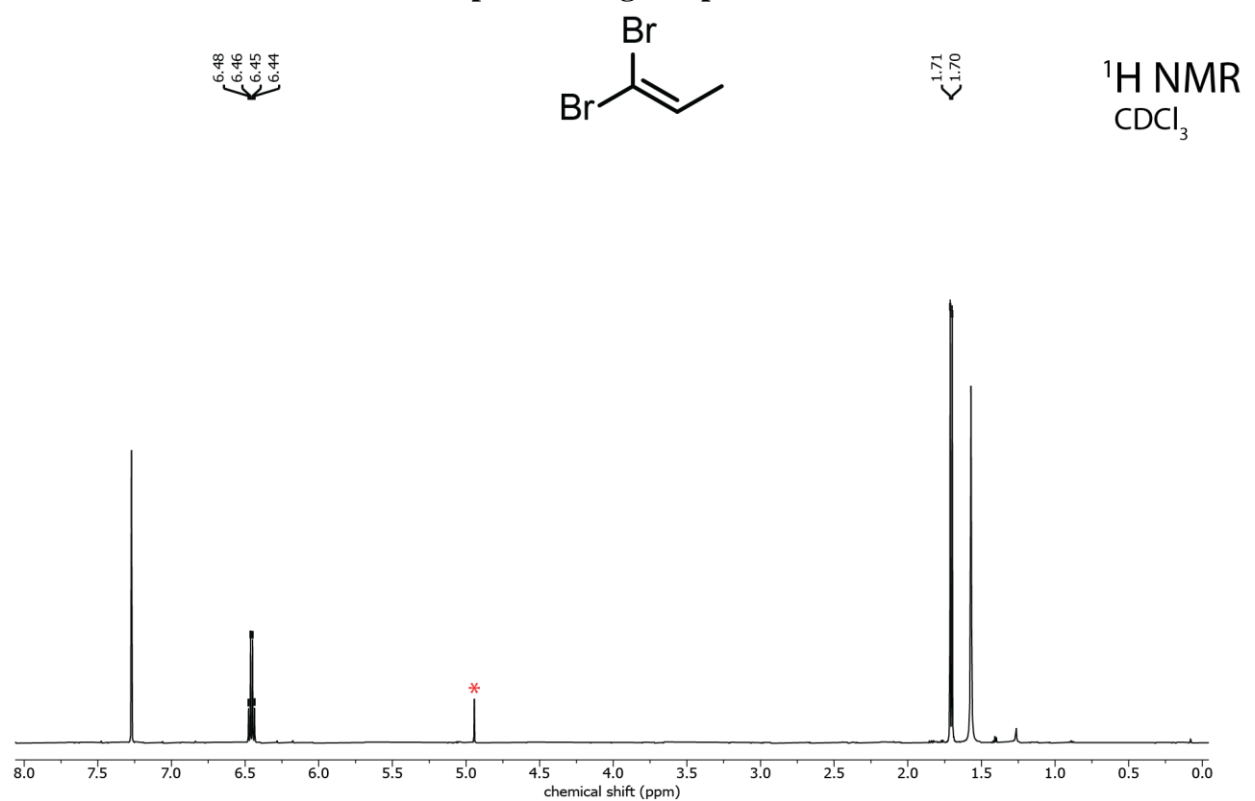
1•O= CCCC=O **post milling**

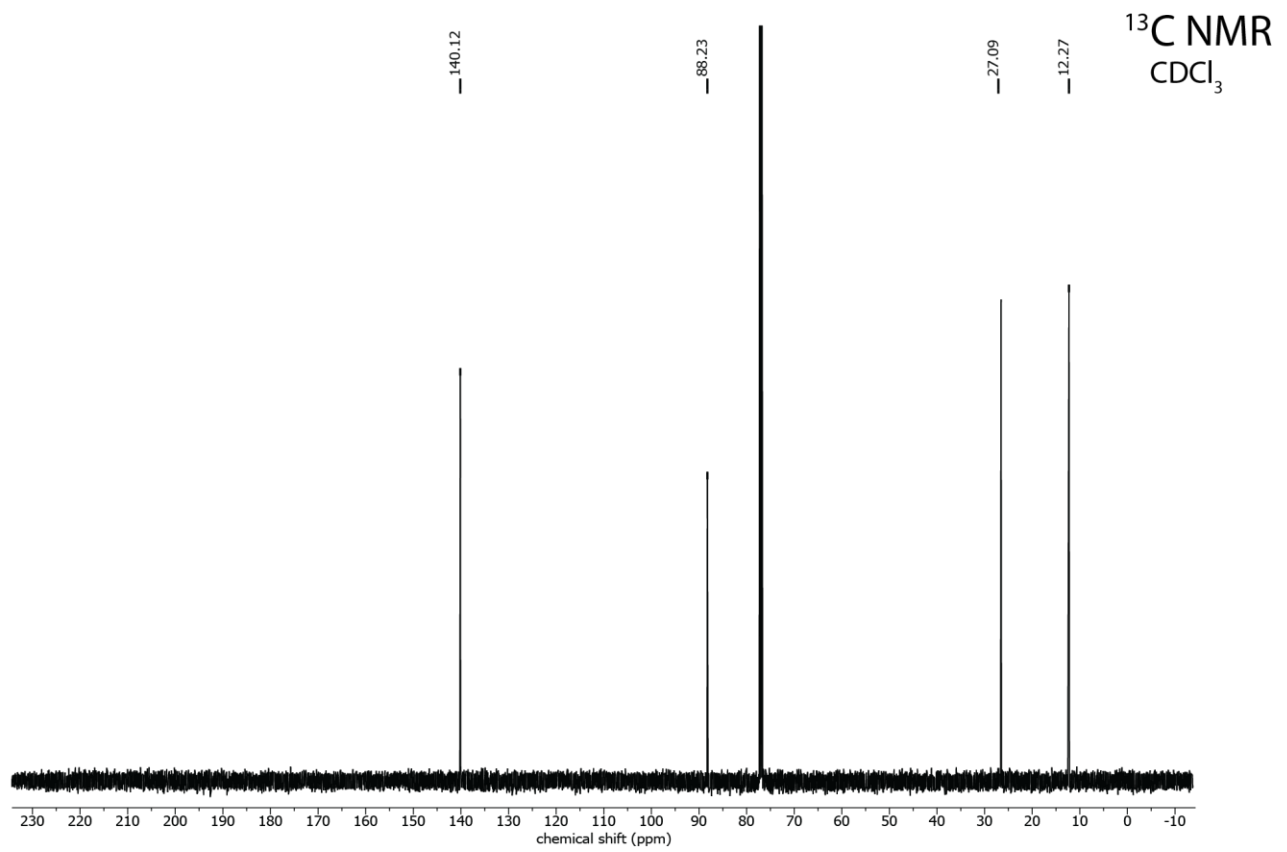
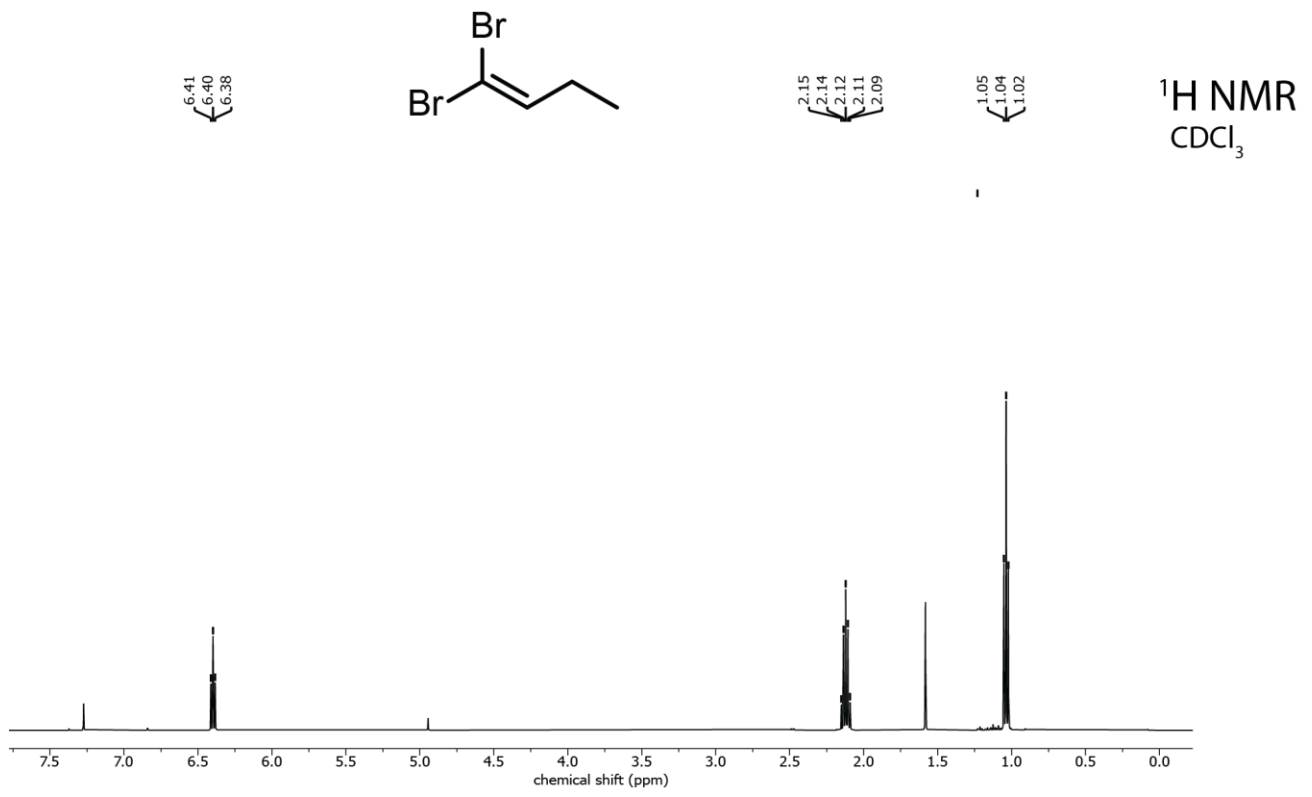


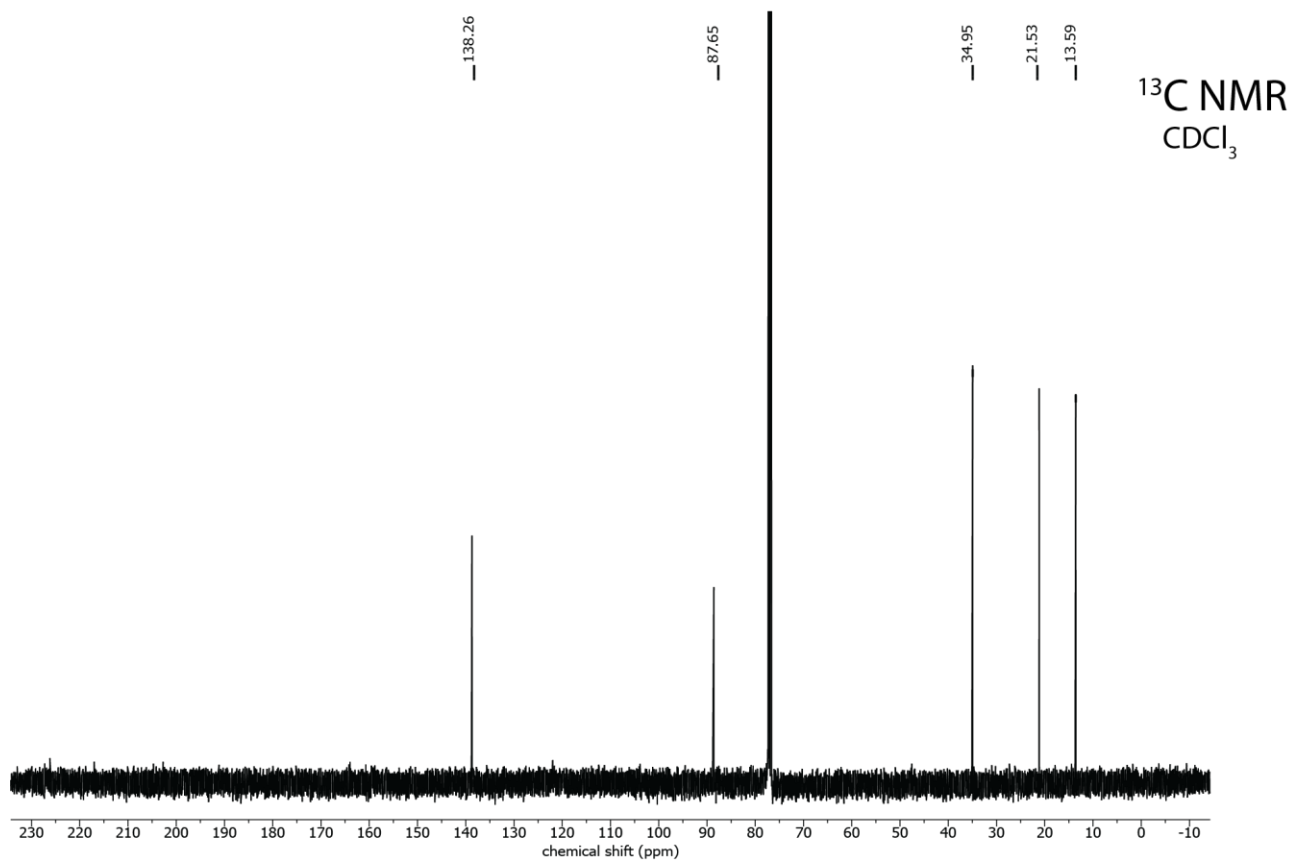
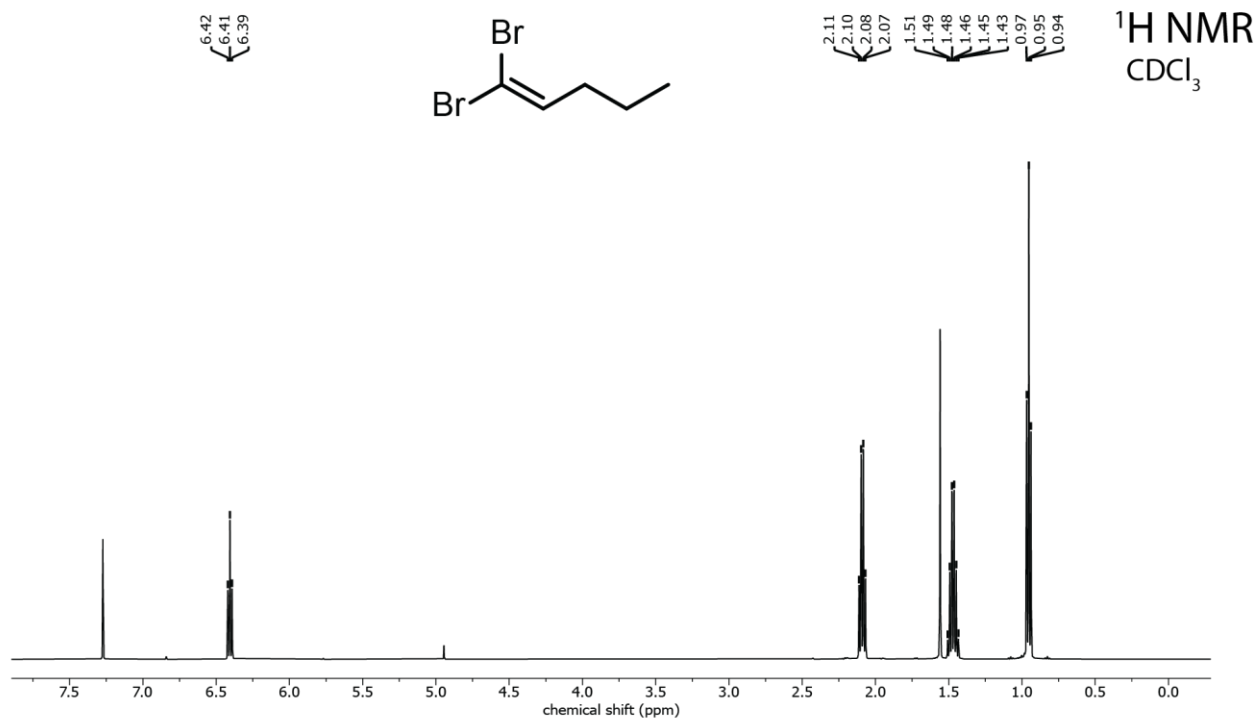
negligible starting material

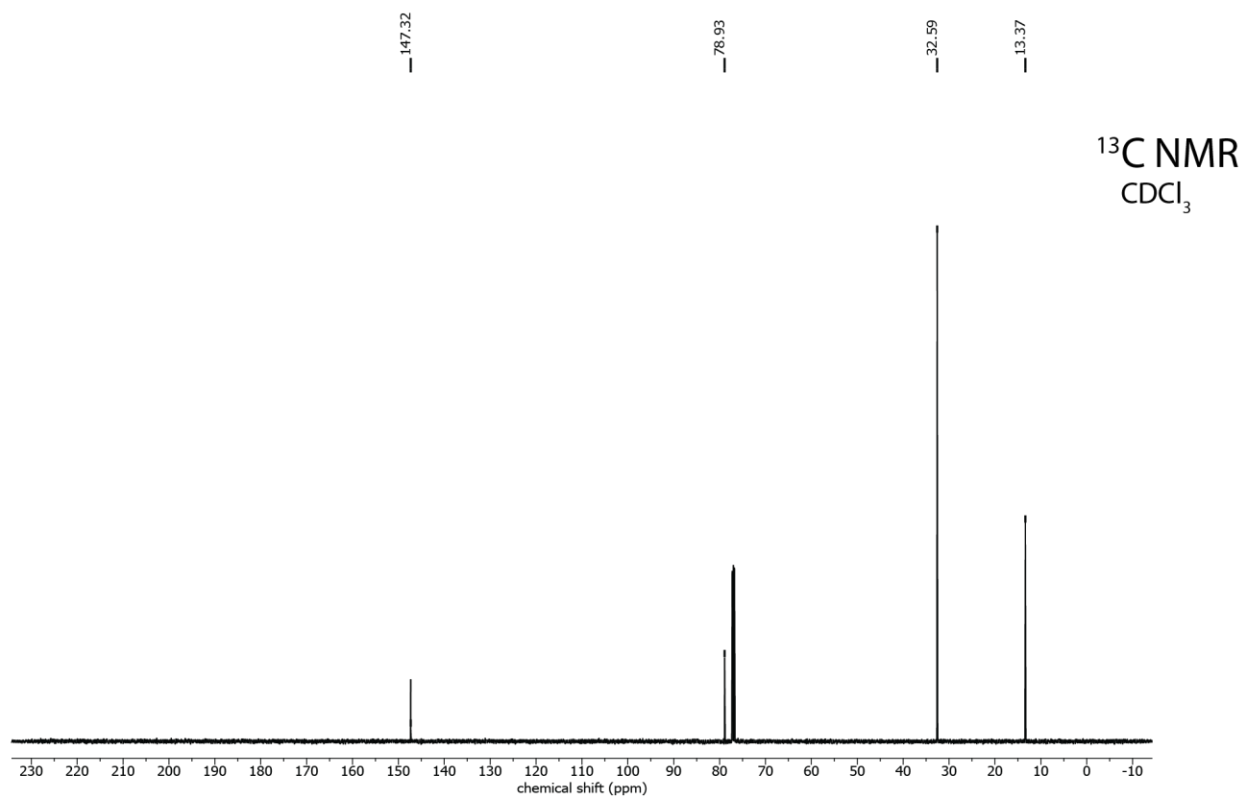
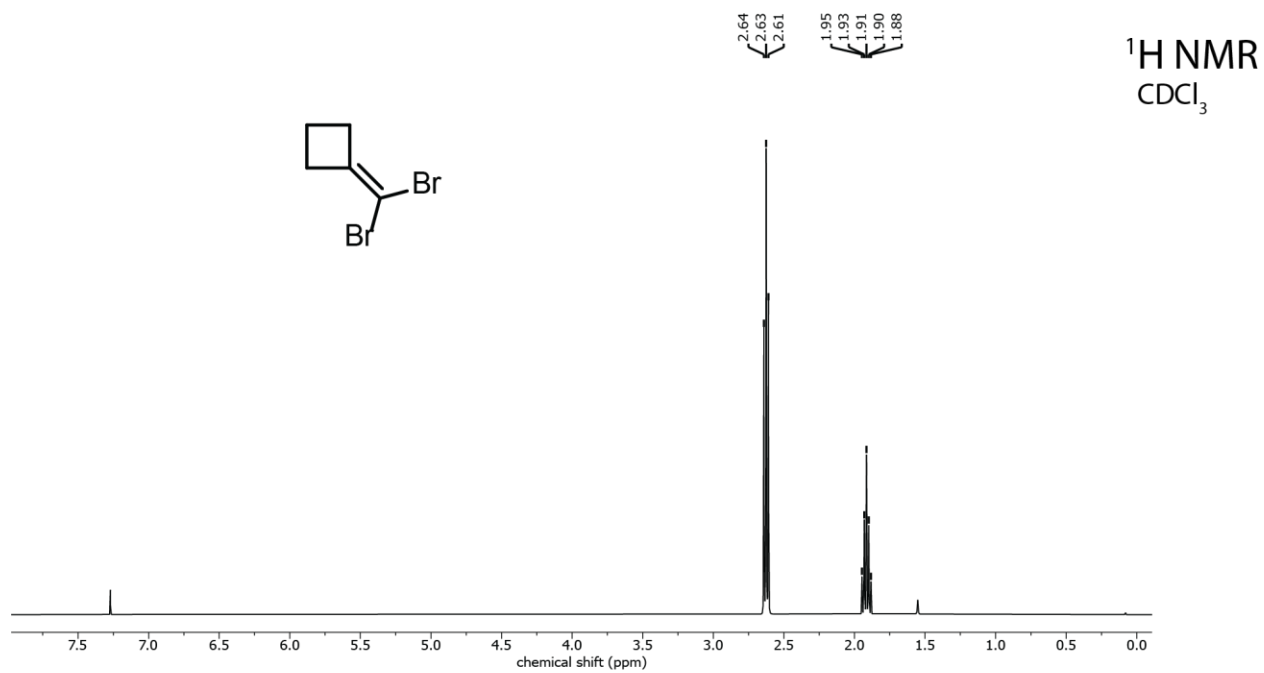


A.12. Solution ^1H and ^{13}C NMR of purified organic products

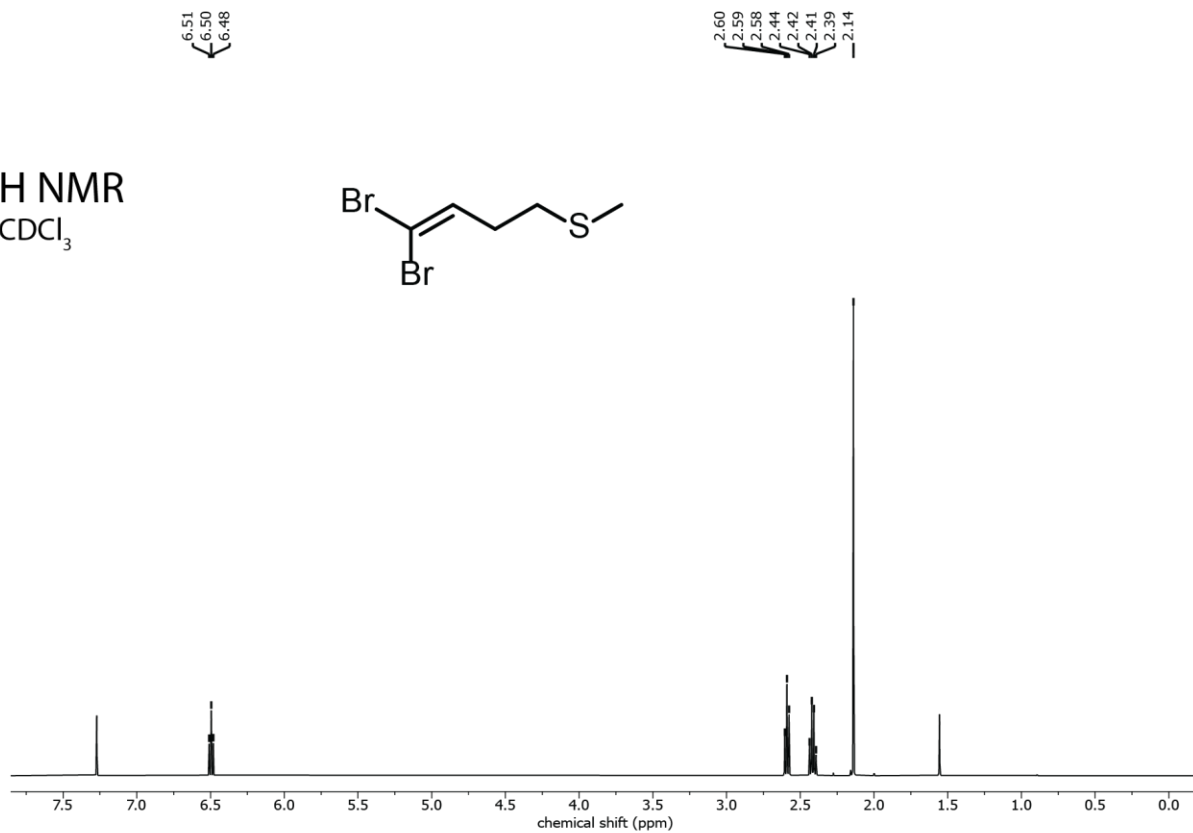
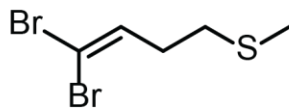




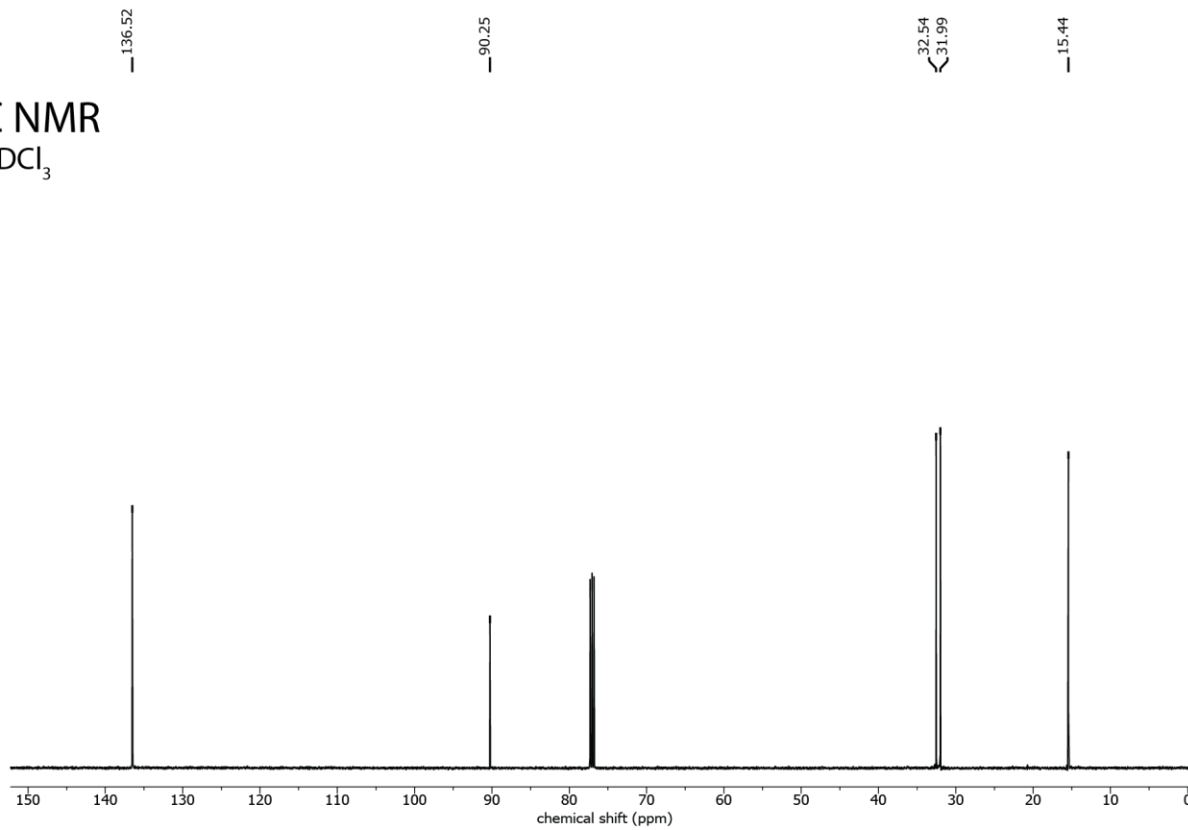




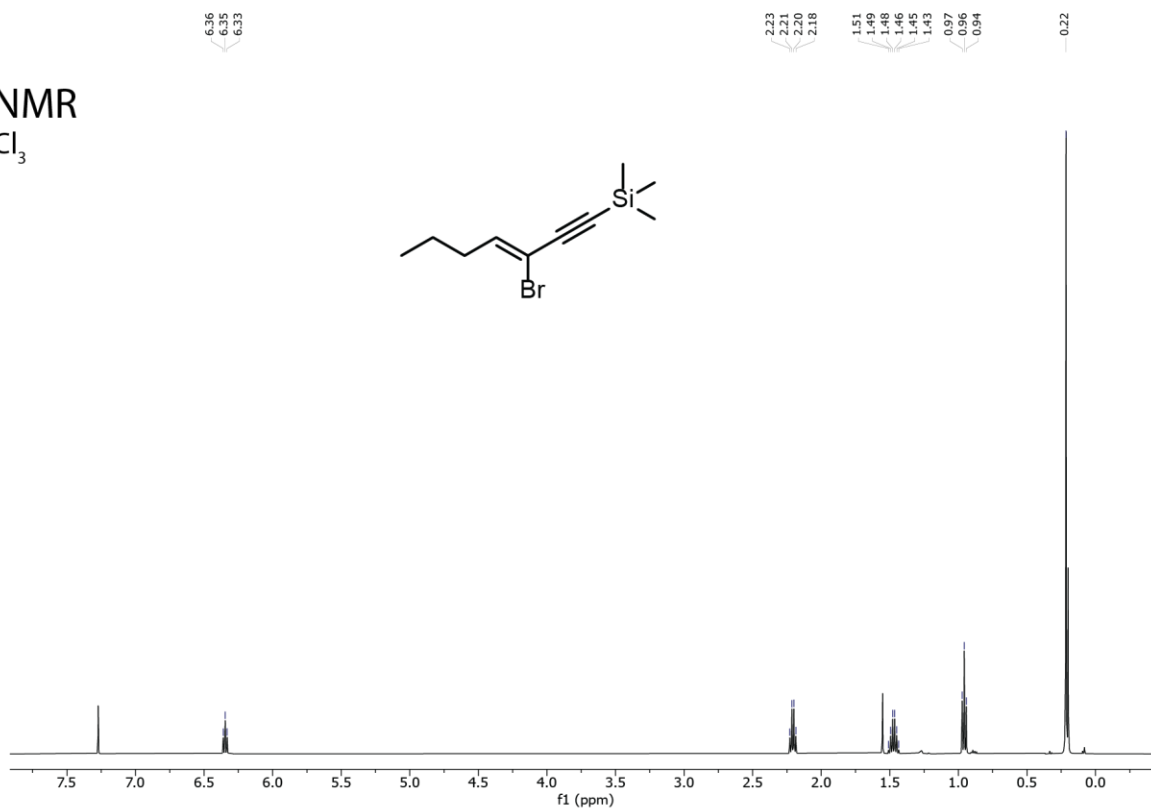
^1H NMR
 CDCl_3



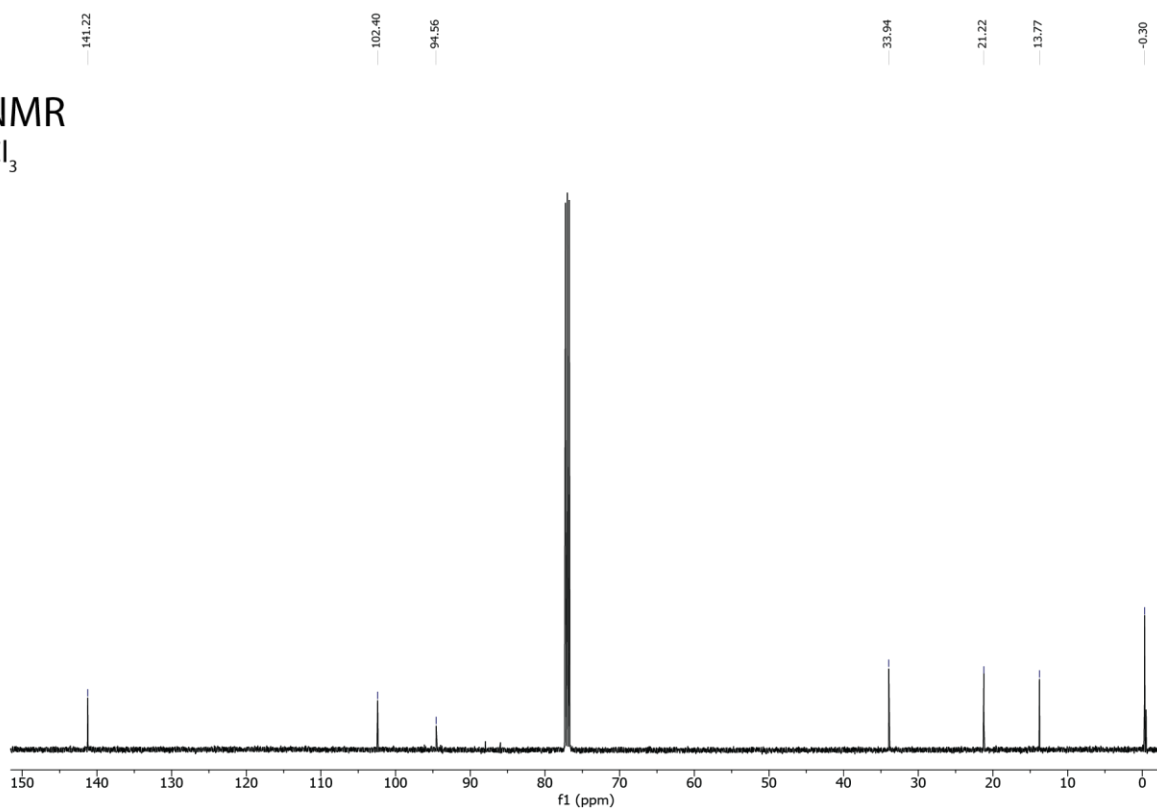
^{13}C NMR
 CDCl_3



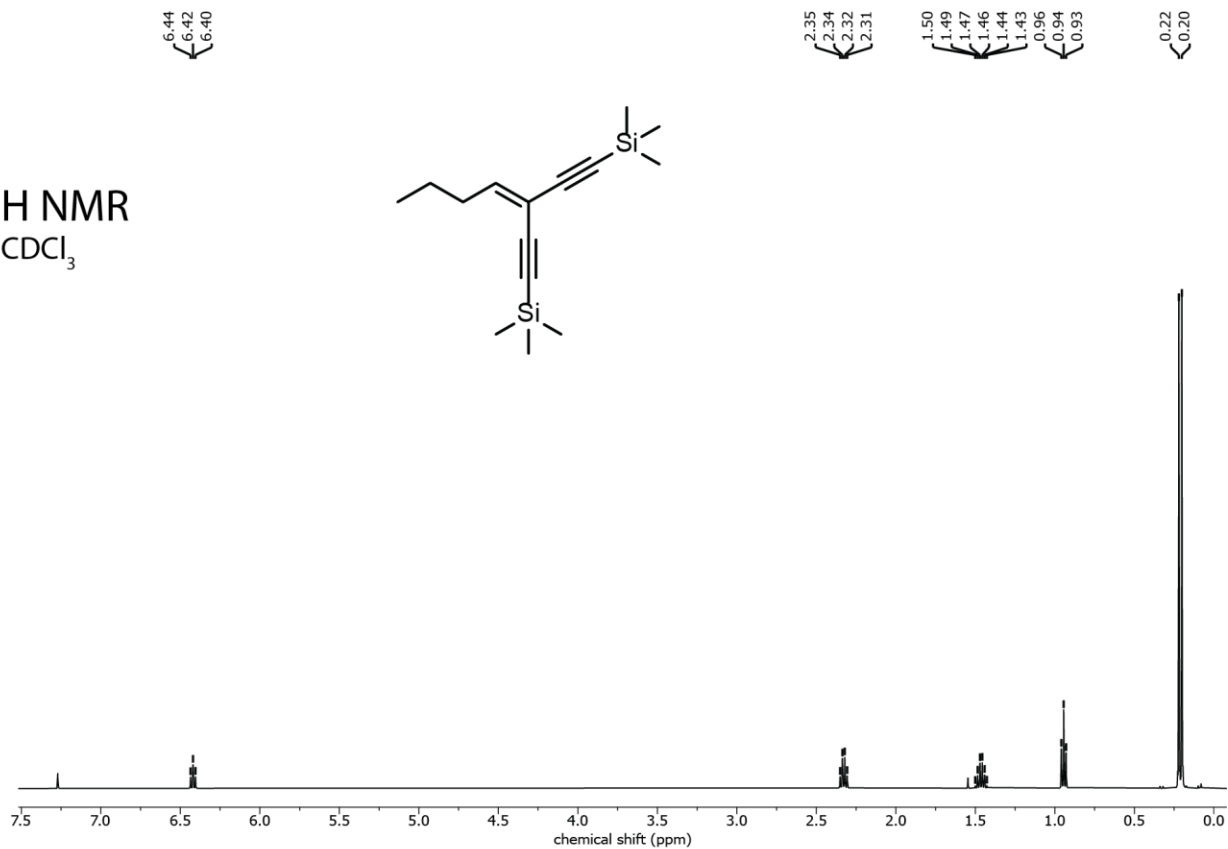
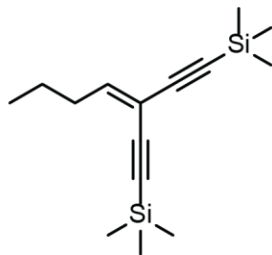
¹H NMR
CDCl₃



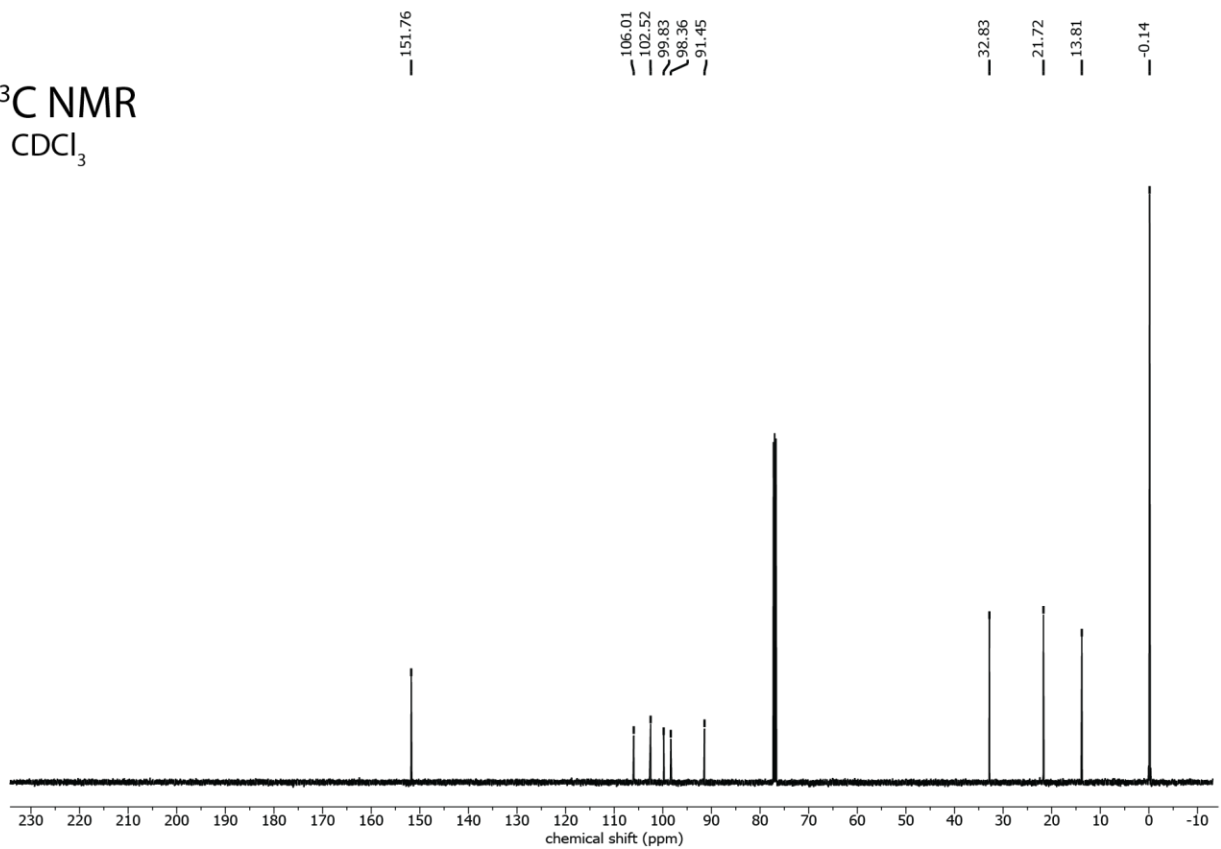
¹³C NMR
CDCl₃



^1H NMR
 CDCl_3



^{13}C NMR
 CDCl_3



A.13. References

1. P. Wolkoff, *Can. J. Chem* **1975**, *53*, 1333-1335.
2. J. Uenishi, K. Matsui, H. Ohmiya, *J. Organomet. Chem.* **2002**, *653*, 141-149.
3. R. Appel, W. Morbach, *Synthesis* **1977**, *10*, 699-700.
4. Frisch, M. J. *et. al.*, *Gaussian 16*, Revision C.01, Gaussian Inc., Wallingford, CT, **2016**.
5. a) A. D. Becke, *Phys. Rev.* **1993**, *98*, 5648-5652; b) C. Lee, W. Yang, R. G. Parr, *Phys. Rev. B* **1988**, *37*, 785-789.
6. B. P. Pritchard, D. Altarawy, B. Didier, T. D. Gibson, T. L. Windus, *J. Chem. Inf. Model* **2019**, *59*, 4814-4820.
7. K. Momma, F. Izum, *J. Appl. Cryst.* **2011**, *44*, 1271-1276.
8. G. M. Sheldrick, *Acta Cryst.* **2015**, *A71*, 3-8.
9. G. M. Sheldrick, *Acta Cryst.* **2015**, *C71*, 3-8.
10. A. L. Spek, *Acta Cryst.* **2015**, *C71*, 9-18.

Appendix B: *Ab Initio* metal-organic framework crystal structure prediction reveals elusive and functional copper(II) imidazolate frameworks

B.1. Materials

2-methylimidazole (**HMeIm**) (99%) was obtained from Sigma Aldrich. Copper (II) sulfate heptahydrate ($\geq 99\%$) was obtained from American Chemicals Ltd. Aqueous ammonia (28%) and methanol (99.8%) were obtained from Fischer Chemical. Acetone ($\geq 99.5\%$) was obtained from Caledon Chemicals. Sodium hydroxide was obtained from ACP Chemicals. All chemicals listed above were used as supplied without further purification. 2-vinylimidazole (**HVIm**) and 2-ethynylimidazole (**HAIIm**) were prepared according to previous reports.^{1,2} $[\text{Cu}(\text{NH}_3)_4]\text{SO}_4 \cdot \text{H}_2\text{O}$ was prepared according to previous reports.³

B.2. Synthetic Methods

B.2.1. Synthesis of single crystals of *dia*-Cu(VIm)₂

100 mg of copper(II) sulfate heptahydrate was dissolved in 10 mL of water, and 1 mL of aqueous ammonia (28%) was added to form a dark blue solution. To this was added 70 mg of **HVIm**, which was dissolved by sonication to yield a clear solution. After letting this mixture sit, capped, for 15 minutes, small dark blue crystals appeared amongst a large amount of brown impurity. The blue crystals can be separated by hand, under an optical microscope, for scXRD analysis.

B.2.2. Synthesis of single crystals of *dia*-Cu(AIm)₂

25 mg of copper (II) sulfate heptahydrate is dissolved in 10 mL of water, and 1 mL of aqueous ammonia (28%) was added to form a dark blue solution. A solution of 10 mg of **HAIIm** dissolved in a mixture of 5 mL of water and 1 mL aqueous ammonia (28%) is added dropwise to the copper solution over the course of 5 minutes, with gentle stirring. A fine powder forms during this addition, and this precipitation proceeds further without stirring for another 2 hours. Examination of this precipitate under an optical microscope shows the presence of a small amount of deep-

purple single crystals among the large amount of dark brown impurity. These crystals can be separated by hand for scXRD analysis.

B.2.3. Synthesis of single crystals of *dia*-Cu(MeIm)₂

200 mg of copper(II) sulfate pentahydrate is added to 10 ml of water, and 3 ml of aqueous ammonia (28%) is added to form a dark blue solution. 200 mg of HMeIm is added as a solid and is dissolved by stirring. The mixture is heated gently for about 5 minutes until bubbles of ammonia evolve and a solid precipitate appears. This solid is removed by filtration with the mixture still hot, and the filtrate is collected and allowed to cool, capped, to room temperature. Crystal form over the course of the next 6 hours which are collected by pipette and separated by hand under an optical microscope for scXRD analysis.

B.2.4. Synthesis of bulk powder *dia*-Cu(VIm)₂

1 mmol (245 mg) of Cu(NH₃)₄(H₂O)(SO₄), 2.1 mmol HVIm (197.4 mg) and 500 μL water are placed in an 8 mL plastic vial and subject to resonant acoustic mixing (RAM) at 80 g for 20 minutes at room temperature. The resulting powder is stirred briefly in 10 mL of water, isolated by centrifugation, then stirred briefly in 10 mL of acetone. After isolation by centrifugation, the material is dried overnight at 80 °C under vacuum.

B.2.5. Synthesis of bulk powder *α*-Cu(AIm)₂

100 mg of copper(II) sulfate heptahydrate is dissolved in 10 mL of water and 1 mL of aqueous ammonia (28%) is added to form a dark blue solution. 64 mg of HAIm is added as a solid, and immediately a burgundy precipitate forms. This mixture is allowed to stir for 10 minutes, then the burgundy precipitate is isolated by centrifugation, then stirred briefly in 10 mL of water, and again isolated by filtration. After stirring briefly in 20 mL of acetone, the product is collected by centrifugation and dried overnight at 80 °C under vacuum.

B.2.6. Synthesis of bulk powder *β*-Cu(AIm)₂

60 mg of *dia*-Cu(Aim)₂ and 30 uL of methanol are milled for 20 minutes in a 15 mL zirconia milling jar with one 1.3g zirconia milling ball at 25 Hz. The powder is collected, stirred briefly in methanol, filtered, and dried under high vacuum at room temperature overnight.

B.2.7. Synthesis of bulk powder *dia*-Cu(MeIm)₂

1 g of copper(II) sulfate heptahydrate is dissolved in 25 ml of water and 15 mL of aqueous ammonia (28%) is added to form a dark blue solution. A solution of 1.5 g of HMeIm in 30 mL of water is added to this solution, and the mixture is stirred for 5 minutes. Under continued vigorous stirring, 2 mL of 25 % NaOH (25g NaOH in 75 mL DI Water) is added dropwise over the course of 10 minutes, causing the precipitation of a green powder. After 10 minutes of additional stirring, the powder is collected by filtration and is rinsed on the filter with 10 mL of dilute (~8%) aqueous ammonia. This powder is collected and washed in 20 mL of acetone before evacuation under vacuum at 80 °C.

B.3. Crystallographic information

Single crystal X-ray diffraction (scXRD) data were measured on a Bruker D8 Venture diffractometer equipped with a Photon 200 area detector, and *I μ S* microfocus X-ray source (Bruker AXS, CuK α source). Measurements were carried out at 150(2) K for Cu(VIm)₂, and 298(2) K for Cu(MeIm)₂ and α -Cu(MeIm)₂. Crystals were coated with a thin layer of paratone oil before mounting on the diffractometer. Structural solutions were carried out using the SHELXTL package.⁴ The parameters were refined for all data by full-matrix-least-squares refinement of F² using SHELXL.⁵ All non-hydrogen atoms were refined with anisotropic thermal parameters. All hydrogen atoms were constrained to ride on their carrier atom.

Table B.3.1. Crystallographic data for scXRD structures.

Material	Cu(MeIm) ₂	Cu(VIm) ₂	α-Cu(AIm) ₂
Empirical formula	C ₈ H ₁₀ CuN ₄	C ₁₀ H ₁₀ CuN ₄	C ₁₀ H ₆ CuN ₄
Formula weight	225.74	249.76	245.73
Temperature (K)	298(2)	150(2)	298(2)
Crystal system	orthorhombic	tetragonal	tetragonal
Space group	Fdd2	I4 ₁	I4 ₁
<i>a</i> (Å)	8.0097(5)	7.4615(10)	7.7149(4)
<i>b</i> (Å)	15.3152(9)	7.4615(10)	7.7149(4)
<i>c</i> (Å)	16.6204(9)	18.614(3)	17.8648(12)
α (°)	90	90	90
β (°)	90	90	90
γ (°)	90	90	90
<i>V</i> (Å ³)	2038.8(2)	1036.3(3)	1063.31(13)
<i>Z</i>	8	4	4
ρ _{calc} (g/cm ³)	1.471	1.601	1.535
μ (mm ⁻¹)	2.703	2.728	2.658
<i>F</i> (000)	920.0	508.0	492.0
2θ range for data collection (°)	13.566 to 144.628	16.804 to 144.888	12.498 to 144.598
Index ranges	-9 ≤ <i>h</i> ≤ 9, -18 ≤ <i>k</i> ≤ 18, -20 ≤ <i>l</i> ≤ 20	-8 ≤ <i>h</i> ≤ 9, -9 ≤ <i>k</i> ≤ 9, -22 ≤ <i>l</i> ≤ 22	-9 ≤ <i>h</i> ≤ 8, -9 ≤ <i>k</i> ≤ 5, -17 ≤ <i>l</i> ≤ 21
Reflections collected	5894	7731	4371
Independent reflections	1000 [R _{int} = 0.0556, R _{sigma} = 0.0376]	1023 [R _{int} = 0.0388, R _{sigma} = 0.0241]	969 [R _{int} = 0.1533, R _{sigma} = 0.1042]
Data/restraints/parameters	1000/1/62	1023/1/69	969/55/70
<i>S</i>	0.936	1.009	0.956
Final R indexes [<i>I</i> ≥ 2σ (<i>I</i>)]	R ₁ = 0.0335, wR ₂ = 0.1060	R ₁ = 0.0208, wR ₂ = 0.0574	R ₁ = 0.0539, wR ₂ = 0.1129
Final R indexes [all data]	R ₁ = 0.0348, wR ₂ = 0.1076	R ₁ = 0.0214, wR ₂ = 0.0582	R ₁ = 0.1186, wR ₂ = 0.1544
Largest diff. peak/hole (e Å ⁻³)	0.31/-0.35	0.19/-0.22	0.32/-0.36

B.4. FTIR spectra of Cu-ZIFs

FTIR measurements were taken on a Bruker Vertex 70 FTIR spectrometer, using the Bruker Platinum ATR accessory.

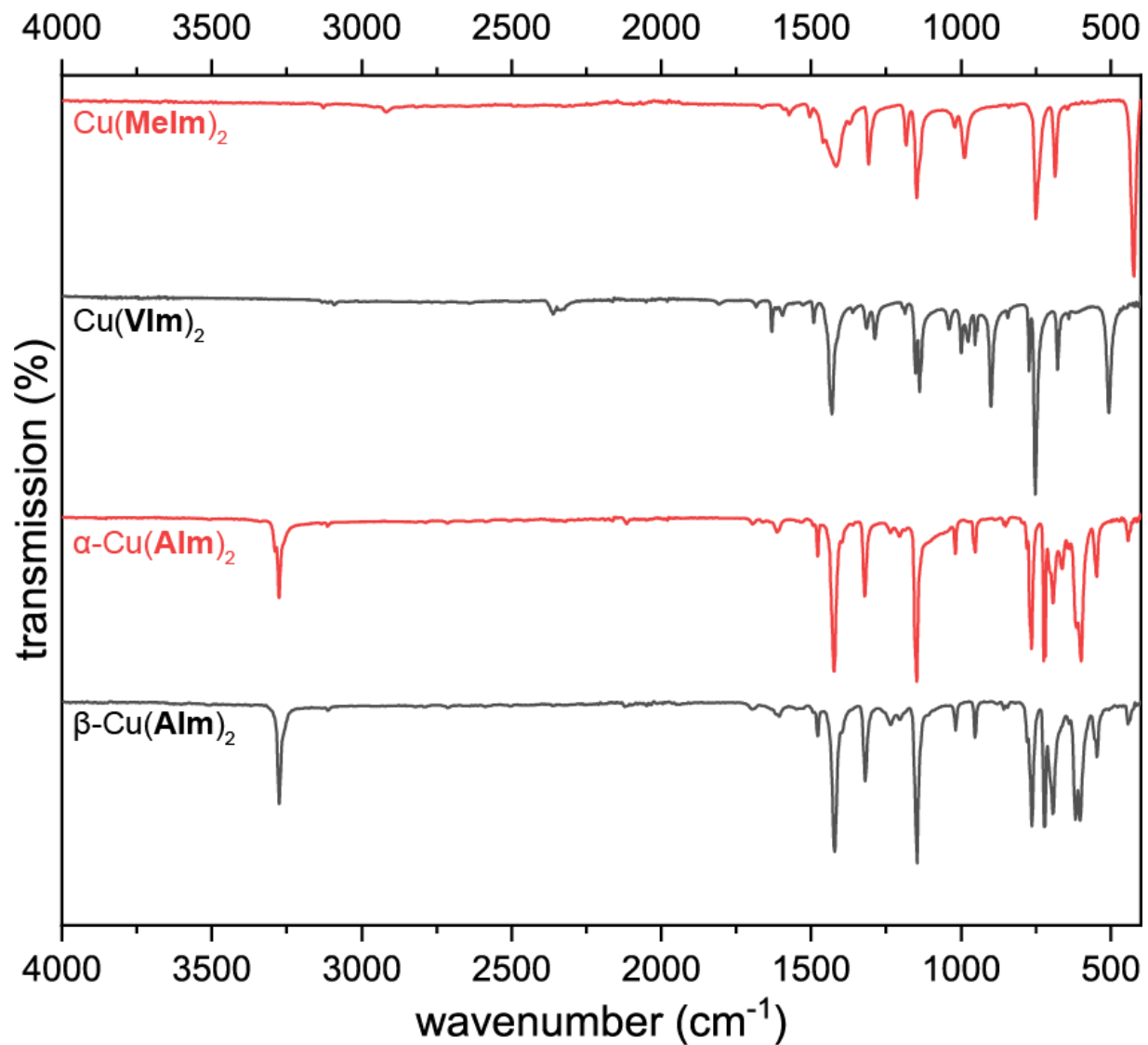


Fig B.4.1. FTIR Spectra of copper(II)-based ZIFs.

B.5. ^1H NMR Spectra of acid-digested $\text{Cu}(\text{AIm})_2$ ZIFs

^1H NMR spectra were collected on a Varian Inova 500 MHz spectrometer operating at 500 MHz for ^1H . ZIF samples were dissolved in concentrated deuterium chloride (37 %, Sigma Aldrich) which was then diluted with D_2O (Sigma Aldrich) before data collection.

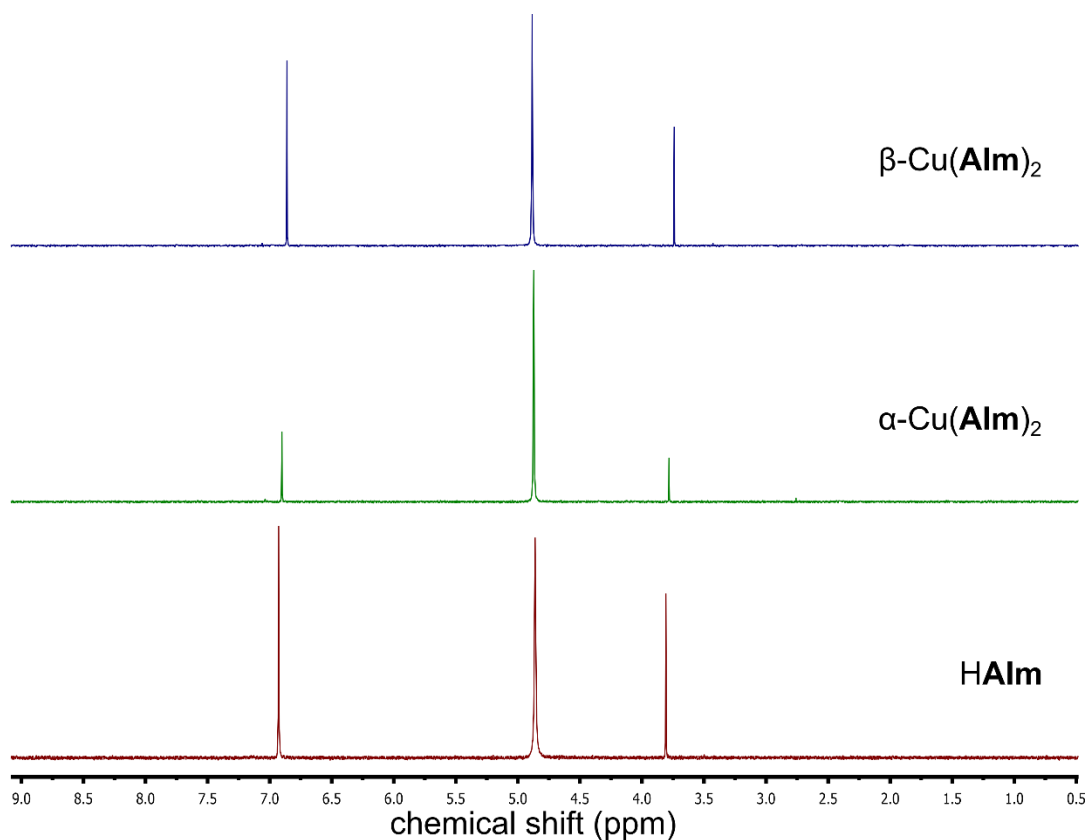


Fig B.5.1. ^1H NMR Analysis of $\text{Cu}(\text{AIm})_2$ ZIFs. Proton NMR of ZIFs digested in dilute DCl in D_2O shows that the AIm linker is unchanged after milling $\alpha\text{-Cu}(\text{AIm})_2$ to produce $\beta\text{-Cu}(\text{AIm})_2$.

B.6. TGA/DSC Analysis of Cu-ZIFs

Thermogravimetric analysis (TGA) and differential scanning calorimetry (DSC) data were collected simultaneously using a Mettler-Toledo TGA/DSC 1 instrument. Each sample (3 – 10 mg) was loaded into a 70 μL alumina pan and heated from 30 C to 800 C under a stream of air (65 mL min^{-1}).

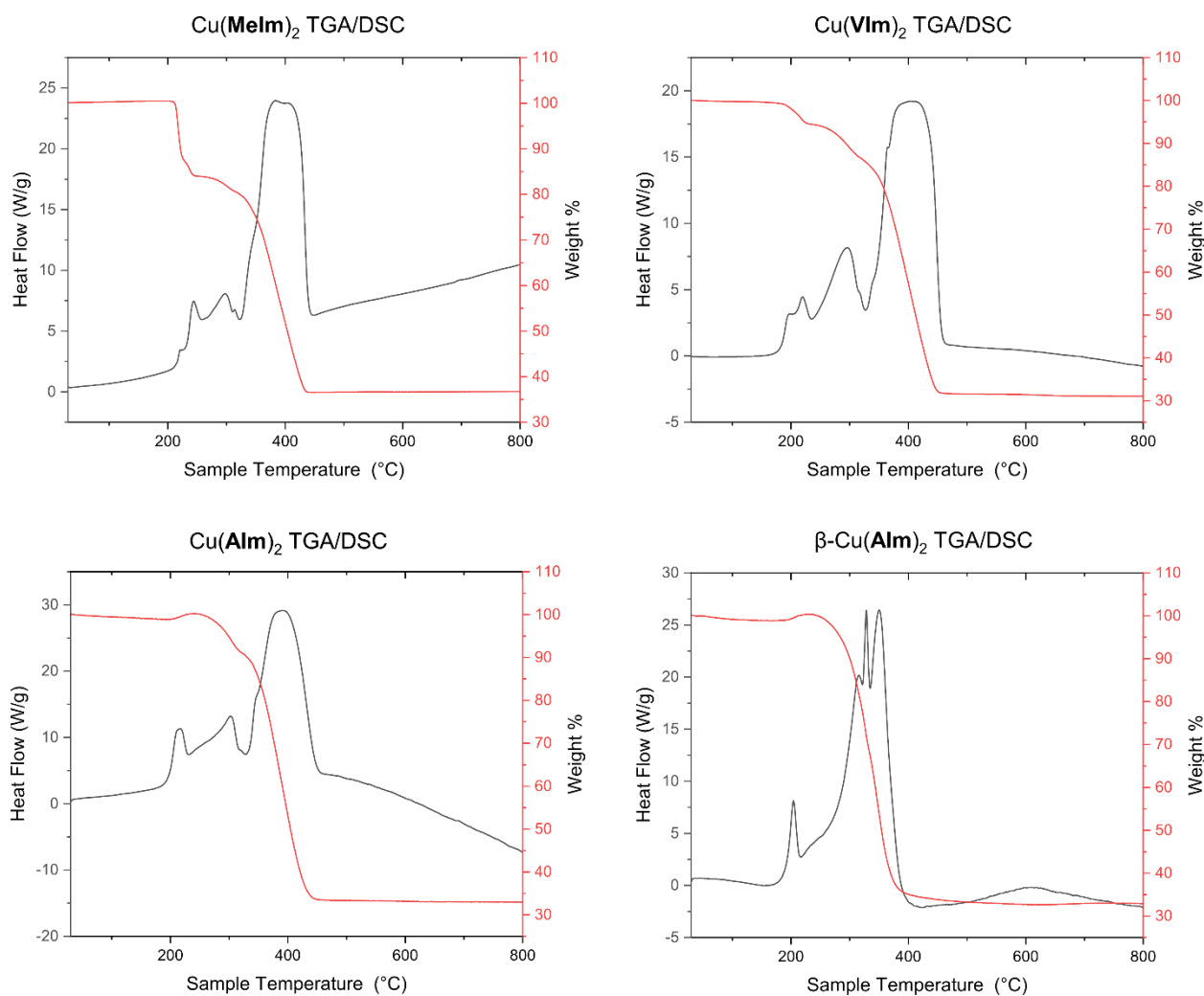
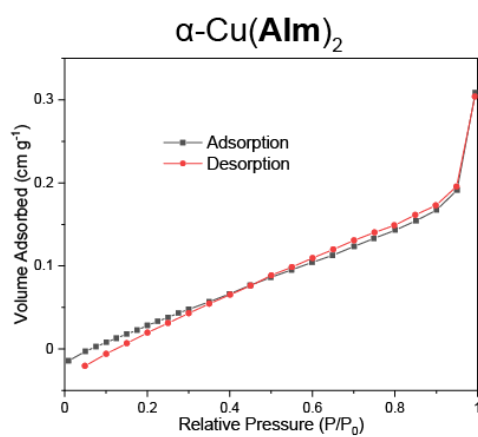
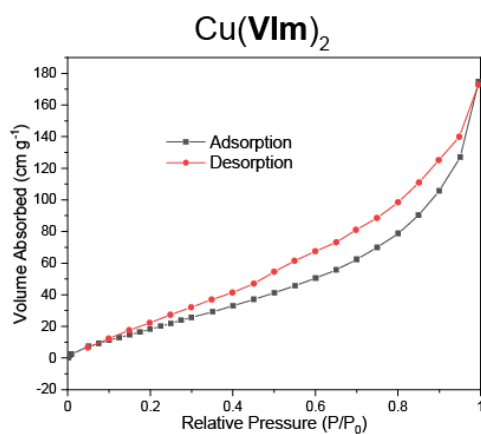
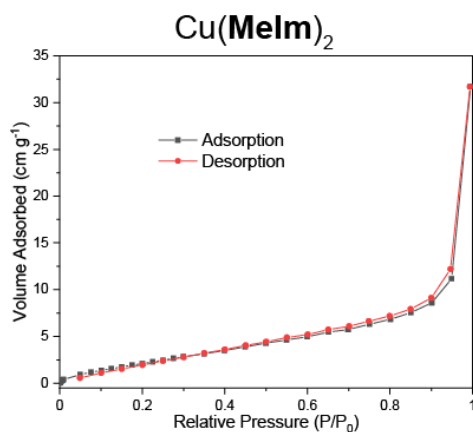


Fig B.6.1. TGA/DSC Analysis of Cu-ZIFs. Thermogravimetric and differential scanning calorimetry analysis of Cu(VIm)₂ (theoretical residue: 31.8% experimental: 31.3%), α -Cu(AIm)₂ (theoretical residue: 32.4% experimental: 33.2%), β -Cu(AIm)₂ (theoretical residue: 32.4% experimental: 32.5%) and Cu(MeIm)₂ (theoretical residue: 35.2% experimental: 36.6%)

B.7. N₂ Adsorption Data



Material	Multipoint BET surface area
Cu(MeIm) ₂	11 m ² g ⁻¹
Cu(VIm) ₂	102 m ² g ⁻¹
α-Cu(AIm) ₂	0.4 m ² g ⁻¹

B.8. PXRD analysis for Cu-ZIFs

Powder x-ray diffraction (PXRD) data was collected using a Bruker D2 Phaser diffractometer equipped with a Lynxeye 1D detector using Cu K α x-ray radiation which was Ni-filtered.

S.8.1 PXRD Analysis of Impact Tests for Cu-ZIFs

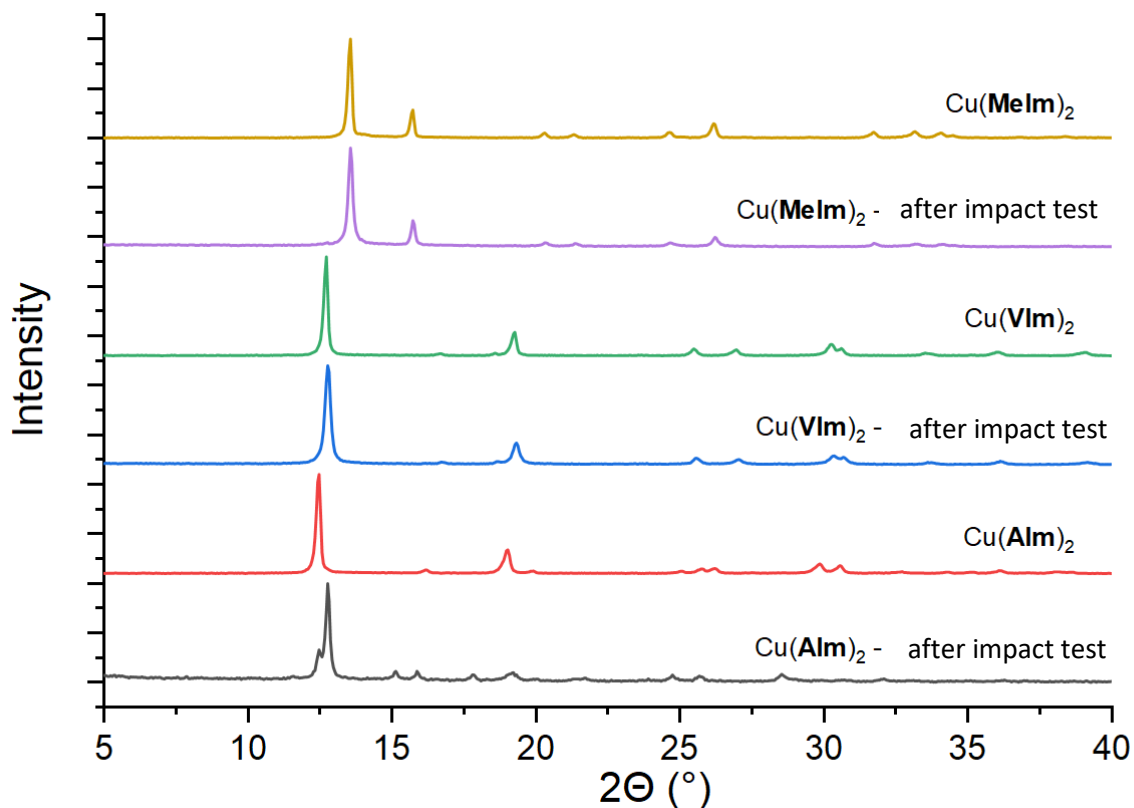


Fig B.8.1. PXRD Patterns for Cu-ZIFs after impact-testing. Impact sensitivity was probed using a hammer drop test, where a steel cylinder of 2.7 kg weight is dropped from a height of 2.1 m onto approximately 25 mg of sample, representing a 50 J impact.

B.8.2. PXRD Analysis of $\text{Cu}(\text{VIm})_2$ Synthesis

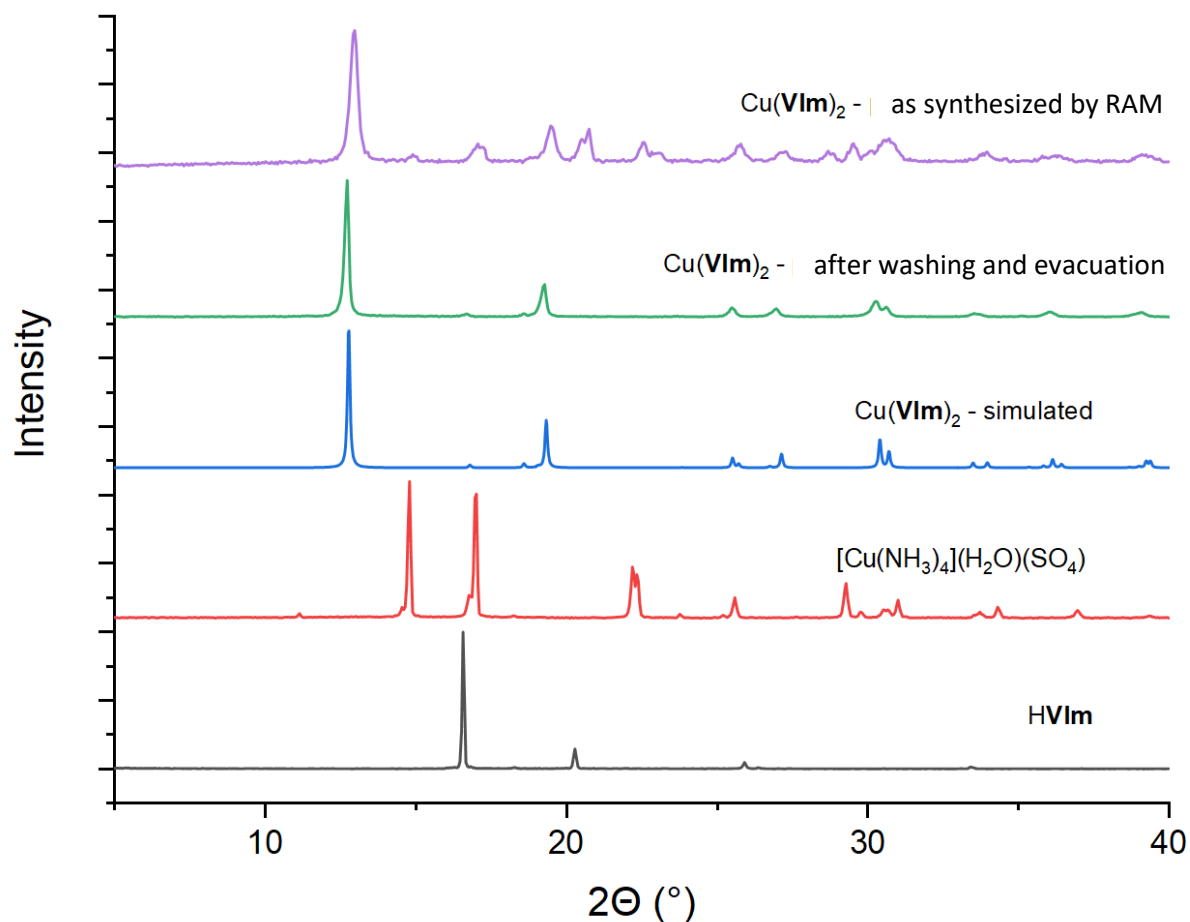


Fig B.8.2. PXRD Patterns for $\text{Cu}(\text{VIm})_2$ synthesis. Microcrystalline $\text{Cu}(\text{VIm})_2$ is made by resonant acoustic mixing, then washed and evacuated. The PXRD pattern of the bulk materials matches that simulated from the herein reported scXRD structure.

B.8.3 PXRD Analysis of Solution Synthesis of $\text{Cu}(\text{MeIm})_2$ and $\alpha\text{-Cu}(\text{AIm})_2$

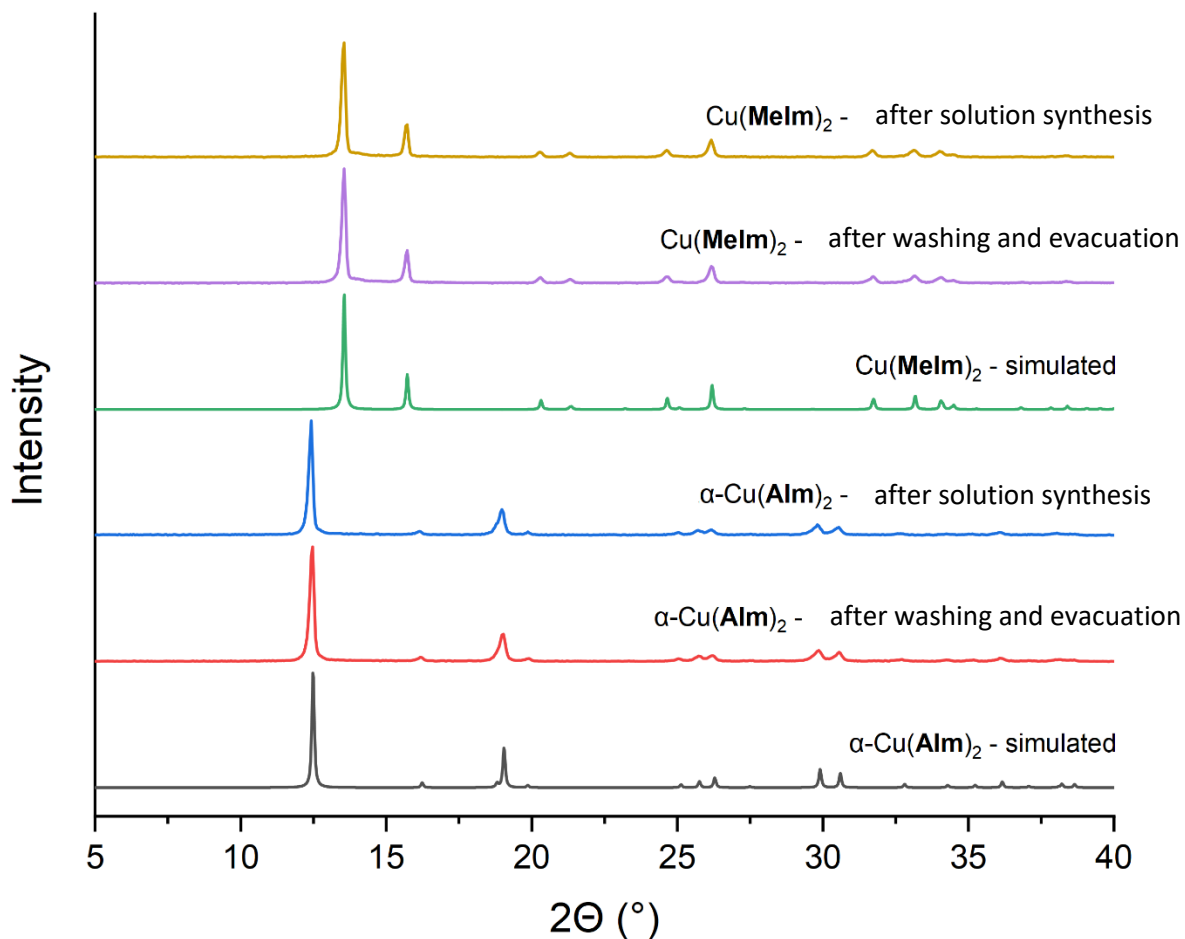


Fig B.8.3. PXRD Patterns for solution synthesis of $\text{Cu}(\text{MeIm})_2$ and $\text{Cu}(\text{AIm})_2$. Microcrystalline $\text{Cu}(\text{AIm})_2$ and $\text{Cu}(\text{MeIm})_2$ are precipitated from solution before washing and evacuation. The PXRD patterns of the powders match those simulated from the herein reported scXRD structures.

B.9. Crystal structure prediction methods

The CSP method used in this work is based on our previously reported method of combining the *ab initio* random structure searching method (AIRSS)⁷ algorithm with the Wyckoff Alignment of Molecules (WAM)⁸ method. Random trial crystal structures were generated using AIRSS and WAM by placing the metal nodes and organic linkers randomly into the asymmetric unit of a given unit cell with a given symmetry. For each of the three systems Cu(**MeIm**)₂, Cu(**VIm**)₂ and Cu(**AIm**)₂, up to 1000, 2000, 3000 or 4000 structures were generated containing either 1, 2, 3, or 4 ZIF formula units (M(L)₂) per crystallographic primitive cell respectively. Geometry optimizations were performed using the plane-wave periodic DFT code CASTEP⁹ using the PBE functional with Grimme D2 dispersion correction. The plane-wave cutoff was set to 400 eV and the Brillouin zone was sampled with a 0.07 Å⁻¹ k-point grid. The ultrasoft set pseudopotentials were used from the internal QC5 library of CASTEP.

Initial optimized structures were ranked by overall lattice energy and duplicate structures were removed. Then, only the structures with energies up to 50 kJ mol⁻¹ above the structure with the global energy minimum were kept, and all higher-energy structures were discarded. These remaining structures were again geometry-optimized using the more sophisticated PBE functional with many body dispersion (MBD*) correction scheme. For this computation, the plane-wave cutoff was raised to 700 eV and the structures were then ranked again by energy and duplicates were removed. Final calculations of solvent-accessible volumes and packing coefficients for all predicted structures were performed using the PLATON¹⁰ software package.

B.10. SEM Images of Cu-ZIFs

SEM images were collected using a FEI Quanta 450 environmental Scanning Electron Microscope. Samples were sputter coated with a 4 nm layer of Pt before imaging.

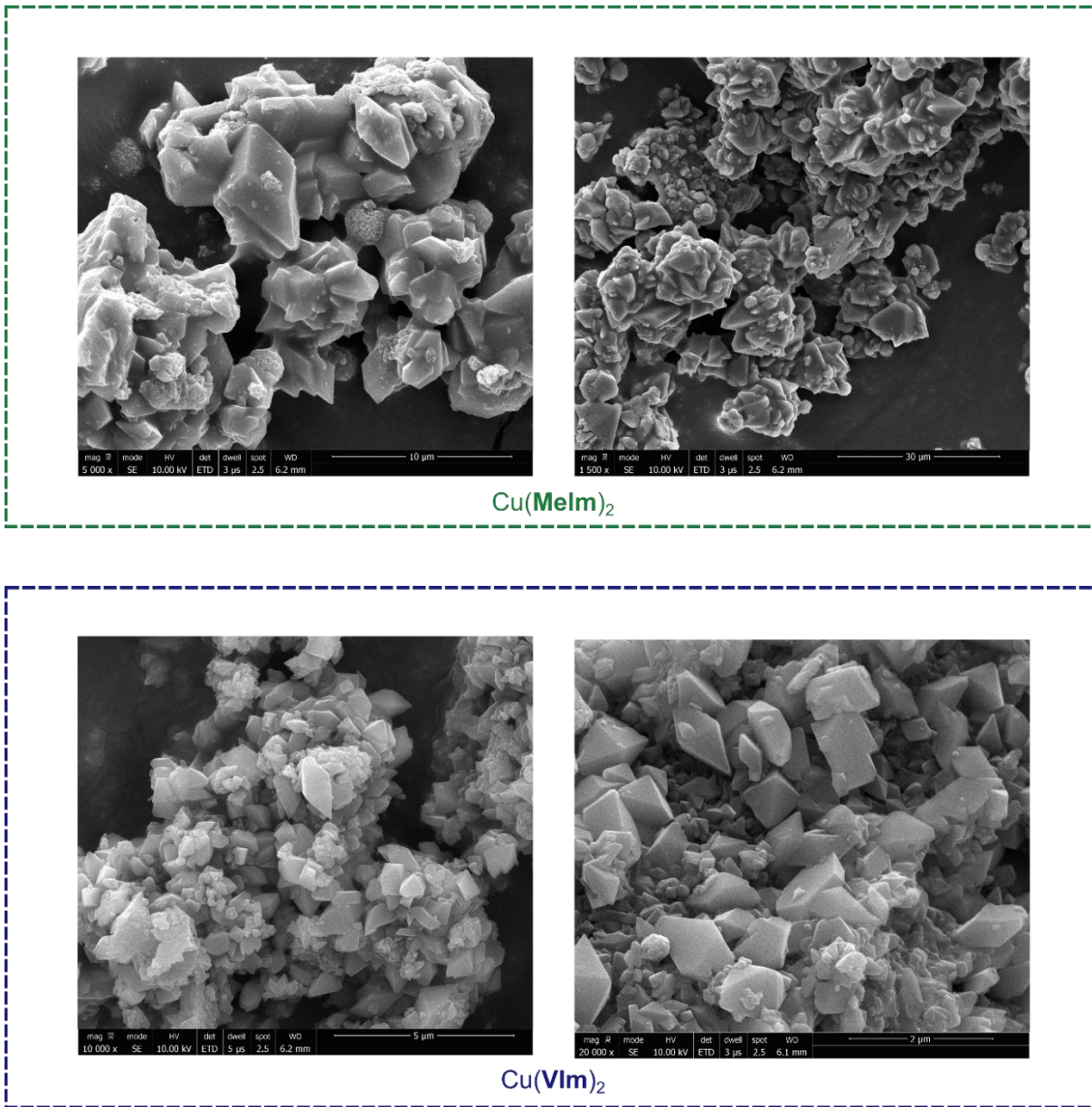


Figure B.10.1. SEM images of $\text{Cu}(\text{MeIm})_2$ and $\text{Cu}(\text{VIm})_2$.

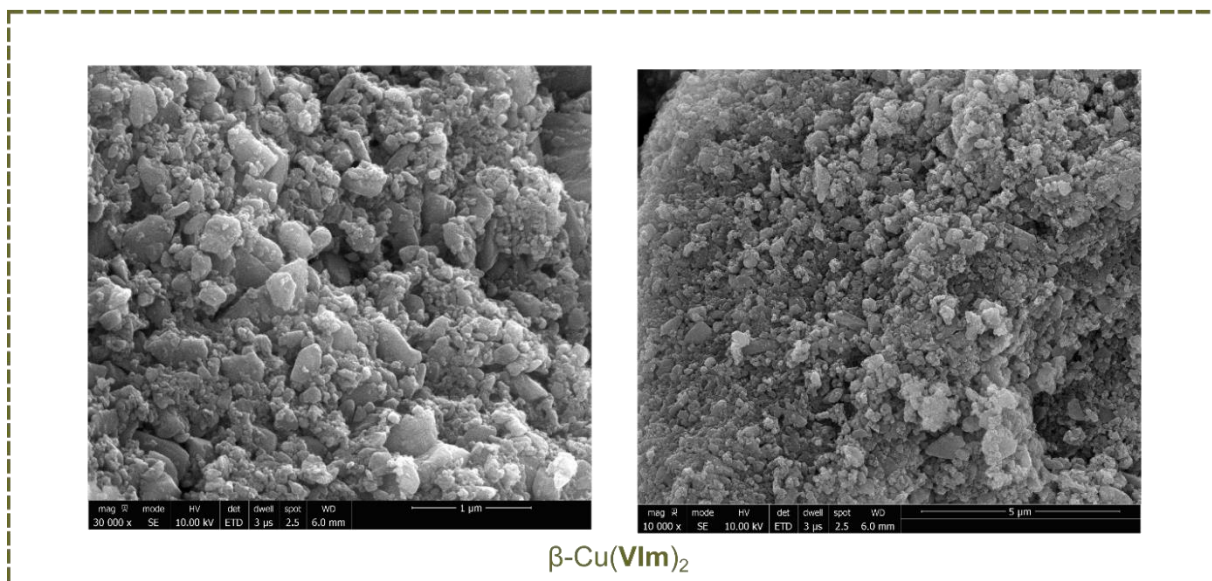
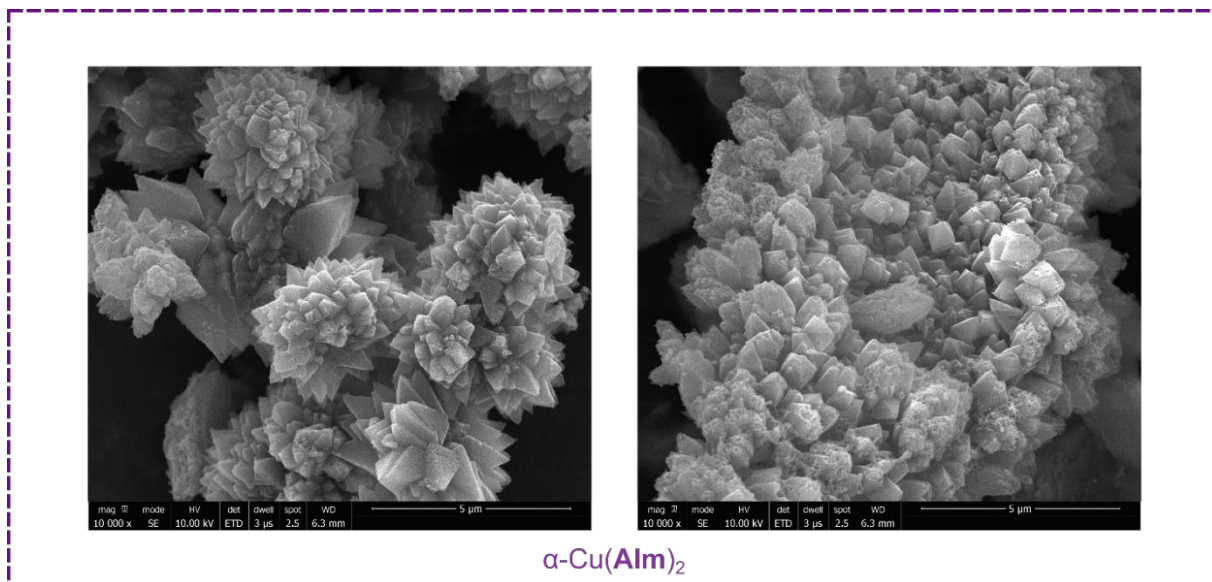


Figure B.10.2. SEM images of α -Cu(MeIm)₂ and β -Cu(VIm)₂.

B.11. Hypergolic Drop-Test Data for Cu-ZIFs

Hypergolic tests were performed using a standardized drop-test setup described previously.⁶ A 5 mg sample of Cu-ZIF is placed in a glass vial and a 10 μ L drop of white fuming nitric acid is released from a syringe 5 cm above the sample. A Redlake MotionPro Y4 high-speed camera collecting images at 1000 frames per second is used to determine the time between contact of the white fuming nitric acid with the sample and the first signs of ignition, the ignition delay (ID). This data is collected in triplicate to determine the ID with an associated standard deviation, in parentheses.

B.12. Structure solution from powder X-ray diffraction data

Powder X-ray diffraction data was used to solve the crystal structure of β -Cu(**AIM**)₂. Indexing of the pattern was accomplished using the program DICVOL06.¹¹ Space group determination, Pawley refinement, and simulated annealing structure solution were performed using the TOPAS Academic 6 software package.¹² The structure produced by simulated annealing was subject to Rietveld refinement against the experimental PXRD data. The resulting structure was subject to geometry optimization using CASTEP plane wave DFT code to produce the final crystal structure.

B.12. References

1. J. M. Marrett, C. Mottillo, S. Girard, C. W. Nickels, J.-L. Do, G. Dayaker, L. S. Germann, R. E. Dinnebier, A. J. Howarth, O. K. Farha, T. Frišćić, C. J. Li, *Cryst. Growth Des.* **2018**, *18*, 3222-3228.
2. O. Dirat, A. Clipson, J. M. Elliot, S. Garrett, A. B. Jones, M. Reader, D. Shaw, *Tetrahedron Lett.* **2006**, *47*, 1729-1731.
3. F. Mazzi, *Acta Cryst.* **1955**, *8*, 137.
4. G. M. Sheldrick, *Acta Cryst. Sect. A* **2015**, *71*, 3-8.
5. G. M. Sheldrick, *Acta Cryst. Sect. C* **2015**, *71*, 3-8.
6. H. M. Titi, J. M. Marrett, G. Dayaker, M. Arhangelskis, C. Mottillo, A. J. Morris, G. P. Rachiero, T. Frišćić, R. D. Rogers, *Sci. Adv.* **2019**, *5*, eaav9004.
7. C. J. Pickard, R. J. Needs, *J. Phys. Condens. Matter* **2011**, *23*, 053201.
8. J. P. Darby, M. Arhangelskis, A. D. Katsenis, J. M. Marrett, T. Frišćić, A. J. Morris, *Chem. Mater.* **2020**, *32*, 5835-5844.
9. S. J. Clark, M. D. Segall, C. J. Pickard, P. J. Hasnip, M. I. J. Probert, K. Refson, M. C. Payne, *Z. Kristallogr. – Cryst. Mater.* **2005**, *220*, 567-570.
10. L. Spek, *Acta Cryst.* **2009**, *D65*, 148-155.
11. A. Boulton, D. Louer, *J. Appl. Cryst.* **2004**, *37*, 724-731.
12. A. Coelho, Coelho Software: Brisbane, Australia **2017**.